



University of  
Massachusetts  
Amherst

## Aspects of Network Formation and Property Evolution in Glassy Polymer Networks

Item Type	dissertation
Authors	Detwiler, Andrew Thomas
DOI	<a href="https://doi.org/10.7275/2387668">10.7275/2387668</a>
Download date	2024-12-01 23:00:41
Link to Item	<a href="https://hdl.handle.net/20.500.14394/38888">https://hdl.handle.net/20.500.14394/38888</a>

ASPECTS OF NETWORK FORMATION AND PROPERTY EVOLUTION IN  
GLASSY POLYMER NETWORKS

A Dissertation Presented

by

ANDREW THOMAS DETWILER

Submitted to the Graduate School of the  
University of Massachusetts Amherst in partial fulfillment  
of the requirements for the degree of

DOCTOR OF PHILOSOPHY

September 2011

Polymer Science and Engineering

© Copyright by Andrew Thomas Detwiler 2011  
All Rights Reserved

ASPECTS OF NETWORK FORMATION AND PROPERTY EVOLUTION IN  
GLASSY POLYMER NETWORKS

A Dissertation Presented

By

ANDREW THOMAS DETWILER

Approved as to style and content by:

---

Alan J. Lesser, Chair

---

Thomas J. McCarthy, Member

---

Surita R. Bhatia, Member

---

David A. Hoagland, Department Head  
Polymer Science and Engineering

## DEDICATION

To the teachers who dedicate themselves to fostering a love of science and learning.

## ACKNOWLEDGEMENTS

The time I have spent in graduate school at UMass has been filled with learning in all areas of my life. I have had the good fortune to meet many new friends and colleagues during my time here. I would first like to thank my advisor, Professor Alan Lesser, for his patience in allowing me to develop as a researcher and as a student. Without his insight and guidance this work would not have been possible. I would also like to thank my committee members, Professor Tom McCarthy and Professor Maria Santore, for their willingness to provide constructive feedback on my work and presentations.

I would like to thank the Center for University of Massachusetts Industrial Research on Polymers and the National Science Foundation Materials Research Science and Engineering Center for funding and instrument access. I am also grateful for the work of James Gorman as part of the Research Experience for Teachers program.

I have enjoyed working with all the members of the campus community who have passed through the 3<sup>rd</sup> Floor labs. The sense of community in the department has made my time here enjoyable. I would also like to recognize the efforts of Dr. Greg Dabkowski, who first introduced me to the PSE Outreach Program. He has been a wonderful friend and mentor to me through my involvement in Outreach. His passion for teaching and learning has been inspirational.

I thank my family and friends for their support during my many years of schooling. I must also thank my wife, Liv, whose love and support have been critical to surviving the dissertation process.

ABSTRACT

ASPECTS OF NETWORK FORMATION AND PROPERTY EVOLUTION IN  
GLASSY POLYMER NETWORKS

SEPTEMBER 2011

ANDREW THOMAS DETWILER, B.A., CASE WESTERN RESERVE UNIVERSITY

B.S.E, CASE WESTERN RESERVE UNIVERSITY

M.S., UNIVERSITY OF MASSACHUSETTS AMHERST

Ph.D., UNIVERSITY OF MASSACHUSETTS AMHERST

Directed by: Professor Alan J. Lesser

Experimental and theoretical characterization techniques are developed to illuminate relationships between molecular architecture, processing strategies, and physical properties of several model epoxy-amine systems. Just beyond the gel point partially cured networks are internally antiplasticized by unreacted epoxy and amine which leads to enhanced local chain packing and strain localization during deformation processes. Additional curing causes the antiplasticization to be removed, resulting in lower modulus, density, yield stress, and less strain localization. Physical and mechanical probes of network formation are discussed with respect to several different partially cured model epoxy-amine chemistries.

The non-linear fracture energy release rate and the molecular architecture of virgin and healed epoxy networks are related through an effective crack length model. The inelastic component of the fracture energy release rate is attributed to the failure of

network strands in a cohesive zone at the crack tip. Data from fracture and healing experiments are in good agreement with the model over more than three orders of magnitude. Changes in the shape of the process zone and deviation from planar crack growth cause deviations from the model for the toughest networks tested.

Double network epoxies are created from stoichiometric blends of an epoxy resin cured sequentially with aliphatic and aromatic amine curing agents. Unreacted epoxide and aromatic amine functionality antiplasticize the partially cured materials. The thermal and mechanical properties of the fully cured networks vary according to composition. No evidence of phase separation is observed across the entire composition and conversion range. However, the breadth of the glass transition in the double networks increases due to the difference in the molecular stiffness of the two curing agents.

Techniques are developed to monitor the evolution of residual stresses and strength in complex multicomponent epoxy-amine based coatings. The evolution of properties is attributed to loss of volatile small molecules from the coatings. The stresses that develop in biaxially constrained membranes are monitored through mechanical excitation. The strength of the membranes is determined by monitoring the size and shape of center cracks. This fracture analysis technique allows the evolution of stresses and toughness of the materials to be monitored simultaneously.

# TABLE OF CONTENTS

	Page
ACKNOWLEDGEMENTS .....	v
ABSTRACT .....	vi
LIST OF TABLES .....	x
LIST OF FIGURES .....	xi
 CHAPTER	
1. ASPECTS OF NETWORK FORMATION IN GLASSY THERMOSETS .....	1
Abstract .....	1
Introduction .....	1
Method .....	4
Results and Discussion .....	6
Tg-Conversion .....	6
Density .....	8
True Stress-Strain Response .....	12
Modulus .....	15
Yield .....	16
Post-Yield Response .....	17
Strain-Hardening .....	20
Strain Localization .....	24
Shear Band Stability .....	26
Conclusions .....	32
References .....	34
2. MOLECULAR ASPECTS OF FRACTURE AND SELF-HEALING IN GLASSY THERMOSETS .....	40
Abstract .....	40
Introduction .....	40
Method .....	42
Sample Preparation .....	43
Thermal Analysis .....	44
Compression Testing .....	44
Fracture Toughness Testing .....	44
Healing .....	45
Results and Discussion .....	46
Molecular Considerations of Fracture .....	49

Designing a Healing System.....	59
Conclusions.....	60
References.....	61
3. CHARACTERIZATION OF DOUBLE NETWORK EPOXIES WITH TUNABLE COMPOSITIONS.....	65
Abstract.....	65
Introduction.....	66
Method.....	68
Results and Discussion.....	70
Partially Cured Networks.....	70
Fully Cured Networks.....	73
X-Ray Scattering.....	78
Compression Testing.....	80
Conclusions.....	90
References.....	91
4. THE EVOLUTION OF STRESS AND STRENGTH DEVELOPMENT IN EPOXY BASED COATINGS.....	96
Abstract.....	96
Introduction.....	97
method.....	99
Results and Discussion.....	103
Acoustic Stress Measurement.....	109
Stress Measurement: Inflation.....	115
Membrane Strength Measurements.....	119
Method of Virtual Work.....	121
Monitoring Stress and Strength.....	127
Conclusions.....	128
References.....	129
BIBLIOGRAPHY.....	130

## LIST OF TABLES

Table	Page
Table 2-1. Physical and mechanical properties of epoxy-amine resins. ....	48
Table 2-2. Fracture model parameters for virgin and healed networks. ....	57
Table 4-1. Values of $\gamma_{mn}$ determining the frequencies of free vibration of a circular membrane.....	110
Table 4-2. Prefactors and coefficients of the polynomials $P_T^{+n}(m)$ .....	126

## LIST OF FIGURES

Figure	Page
Figure 1 -1. a) $T_g$ as a function of conversion. Dashed lines indicate critical conversion and critical $T_g$ . b) Density as a function of $T_g$ .	8
Figure 1.-2. Density evolution during cure for two isothermal cure temperatures.	9
Figure 1-3. Typical true stress versus neo-Hookian strain compression curve.	13
Figure 1-4. True stress vs neo-Hookian strain for isothermally cured resins and resins cured using the temperature ramp.	14
Figure 1-5. Physical and mechanical properties as functions of $T_g$ .	15
Figure 1-6. a) Strain hardening modulus as a function of $T_g$ . b) $M_c$ as a function of $T_g$ .	22
Figure 1-7. Necking stability contour map.	25
Figure 1-8. a) Shear band support fixture and sample. b) Shear sample before (left) and after (right) testing.	30
Figure 1-9. Shear band stability map.	32
Figure 2-1. Epoxy and amine monomers	43
Figure 2-2. Plot of mode I fracture toughness vs glass transition temperature.	46
Figure 2-3. Plots of the non-linear fracture energy (J) vs the linear component ( $J/(1+X)$ ).	55
Figure 3-1. Epoxy resin and amine cross-linkers.	68
Figure 3-2. Plot of storage modulus vs. temperature from DMTA temperature scans of partially cured networks.	72
Figure 3-3. Plot of loss modulus vs. temperature from DMTA temperature scans on partially cured networks.	72
Figure 3-4. Plot of true stress vs Neo-Hookian strain from uniaxial compression testing of partially cured networks.	73
Figure 3-5. Plot of $T_g$ of double networks as a function of DDS fraction.	74
Figure 3-6. Plot of storage modulus vs Temperature scans from DMTA analysis.	75
Figure 3-7. Plot of loss modulus vs Temperature scans from DMTA analysis.	75

Figure 3-8. Normalized loss modulus vs shifted $T_g$ plotted from DMTA temperature scans of selected network compositions..	76
Figure 3-9. Plot of full width at half-maximum vs. DDS fraction from the $\alpha$ -transition region of DMTA temperature scans .....	77
Figure 3-10. Plot of wide angle x-ray scattering profile vs. scattering vector from fully cured networks..	79
Figure 3-11. Plot of small angle x-ray scattering profile vs. scattering vector from fully cured networks..	79
Figure 3-12. Plot of true stress vs Neo-Hookian strain from uniaxial compression tests on fully cured networks conducted at 20°C..	83
Figure 3-13. Plot of compressive modulus vs DDS fraction measured at 20°C.....	83
Figure 3-14. Plot of yield stress vs DDS fraction..	84
Figure 3-15. Plot of density vs DDS fraction measured by the water displacement method at 21°C..	85
Figure 3-16. Plot of strain hardening modulus vs DDS fraction..	85
Figure 3-17. Plot of cross-link density calculated from the strain hardening modulus vs cross-link density calculated from the stoichiometric balance of monomers..	86
Figure 3-18. Plot of true stress vs. Neo-Hookian strain from compression tests conducted at $T_g+20^\circ\text{C}$ for double networks..	87
Figure 3-19. Plot of compressive modulus vs DDS fraction measured in the low strain region of compression tests conducted at $T_g+20^\circ\text{C}$ .....	88
Figure 3-20. Plot of molecular weight between cross-links vs DDS fraction. ....	88
Figure 3-21. Plot of true strain at break vs DDS fraction from compression testing..	90
Figure 4- 1 DSC temperature scans of membrane materials..	104
Figure 4- 2 Residual weight vs temperature from a TGA temperature scan on membrane material immediately after removal from glass molds..	104
Figure 4- 3. Log-log plot of weight loss vs time during isothermal conditioning of membrane material freshly removed from glass mold. ....	105
Figure 4- 4 DMTA temperature sweeps of coating material conditioned at 55°C..	107
Figure 4- 5. Elastic modulus versus weight loss measured in tension at 55°C.....	108

Figure 4-6. Acoustic testing assembly.....	110
Figure 4-7. Sonograms representing the amplitude in units of sound pressure level of the measured responses of membranes to acoustic frequency sweeps..	112
Figure 4-8. Contour plot of (0,2) normal mode..	113
Figure 4-9. Resonant frequency of the (0,2) mode as a function of weight loss for a membrane conditioned at 55°C.....	114
Figure 4-10. Stress vs weight loss.....	115
Figure 4-11. Photograph (left) of the inflation setup with LVDT, flange, membrane, and air supply. Schematic (right) with components labeled and sealed in an oven during a measurement. ....	116
Figure 4-12 Membrane Inflation Diagram.....	117
Figure 4-13. Plot of membrane stress vs inflation pressure measured at 55°C during inflation (blue diamonds) and deflation (red squares) at 6.3% weight loss, corresponding to the initiation of macroscopic crack extension at 55°C.....	118
Figure 4-14. Polynomial fit of the graphical solution for $K_I$ for equibiaxial stress on a center cracked membrane. Inset is a schematic of the geometry of the cracked membrane.....	120
Figure 4-15. Polynomial fit to the solution curve for the stress intensity due to a point load on a circular membrane..	121
Figure 4-16 Plot of far-field stress vs weight loss for a center cracked biaxially constrained membrane. ....	127
Figure 4-17 Fracture toughness vs weight loss during conditioning of biaxially constrained membranes at 55°C.....	128

# CHAPTER 1

## ASPECTS OF NETWORK FORMATION IN GLASSY THERMOSETS

### **Abstract**

Aspects of network formation and the physical properties of stoichiometric amine-cured epoxy resins are investigated. The state of network formation is systematically controlled by using isothermal cure conditions and a linear temperature ramp condition. Affine deformation in compression at a constant true strain rate is used to measure the true stress-strain response from small strains to large strains. Beginning with the low-strain responses and continuing through yielding, partially cured samples demonstrate characteristics of physical ageing that diminish as the networks approach full conversion. The post-yield properties are characterized by a strong dependence on network connectivity with little influence of the curing method. The mechanical responses are also applied to necking and shear banding analyses. The resins are unable to achieve stable necking in tension. However, shear bands are able to be stabilized, as predicted by a model developed in this work. These results suggest that physical ageing is inherent in epoxy network formation, and the resulting strain localization significantly degrades the mechanical integrity of epoxy resins in the partially cured state, regardless of the cure conditions.

### **Introduction**

Physical ageing has been widely studied in thermoplastic systems where it has been associated with increases in density, modulus, and yield stress and with changes in

other rate- and temperature-dependent properties (1,2,3). The underlying physical consequences of the sub-molecular relaxations associated with physical ageing are increases in relaxation times and decreases in free volume. From an engineering perspective it is important to know the thermal and mechanical history of a material in order to be able to predict physical and mechanical properties over its lifetime. McKenna has shown with polycarbonate that mechanical and thermal rejuvenation do not produce identical states, and the yield stress evolves to different equilibrium values depending on the type of rejuvenation (4). However, Govaert *et al* showed mechanical rejuvenation and thermal treatments of polycarbonate only differed with respect to the “age” of the resulting material (5).

Thermoplastics have received much of the attention from researchers in the physical ageing literature due to their widespread application and somewhat more straightforward characterization relative to that of thermosets. Far less work has been reported on the effects of physical ageing in thermosets. Particularly in densely cross-linked systems where the relaxation of highly constrained chain segments into denser, less flexible conformations may be significantly hindered by the topological connections of the networks. Some authors who have studied physical ageing in glassy thermosets have seen responses similar to those observed in thermoplastics (6,7,8,9). A fundamental difference between most thermoplastics and thermosets is the processing conditions involved in their manufacture. Commercial thermoplastics are generally polymerized and pelletized before being shipped to a processing plant where they undergo some sort of molding operation. In contrast, thermosets such as epoxies, polyurethanes, and phenolics become intractable when they are polymerized. As a result, the monomers or precursors

must be molded into their final form before they are fully cured. This intractability also means the topological arrangement of chain segments and cross-links is fixed during the reactive step of processing.

Initial studies by this research group on thermosets indicate that characteristics commonly observed in the physical ageing of thermoplastics also occur in the early stages of epoxy network formation (10). To further our understanding, and to compare partially cured model epoxy networks with the literature on network formation and physical ageing, a sensitive probe of network formation is needed. Differential scanning calorimetry (DSC) is one technique that allows the characterization of the thermal properties of epoxy networks, namely  $T_g$  and conversion. As a complimentary technique a number of authors have studied the small-strain and yield responses of various epoxy networks as a function of temperature and/or composition (8,11,12,13,14,15). Relatively little work has considered the large-strain responses of glassy thermosets (16,17), particularly in the strain-hardening regime.

Lesser and Calzia used simple compression to test the strain-hardening properties of a series of fully cured networks with systematically varied molecular weight between cross-links ( $M_c$ ) (18). In their work  $M_c$  was controlled by stoichiometrically varying the ratio of a difunctional amine chain extender to a tetrafunctional amine cross-linker. They found the strain-hardening moduli of model aliphatic (more flexible backbone) and aromatic (stiffer backbone) epoxy resins to be highly correlated with  $M_c$ . By studying flexible aliphatic as well as stiffer aromatic cross-linkers and chain extenders they were able to show that the strain hardening response is independent of backbone stiffness. However, they also found that  $G_R$  decreases with increasing temperature in the glassy

state. This temperature dependence suggests strain hardening is not a purely entropic process in the glassy state.

In this study we use compression and other physical characterization techniques to analyze glassy network formation during the curing process. Physical and mechanical data are compared using several physical models. In addition, a model is developed to predict strain localization behavior as it applies to necking and shear banding. The purpose of the current work is not to investigate physical ageing or methods of rejuvenation, however comments are made with regard to the effect of thermal treatments and mechanical deformation on the materials investigated herein.

## **Method**

Stoichiometric mixtures of difunctional epoxide resin based on a purified diglycidyl ether of bisphenol A (DGEBA; DER 332, epoxide equivalent weight 175 g/mol); difunctional N,N'-dimethylethylenediamine (DMEDA Aldrich 90+%); and tetrafunctional ethylenediamine (EDA Aldrich 99+%) were poured into cylindrical glass molds treated with a release agent. The molds were placed in a 23°C water bath for several hours to control the exothermic reaction.

For an isothermal cure condition the molds were transferred from the water bath to nitrogen gas purged ovens at the desired cure temperatures (between 23°C and 165°C). Samples were cured isothermally for 18 hours in order to maximize the level of conversion possible at that temperature.

For a ramped cure condition, molds were transferred from the water bath to an oil bath at 25°C. The oil bath was then heated at a rate of 40°C per hour to 165°C. At intermediate temperatures molds were removed and quenched to room temperature in

water baths to give partially cured samples. Samples were stored in a freezer at  $-10^{\circ}\text{C}$  to prevent further curing and to inhibit physical ageing until they could be tested. Some partially cured samples from both the isothermal and ramp series were also post-cured at  $165^{\circ}\text{C}$  for four hours in order to observe the effect of cure path on their properties in the fully cured state.

The  $T_g$  of each resin was determined as the inflection point of the heat flow vs. temperature curve from DSC heating at  $10^{\circ}\text{C}$  per minute in a TA Instruments DSC 2910. Conversion was measured as the integration of the exotherm in the  $dH/dT$  curve of each resin.

Compression bullets were formed by cutting the cylinders into sections with height to diameter ratios of 1:1. Care was taken to machine the top and bottom faces of the cylinders such that there were parallel to each other and perpendicular to the sides of the cylinders. The faces were polished to give smooth, glassy surfaces. Density was measured at  $23^{\circ}\text{C}$  by the water displacement method (ASTM D792). Dimensions for compression testing were measured to the nearest 0.01 mm using calipers.

Immediately before compression testing a surfactant-PTFE film-surfactant treatment was applied to the top and bottom surfaces of the compression specimens in order to produce a low friction surface which would allow for affine deformation over a large range of strains. The samples were loaded in compression using an Instron 5800 fitted with a 50kN load cell and controlled using the Merlin software package. Samples were tested at  $20^{\circ}\text{C}$  and a constant true strain rate of  $0.1\text{mm/mm/min}$  ( $1.67 \times 10^{-3} \text{ s}^{-1}$ ) was maintained during the entire test.

Tensile testing was conducted on ASTM D638 Type I samples machined from 3mm thick plaques. Samples were tested at 20°C using a strain rate of  $1.67 \times 10^{-3} \text{ s}^{-1}$  on the same instrument described for compression testing (see above).

Characterization of shear bands was achieved by compressing rectangular specimens containing precracks intended to promote shear. Rectangular samples with dimensions of 40 x 13 x 6 mm were tested in compression in a modified IITRI fixture (see Image 1), which prevents buckling while allowing shear bands to be photographed *in situ* through the hole. The samples are placed upright between the two aluminum plates and the screws are hand tightened. Before testing fresh razor blades are tapped into 6 mm slots cut into the samples at 45° to promote shear band formation. A series of lines oriented perpendicular to the precracks are scratched into the sample surface in order to measure shear optically.

## **Results and Discussion**

### **Tg-Conversion**

The  $T_g$  of an epoxy resin increases as the conversion increases and the two have been shown to be well correlated (11,14,19,20). Differential scanning calorimetry (DSC) is widely used to measure  $T_g$  and conversion.  $T_g$  is often measured as the inflection point of the step change in the heat release rate versus temperature curve. Conversion ( $x$ ) is calculated by integrating under the heat of reaction peak ( $\Delta H$ ) above  $T_g$  in a plot of heat release rate (normalized by sample mass) versus temperature, then dividing by the heat of reaction of an uncured sample ( $\Delta H_0$ ) according to Equation 1-1 (21).

$$x = 1 - \frac{\Delta H}{\Delta H_0} \quad [1-1]$$

DGEBA is a difunctional epoxide and EDA is a tetrafunctional amine. When fully cured these monomers form a model network consisting of tetrafunctional cross-links (6,22). However, at intermediate stages of cure the networks are less well-defined since there is a distribution of EDA molecules that have reacted with zero, one, two, three, or four epoxide groups (13,19,20,22). For our case Flory's equation (Equation 1-2) predicts the gel point to be at a critical conversion ( $x_c$ ) of about 0.58 (24,25).

$$x_c = \frac{1}{[1 + (f - 2)]^{1/2}} \quad [1-2]$$

where  $f$  is the average functionality or average number of labile amine hydrogens on each cross-linker molecule. This prediction assumes equal reactivity of all species with no side reactions, such as etherification of the epoxide groups with hydroxyl groups. Several groups have demonstrated epoxies with gel points in the vicinity of this prediction, although the values are always slightly higher than 0.58 due to intramolecular reactions (25,26). At the critical conversion the resins treated here transition from sol glasses to gel glasses. Accordingly, many of the physical and mechanical properties reported in this work demonstrate qualitative changes in behavior when conversion approaches the critical conversion.

Figure 1-1a shows  $T_g$  as a function of conversion for resins cured by the isothermal and ramped cure schedules. The non-linear relationship between  $T_g$  and conversion has been reported by many authors using DSC (21) as well as FTIR absorbances to calculate conversion (20,27). The data points from the two curing methods overlap, which suggests the  $T_g$ -conversion relationship is not sensitive to the curing method. This cure path insensitivity was also suggested by Gillham and Wang for a series of aromatic amine-cured epoxy resins (19). It is notable that  $T_g$  increases sharply

as the conversion approaches 1. Since measures of conversion (from DSC or FTIR) are less sensitive than  $T_g$  to changes in the network in the high conversion regime,  $T_g$  is used throughout this paper as the quantitative measure of cure state.

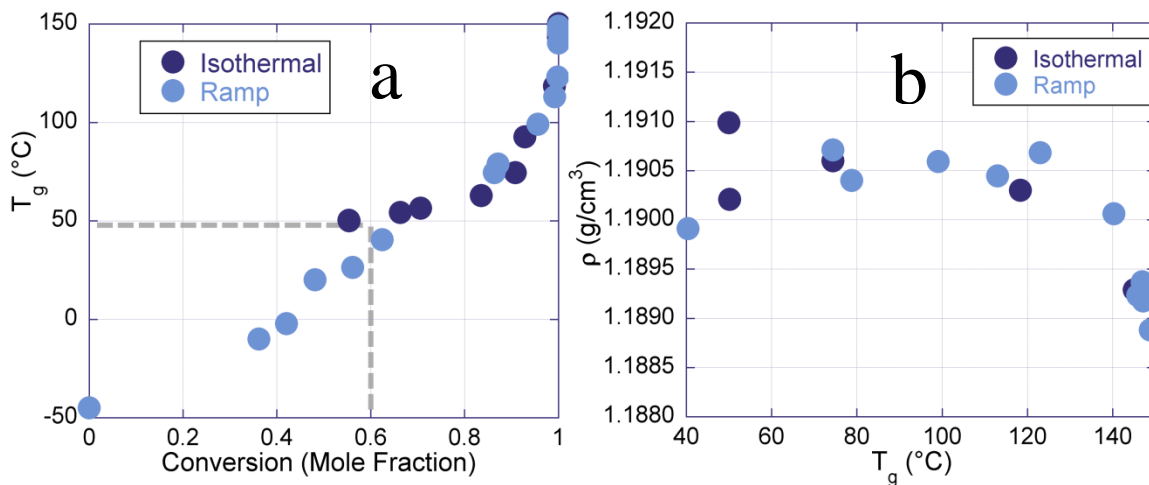


**Figure 1- 1. a)  $T_g$  as a function of conversion. Dashed lines indicate critical conversion and critical  $T_g$ . b) Density as a function of  $T_g$ .**

## Density

The monomers used to prepare these model epoxy networks begin as liquids at room temperature. The DGEBA has a density of 1.16 g/cm<sup>3</sup> while the EDA has a density of 0.899 g/cm<sup>3</sup>. Density at 23°C is plotted as a function of  $T_g$  for the two series of partially cured resins (Figure 1-1b). Beyond the gel point the resins have density values around 1.1905 g/cm<sup>3</sup>. When they achieve maximum  $T_g$  their density decreases slightly to approximately 1.1890 g/cm<sup>3</sup>, a decrease of 0.1%. Density evolves in a non-linear manner in this system. However, the changes in density are fairly small in this conversion range, especially when the precision of the measurements averages about  $\pm 0.0005$  g/cm<sup>3</sup>. The non-linear evolution of density as a function of  $T_g$  and the effects of thermal history have been reported for other epoxy systems (13,28,29,30). Density typically remains approximately constant from the gel point until resins approach the maximum  $T_g$  where

density suddenly decreases. This decrease in density has been attributed to the lower coefficient of thermal expansion of polymers in the glassy region relative to that in the rubbery region. It is unlikely to be a result of further conversion since, although there is a significant change in  $T_g$  over this range (120-145°C), conversion is essentially complete (Figure 1-1a). This de-densification at maximum  $T_g$  is observed for all fully cured resins, including those initially cured at 165°C and those subjected to a post-cure.

Below is a simplified diagram that qualitatively illustrates how the density of a typical epoxy resin changes during two different isothermal cure conditions (31) (Figure 1-2).

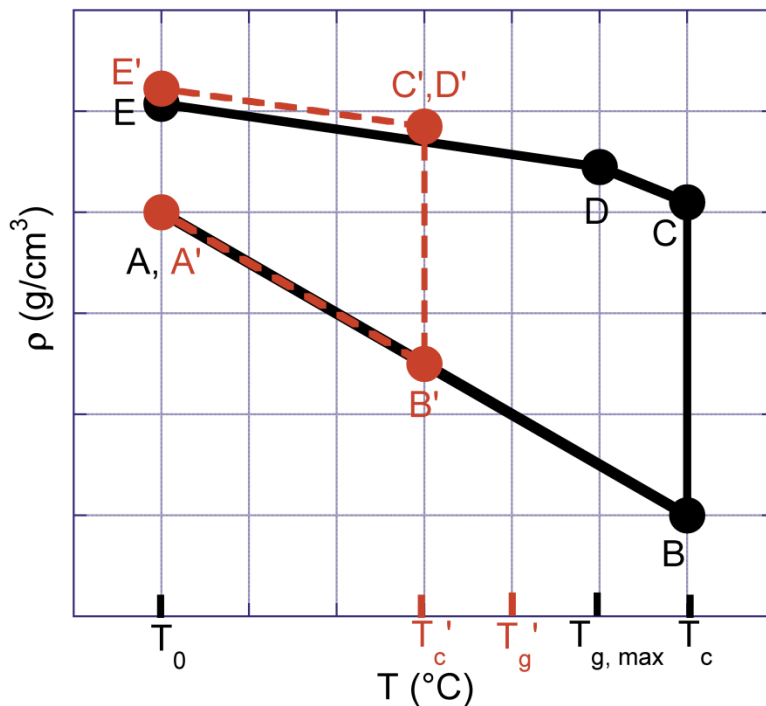


**Figure 1-2. Density evolution during cure for two isothermal cure temperatures. For ABCDE  $T_c > T_{g, max}$ . For A'B'C'D'E'  $T'_c < T'_g$ . The prime symbols (') are used to distinguish between the two paths.**

Path ABCDE depicts an isothermal cure where the cure temperature ( $T_c$ ) is above the maximum  $T_g$  ( $T_{g, max}$ ) of the fully cured resin, whereas  $T'_c$  for path A'B'C'D'E' is below  $T_{g, max}$ . In ABCDE the epoxide and amine monomers are heated from A to B, i.e. room

temperature ( $T_0$ ) to  $T_c$ . The density decreases during this process due to thermal expansion in the liquid state. From B to C the system is held isothermally at  $T_c$  for some amount of time to allow the chemical reaction to proceed. There is isothermal shrinkage due to the curing reaction. The  $T_g$  of the system increases during this step due to the increase in molecular weight and the cross-linking reactions. When the system arrives at C it is assumed that the resin is fully cured and no further chemical reactions take place. The resin is cooled in the rubbery state under quasi-equilibrium conditions from C until it approaches its  $T_g$  at D. The cooling continues from D to E in the glassy state under non-equilibrium conditions.

The other cure path, A'B'C'D'E', uses a lower  $T_c'$  which produces a resin with lower  $T_g'$  and slightly higher density. Vitrification occurs during cure since  $T_g'$  increases above  $T_c'$ . Therefore, points C' and D' overlap, and all cooling occurs in the glassy state. This cure path is typical of what partially cured epoxy resins experience since  $T_g$  tends to be between 10°C and 30°C greater than  $T_c$ , assuming the resin is reactive at  $T_c$  (14,20,29,32).

There are several explanations put forward in the literature to explain the observed behavior in terms of chemical and physical changes, respectively, that occur during epoxy processing. The following two paragraphs treat the portions of Figure 1-2 that include the segments from B to C (chemical) and C to E (physical), respectively.

The volume occupied by a chain segment can be broken down into vibrational volume, van der Waals volume, and free volume (33). Vibrational volume is assumed to be constant for an epoxy in the glassy state, independent of conversion (33,34). Based on an analysis of the van der Waals contributions to volume over the course of curing a

similar DGEBA-based epoxy system, others have shown that the van der Waals radius actually increases as epoxies cure (34). This expansion was mainly attributed to the opening of the highly strained epoxide ring. However, positron annihilation studies have shown that free volume passes through a minimum in the vicinity of the gel point, followed by a small increase as cure proceeds beyond the gel point in epoxy systems (34). The reduction in free volume dominates over the van der Waals expansion effect until the gel point is reached, at which point free volume remains relatively constant while van der Waals based expansion continues until the resin is fully cured. In agreement with the literature, we observe a maximum in the room temperature density in the vicinity of the gel point and a decrease in density with further conversion.

If density is measured at room temperature it is necessary to cool the sample from an elevated cure temperature ( $T_c$ ) to the measurement temperature. This consists in cooling in the rubbery state if  $T > T_g$  and/or cooling in the glassy state when  $T < T_g$ . Molecular rearrangements in the rubbery state occur rapidly, thus equilibrium is reached in a matter of seconds (33). However, molecular rearrangements in the glassy state are orders of magnitude slower than in the rubbery state. Therefore a material in the glassy state is unable to completely equilibrate when it is subjected to a finite cooling rate. This departure from equilibrium is evidenced by excess enthalpy ( $\Delta H^\circ$ ), entropy ( $\Delta S^\circ$ ), free energy ( $\Delta G^\circ$ ), and volume ( $\Delta V^\circ$ ). These excess quantities spontaneously decrease toward their equilibrium values, hence physical ageing (2,35,36). However, the time scale of this equilibration is often longer than the experimental time scale, particularly when the difference between the measurement temperature and the  $T_g$  is large. Thus, the result of

these “frozen in” excess quantities is a lower measured density at finite times and a slow increase in density over time as the material physically ages.

These explanations are consistent with the behavior we see in our resins. The maximum in density is found in resins which are near the gel point where the network has not yet severely restricted the packing of the chains, and a minimum amount of cooling has occurred in the glassy state. Fully cured resins have lower density than any resin beyond the gel point due to the severe restrictions on chain packing imposed by the tightly cross-linked networks, and because the maximum amount of cooling has occurred in the glassy state.

### **True Stress-Strain Response**

Compression testing is widely used to characterize the true material response of polymers subjected to large deformations. Others have shown that the initial stages of deformation are associated with the process history of the glass and large deformations are associated with the cross-linked network. The combination of deformation mechanisms activated in each region of the true stress versus true strain curves allows one to extract information about the state of physical ageing and network formation exhibited by the resins.

Figure 1-3 is a typical epoxy stress-strain curve that highlights some of the attributes of the experimental data discussed below. The true stress ( $\sigma_t$ ) is plotted on the y-axis. The x-axis is divided into the low strain regime, where we are interested in the true strain ( $\epsilon_t$ ) response, and the large strain regime where the neo-Hookean strain  $-(\lambda^2 - 1/\lambda)$  is a better measure of the network response.  $\lambda$  is the compression ratio, measured as the current length ( $l$ ) divided by the original length ( $l_0$ ).

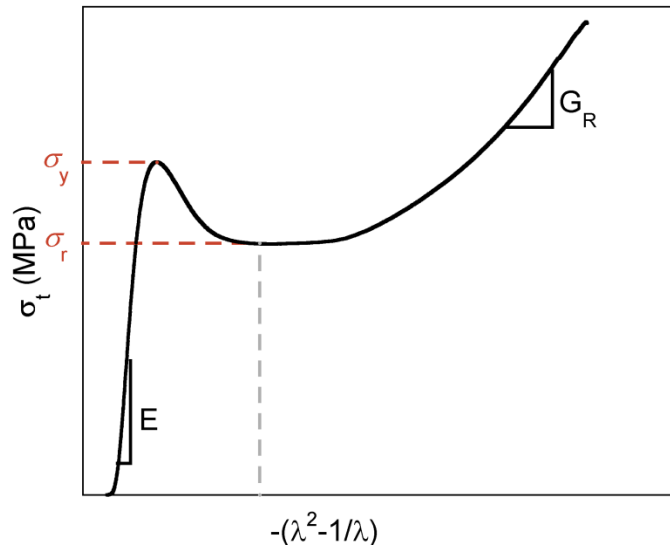


**Figure 1-3. Typical true stress versus neo-Hookian strain compression curve. Dark dashed lines represent yield stress and rejuvenated stress. Light dashed line divides low and high strain regions.**

The compressive modulus ( $E$ ) is measured as the slope of the  $\sigma_t$ - $\varepsilon_t$  curve in the initial linear elastic regime. The yield stress ( $\sigma_y$ ) is taken as the local maximum in the  $\sigma_t$ - $\varepsilon_t$  curve where large-scale plastic deformation begins. The rejuvenated stress ( $\sigma_r$ ) is the local minimum in the  $\sigma_t$ - $\varepsilon_t$  curve after yield. The post-yield stress drop is due to a combination of network packing and network connectivity effects. It can be parameterized as  $K_y = \sigma_y / \sigma_r$  for the calculation of necking and shear banding stability. Beyond the local stress minimum after yield, the stress increases again with further deformation. At this point it is more convenient to use a neo-Hookian strain term, instead of true strain, because the slope of the  $\sigma_t$  vs  $-(\lambda^2 - 1/\lambda)$  curve is the strain hardening modulus ( $G_R$ ), which is used to calculate network connectivity in terms of the molecular weight between cross-links ( $M_c$ ). Each of these regions will be discussed in subsequent sections.

The true stress-neo-Hookian strain curves of resins cured using isothermal and ramp cure conditions are displayed in Figure 1-4a and Figure 1-4b, respectively. For small

strains  $-(\lambda^2-1/\lambda) \approx \epsilon_t-1$ , which amounts to shifting the origin to zero in the small strain regime. The series of isothermal and ramp-cured resins clearly show qualitative differences between resins with different  $T_g$ 's within each series.

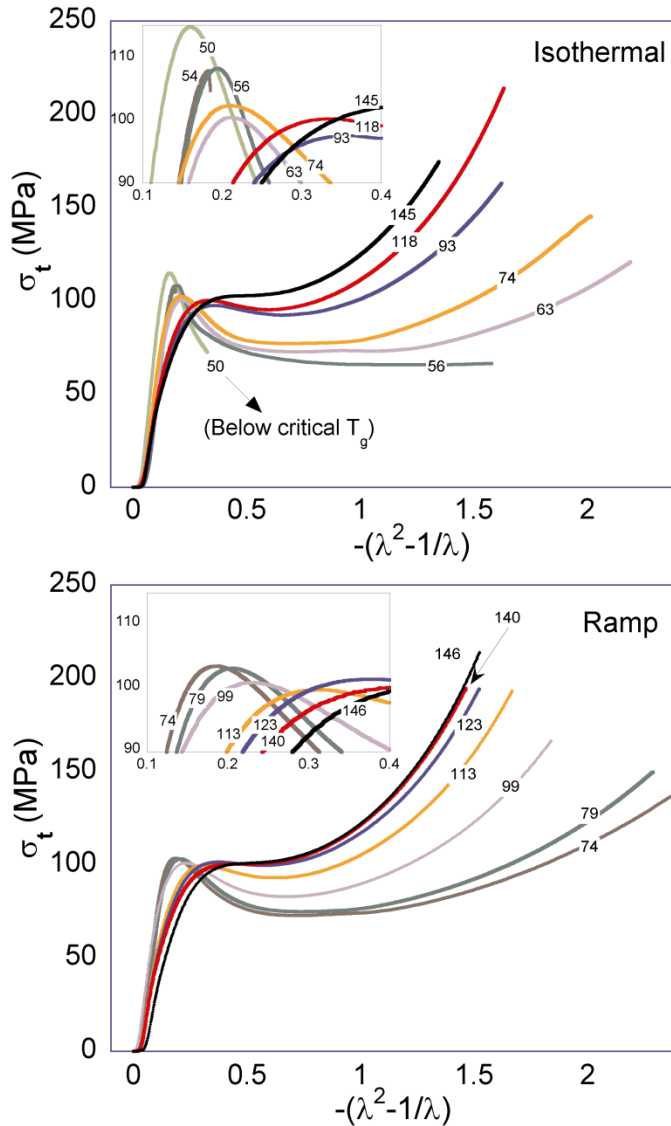


**Figure 1-4. True stress vs neo-Hookean strain for isothermally cured resins and resins cured using the temperature ramp. Curves are labeled with their  $T_g$ 's. Inset is an expansion of the yield region.**

For comparison, the curves are labeled with the  $T_g$  of the resins. At low  $T_g$  (e.g. low conversion) there is a pronounced stress maximum followed by a significant drop in stress. The magnitude of this stress maximum decreases and flattens out as  $T_g$  increases.

In addition, the initial slope of the deformation curves decreases as a function of  $T_g$ ,

whereas the slope at high strains increases as  $T_g$  increases. These progressions in the slopes of the curves are caused by changes in network packing and network connectivity, respectively. The characteristics of each region of the curves will be discussed in detail in the sections that follow.

## Modulus

The modulus of polymers in the glassy state is sensitive to molecular packing (37), and it typically correlates well with density.

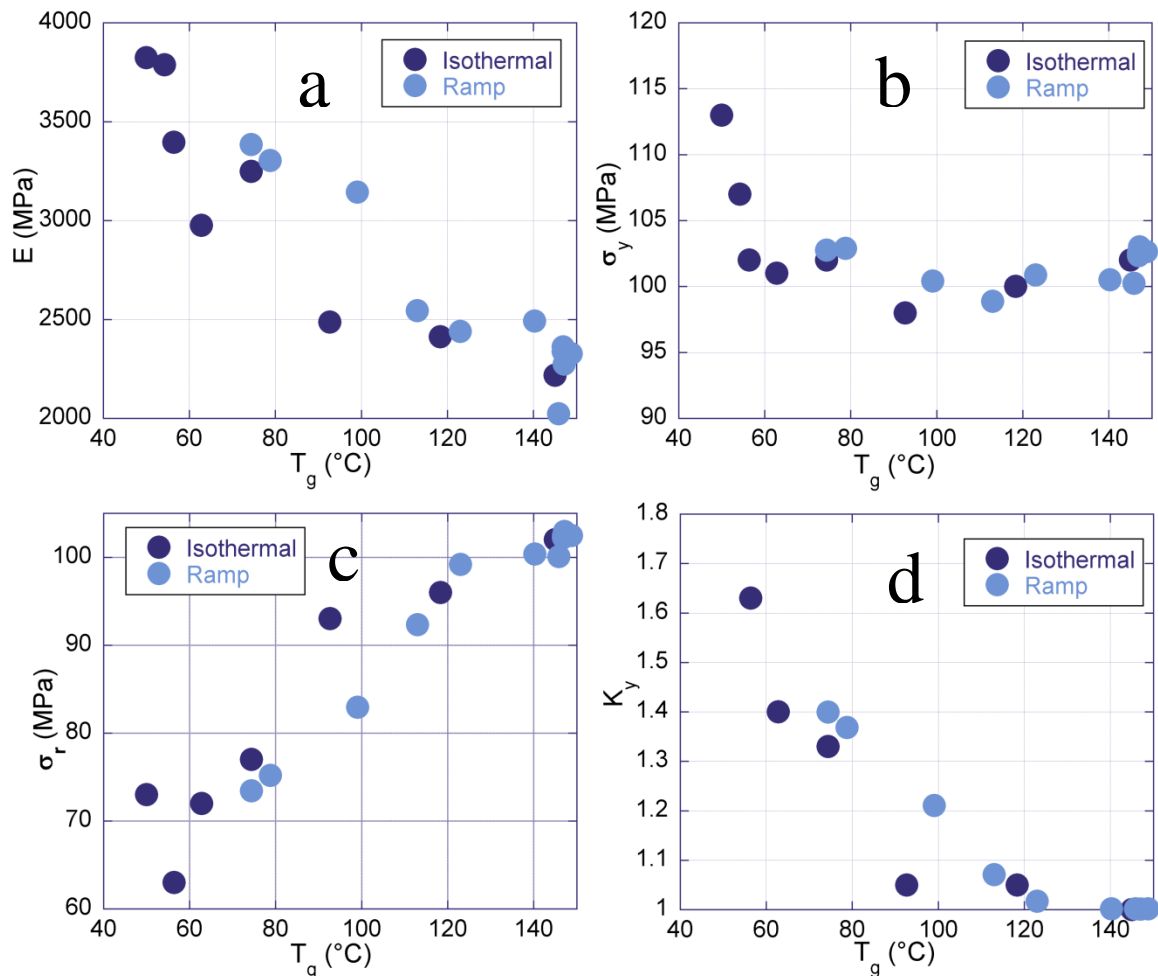


**Figure 1-5. Physical and mechanical properties as functions of  $T_g$ . a) modulus, b) compressive yield stress, c) rejuvenated stress and d) strain localization constant.**

Just as Figure 1-1b demonstrates a decrease in density with  $T_g$ , Figure 1-5a highlights the decrease in modulus with  $T_g$  for resins in both the isothermal and the ramp

cure series. The decrease in modulus as  $T_g$  increases has been previously reported in work on other resin systems (29,38,39). In this system, resins with  $T_g$  values well below  $145^\circ\text{C}$  have significant levels of unreacted amine and epoxide groups. These groups are thought to be able to pack more efficiently than network chains because they have more conformational freedom than the chains that are fully incorporated into the network (i.e. fully reacted segments) (39). A similar argument can be made in terms of physical ageing. Modulus increases as a result of physical ageing where decreased free volume and longer relaxation times increase the apparent stiffness of materials (2). From Figure 1-5a it is clear that modulus decreases as  $T_g$  increases. When subjected to cure conditions that achieve the maximum  $T_g$ , either initially or as a post-cure step, all samples have approximately the same modulus regardless of the initial cure conditions. Therefore, cure path does not appear to affect the modulus of fully cured resins. However, physical ageing appears to be highly correlated with  $T_g$  in the partially cured resins.

## **Yield**

Yielding is a thermally activated stress-induced material response (40). It is the manifestation of macroscopic plastic flow in polymer systems. When inter- and intramolecular forces are no longer sufficient to elastically store additional mechanical energy localized shear bands begin to grow through the volume of the material (9). In Figure 1-5b we observe higher yield stresses in resins with low  $T_g$ 's.

Many authors have shown that yield stress increases when a polymer is physically aged (1,2,3,9,41). However, yield stress levels off around 100 MPa for resins with  $T_g$  greater than  $60^\circ\text{C}$  in the isothermal and ramp cure series. It is important to note that resins in both series with  $T_g$ s below  $50^\circ\text{C}$  fail to achieve yield. Below this low  $T_g$  threshold,

axial cracks propagate through the samples before a macroscopic yield condition is satisfied. Other authors have also commented on the difficulty in machining and testing epoxy resins with low conversions because they are extremely brittle and weak (20). Axial cracking under uniaxial compression has been observed in brittle inorganic materials (42). This fracture is thought to result from an inhomogeneous stress distribution at the platen-sample interfaces and the concurrent inability of the materials to sustain even relatively low levels of localized shear. As mentioned in the introduction, the yield point is considered to be the point at which shear bands begin to propagate through the whole compression bullet. This argument suggests lubrication and absolutely parallel platens and sample ends could help to alleviate this issue. However, perfect lubrication and alignment cannot overcome the susceptibility of inherently flawed networks, such as highly undercured epoxies, to brittle fracture. Therefore, there appears to be a threshold of network formation, in the vicinity of the gel point, before which these epoxy resins cannot be evaluated in the large strain regime using this technique. Below, we consider how the interplay between yield and post-yield behavior can be used to predict the conditions necessary to stabilize shear deformation.

### **Post-Yield Response**

The local minimum in the stress after yield is referred to as the rejuvenated stress ( $\sigma_r$ ) for its relationship with the erasure of physical ageing. Haward and Cross and several subsequent authors found that subjecting polymers to mechanical deformation beyond yield can remove some of the effects of physical ageing e.g. rejuvenating the material (1,4,9,43,44). As a dramatic example, van Melick, Meijer, and Govaert were able to demonstrate affine deformation of polystyrene in tension by mechanical preconditioning

(45). Another common method for removing physical ageing is to anneal a material above  $T_g$ , then quench it to a temperature well below  $T_g$  where physical ageing is very slow. Although quite useful with fully cured resins, thermal rejuvenation is not practical with the current reactive partially cured resins since heating above  $T_g$  will advance the curing reaction. Other less reactive systems, such as DGEBA cured with diaminodiphenylsulfone (DDS), may have some processing window above  $T_g$  where partially cured resins can be thermally equilibrated for a short time without significantly advancing the cure (11). It has also been demonstrated that mechanical rejuvenation is not equivalent to thermal rejuvenation (4,46). As such, the thermo-mechanical history of a sample can strongly influence deformation behavior.

Thermomechanical history is relevant to the current study because partially cured resins with different thermal histories are compared. If mechanical rejuvenation takes place in these materials the post-yield response should only depend on the viscous flow properties of the networks rather than any thermomechanical history (9,43). Figure 1-5b demonstrates the complex relationship between yield stress and  $T_g$ , and supports the argument that yield is sensitive to molecular packing and physical ageing. In contrast, Figure 1-5c shows that the rejuvenated stress appears to be linearly proportional to  $T_g$ . The proportionality between rejuvenated stress and  $T_g$ , and the fact that both sets of data points fall on the same curve, suggests the rejuvenated stress is insensitive to any molecular packing or physical ageing that may take place during the curing process. Therefore, the long-range network connectivity is the dominant factor affecting the rejuvenated stress.

None of the resins treated here have been subjected to mechanical or thermal pre-treatments besides the thermal treatment used to cure them (see Methods). However, the stress-strain curves of the partially cured resins depicted in Figure 1-4a and Figure 1-4b clearly show rejuvenated stresses that are lower than the yield stress. Only the resins taken to full cure at 165°C have a negligible decrease in stress after yield, which indicates the absence of physical ageing. The difference between the yield stress and the rejuvenated stress is often referred to as strain softening, which is a manifestation of strain localization associated with physical ageing. Beyond the yield point localized deformation takes place in shear bands. The macroscopically measured stress continues to decrease as the shear bands expand to incorporate more material. When the shear bands have expanded to include all the material in a compression bullet, the local stress minimum or the rejuvenated stress is obtained. Further deformation is affine in nature, similar to deforming an elastomer above  $T_g$ . Others have argued that deforming a material to the yield point is the mechanical analog of lowering the  $T_g$  of a material to the test temperature (40). In any case, the true stress-true strain response, where the rejuvenated stress is measured and at higher strains, is highly dependent on network connectivity and relatively less dependent on molecular packing.

In order to be able to compare the cure dependence of different resin systems it would be convenient to parameterize the effect of physical ageing in the transition zone between processing dependent and network connectivity dependent properties. The yield stress offers information about how physical ageing and the local chain packing environment affects a material's resistance to flow, whereas the rejuvenated stress offers insight into how the network connectivity affects resistance to flow. Normalizing the

yield stress by the rejuvenated stress gives a dimensionless strain localization parameter ( $K_y = \sigma_y / \sigma_r$ ) that can be applied to various resin systems, including thermoplastics (3).  $K_y$  quantifies the excess stress required to initiate large-scale plastic deformation in a material (i.e. yield stress) relative to the stress required to continue deforming the material beyond yield (i.e. rejuvenated stress). Numerous authors have demonstrated the strain-rate and temperature dependence of yield stress and the rejuvenated stress, so  $K_y$  is necessarily dependent on those variables as well (3,6,18,33,47,48,49,50,51).

Figure 1-5d is a plot of  $K_y$  versus  $T_g$ , where we see an inverse proportionality between  $K_y$  and  $T_g$ .  $K_y$  approaches 1 as the resins approach the maximum  $T_g$ . Therefore, there is an insignificant amount of strain localization that occurs in the deformation of fully cured resins. This lack of strain localization implies that physical ageing is removed as network formation proceeds.

### **Strain-Hardening**

Much of what we know about the strain-hardening responses of polymer networks appears in the literature on thermoplastics and rubbers. Constitutive relationships have been developed to describe large-strain deformation where molecular entanglements form the basis of network structures (3,47,49,52). One theme that is derived from the rubber elasticity approach of these constitutive relationships is the idea that networks display an entropic hardening response at high strains. This non-linear behavior can be captured by using a non-linear measure of strain such as the neo-Hookian strain. Here, the strain hardening modulus ( $G_R$ ) is the slope of the true stress ( $\sigma_T$ ) versus neo-Hookian strain curve as given by Equation 1-3.

$$G_R = -\frac{\partial \sigma_T}{\partial (\lambda^2 - 1/\lambda)} \quad [1-3]$$

where  $\lambda$  is the extension ratio. The molecular weight between entanglements ( $M_e$ ) is calculated from Equation 1-4, which was originally developed to describe transient molecular entanglement networks in thermoplastics (49).

$$M_e = \frac{\phi \rho R T}{G_R} \quad [1-4]$$

Where  $\rho$  is the mass density,  $R$  is the ideal gas constant,  $T$  is the absolute temperature, and  $\phi$  is a constant related to cross-link mobility and is assumed to be equal to 1 for immobile cross-links (32,53). Equation 1-4 can be applied to thermosets with high cross-link densities by assuming cross-links and chain entanglements are analogous such that  $M_c = M_e$ , where  $M_c$  is the molecular weight between cross-links.

Equations 1-3 and 1-4 provide a way to interpret the strain-hardening responses of networks in terms of network architecture. Similar to the effect seen in the rejuvenated stress, differences in network connectivity are assumed to be the dominant factor affecting the mechanical response in the strain-hardening regime (3,37,47,48). The strain hardening modulus ( $G_R$ ) is the value from Equation 1-3 at 90% of the ultimate true strain. Using the slope at 90% of the ultimate true strain samples  $G_R$  at a standardized location along the true stress versus neo-Hookian strain curve for each resin. In the case of perfect adherence to the constitutive model, the true stress would increase linearly with respect to neo-Hookian strain in the strain hardening regime, whereas we see a slight increase in slope as strain increases in this regime. Several authors have commented that the true stress versus neo-Hookian strain curve increases faster than linearly due to finite extensibility considerations and the non-Gaussian deformation behavior of tightly cross-

linked networks in the glassy state (48,54). While more accurate stress-strain measures incorporating inverse Langevin and other strain functions have been proposed (44,49,51), the current method is sufficient to highlight the trends found herein.

Figure 1-6a demonstrates the proportionality between  $G_R$  and  $T_g$ . According to Equation 1-3,  $G_R$  is inversely proportional to  $M_c$ . Since the density and test temperature are essentially constant between samples in both series of resins in Figure 1-6a,  $G_R$  is the main factor affecting the calculated value of  $M_c$ .

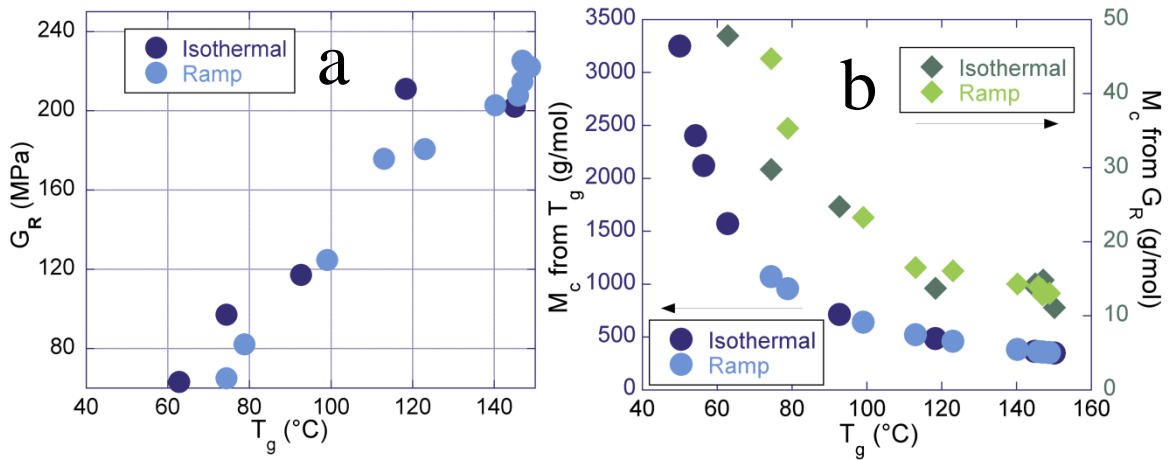


**Figure 1-6. a) Strain hardening modulus as a function of  $T_g$ . b)  $M_c$  as a function of  $T_g$ . Left y-axis applies to  $M_c$  values calculated from Equation 1-6 (i.e. from  $T_g$ ). Right y-axis applies to  $M_c$  calculated from Equation 1-4 (i.e. from  $G_R$ ).**

$M_c$  can also be calculated from the molecular weights of the epoxy and amine monomers (Equation 1-5).

$$M_c = 2 * (M_p + M_a) \quad [1-5]$$

where  $M_p$  is the epoxide equivalent weight ( $\sim 175$  g/mol for DGEBA),  $M_a$  is the amine equivalent weight (15 g/mol for EDA), and all cross-links are assumed to be tetrafunctional (55). For the ideal case of a stoichiometric EDA-DGEBA resin taken to full cure,  $M_c$  is equal to 380g/mol. The value of  $M_c$  calculated from  $G_R$  is an order of magnitude smaller than the value calculated from stoichiometry. Previous work by other authors has found a similar discrepancy between calculations based on stoichiometry and

sub- $T_g$  mechanical characterizations of  $M_c$  (18,55). The rubber elasticity-based theory used to calculate  $M_c$  is expected to deviate from ideality here due to the non-Gaussian conformations of chains in highly cross-linked glassy networks, steric interactions, and trapped entanglements (22,33,53). However, we have demonstrated that strain-hardening modulus increases as the cure state advances so the correlation between the large strain mechanical response and network connectivity proves to be qualitatively correct despite a quantitative discrepancy.

In order to compare the  $M_c$  calculated from the mechanical response with another method that is valid over a wide range of cure conditions, a semi-empirical calculation of  $M_c$  based on  $T_g$  can be used (Equation 1-6).

$$M_c = \frac{\zeta}{T_g - T_{g\infty}} \quad [1-6]$$

Where  $\zeta$  is a cross-link mobility parameter taken to be equal to  $39 \text{ kg}\cdot\text{K}\cdot\text{mol}^{-1}$ , and  $T_{g\infty}=311\text{K}$  is the  $T_g$  of the linear epoxy/amine analog of infinite molecular weight (i.e. difunctional amine cured epoxy resin) (56,57). Figure 1-6b shows that the trends between  $M_c$  and  $T_g$  from the two methods are in excellent qualitative agreement, however the  $M_c$  values differ by a factor of approximately 100. Previous work in our group has shown that this factor decreases as the test temperature approaches and exceeds the  $T_g$  of epoxy networks with stoichiometrically controlled  $M_c$  (18). Unfortunately, the partially cured resins treated here cannot be tested at elevated temperatures because curing proceeds rapidly above  $T_g$ .

## Strain Localization

The decrease in stress after yielding, mentioned above, is the macroscopic manifestation of localized deformation, which is initiated by the response of microscopic defects to loading. Localized regions of flowing material behave in a softer manner than the surrounding undeformed material. However, the softening is balanced by strain hardening. Flow-induced orientation causes deformed material to become stiffer. Thus the deformation zones expand to include more material. The balance of the softening and hardening responses greatly affects material responses, as Govaert *et al* demonstrated in their illustrative work on polystyrene and polycarbonate (3). In compression, polystyrene typically has a decrease in stress after yield ( $K_y=1.6$ ) and a low strain hardening modulus. Polycarbonate also has a significant drop in stress after yield ( $K_y=1.4$ ), but the ratio of its strain hardening modulus to its rejuvenated stress is much higher than that of polystyrene. The result is that strain is much more localized in polystyrene than in polycarbonate, which qualitatively changes which deformation mechanisms are activated.

An early treatment of strain localization was Haward's necking stability analysis (52). He considered the relationship between rejuvenated stress and strain-hardening modulus in tension. Equation 1-7 is the equation presented by Haward (52) and adjusted by van Melick (3) which predicts the stability of a neck.

$$\frac{\sigma_r}{G_R} = \frac{\lambda^2 - 1/\lambda}{K_y \lambda - 1} \quad [1-7]$$

where  $\sigma_r$  is the rejuvenated stress,  $G_R$  is the strain-hardening modulus,  $\lambda$  is the extension ratio of material in the neck, and  $K_y$  is the strain localization constant, which were all defined in previous sections. Figure 1-7 is a contour map which predicts qualitative

deformation behavior of isothermal and ramp cured epoxies in tension (after van Melick *et al* (3) and Haward (52) ). The data points on the graph represent the intersection of the equilibrium ( $K_y$ ) lines and the values of  $\sigma_r/G_R$  determined from compression tests according to Equation 1-7. The values of  $\lambda$  corresponding to the data points are the predicted extension ratios of material in a neck necessary to stabilize the neck.

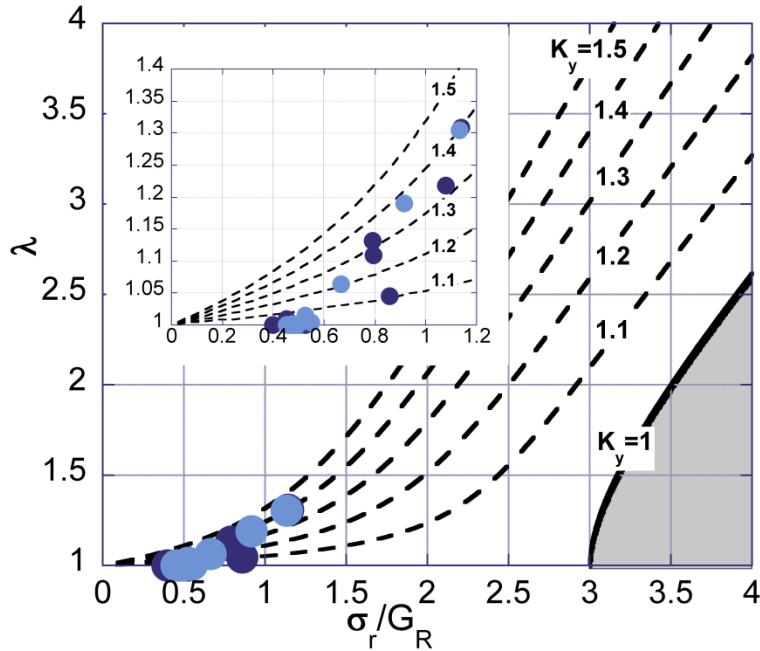


**Figure 1-7. Necking stability contour map. Values of  $\lambda$  were calculated by solving Equation 1-7. Inset expands the region containing experimental data.  $K_y$  equilibrium isolines are labeled with  $K_y$  values, and  $K_y$ ,  $\sigma_r$ , and  $G_R$  are measured from compression tests.**

As  $K_y$  increases the extension ratio necessary to stabilize a neck increases. Therefore, physical ageing, which increases  $K_y$ , imposes a more severe orientation requirement on a material. In the absence of physical ageing (i.e.  $K_y$  equal to 1) necking behavior depends only on  $\sigma_r/G_R$ . In that case, if  $\sigma_r/G_R < 3$  deformation is intrinsically affine, whereas if  $\sigma_r/G_R > 3$  the material will form a stable neck. Most polymers in the glassy state have a value of  $K_y > 1$ , and this strain localization promotes the formation of a neck in tension. The greater  $K_y$  is, the greater the orientation in the neck. Certain thermo-mechanical

histories will either promote or inhibit necking. For example, mechanically deforming PVC, polycarbonate, or polystyrene in the glassy state has been shown to temporarily prevent necking (1,3,44,52). Conversely, physically ageing polymers by annealing them for long times at temperatures below  $T_g$  has been shown to increase  $K_y$ , and thus promote strain localization in the form of a more highly oriented neck (5).

The epoxy resins treated here are glassy thermosets with values of  $K_y$  between 1 and 1.5, and  $\sigma_r/G_R$  less than 1.5. The fully cured resins have  $K_y$  equal to 1. Therefore, the plot predicts they will undergo affine deformation in tension. Resins with  $T_g$  less than  $145^\circ\text{C}$  have  $K_y$  values ranging up to about 1.6 (Figure 1-5d). Therefore, the plot predicts they should form stable necks in tension at relatively low extension ratios. In practice stable necking is not observed. The maximum extension ratio observed in tension with these resins is  $\lambda \approx 1.05$ . Strain localization activates mode I failure at very low macroscopic strains when these resins are loaded in tension. Therefore, they tend to fail before they can achieve extension ratios where necking might be stabilized. Other workers have demonstrated that tensile testing conducted at elevated temperatures approaching  $T_g$  allows cross-linked epoxies to be deformed beyond the yield point (16).

### **Shear Band Stability**

It is well established that shear band formation and necking are phenomena that arise in glassy polymers from a material instability (strain softening followed by subsequent strain hardening) after the polymer yields. In the case of neck formation, the material instability is compounded with a geometric instability. As mentioned above, loading in compression suppresses mode I failure, allowing otherwise brittle materials to be taken to higher strains where yield and post-yield behavior can be characterized.

However, loading in compression also eliminates the geometric instability that causes necking. Therefore, the predominant deformation mechanism in compression is shear banding.

Haward and others (3,52) have established stability conditions for neck formation based on establishing equilibrium across the necked and un-necked regions, respectively. Their result provides conditions for neck formation in terms of the extension ratio ( $\lambda$ ) and other characteristics of the post yield response of the polymer (see Equation 1-7 above). In what follows, we extend the concept by applying the same approach for the stability of a shear band.

For the case of a shear band, the force balance between the applied far-field shear stress and the true shear stress in the shear band is given by Equation 1-8.

$$\tau_0 A_0 = \tau A \quad [1-8]$$

where  $A_0$  is the initial cross-sectional area, and  $A$  is the instantaneous cross-sectional area. From rubber elasticity, Equation 1-9 describes a generalized strain energy function ( $F$ ), where  $G$  is the strain-hardening modulus and  $\lambda_1$ ,  $\lambda_2$ , and  $\lambda_3$  are the extension ratios.

$$F = \frac{1}{2} G (\lambda_1^2 + \lambda_2^2 + \lambda_3^2 - 3) \quad [1-9]$$

$$\lambda_1 = \lambda, \lambda_2 = 1, \lambda_3 = \frac{1}{\lambda} \quad [1-10]$$

In a shear band we define the strain as occurring at constant volume ( $\lambda_1 \lambda_2 \lambda_3 = 1$ ) in a plane according to Equation 1-10. Applying these constraints to equation 1-9, and combining terms we get our strain energy function (Equation 1-11).

$$F = \frac{1}{2} G \left( \lambda - \frac{1}{\lambda} \right)^2 \quad [1-11]$$

The engineering stress ( $\sigma_e$ ) is given by Equation 1-12.

$$\sigma_e = \frac{\partial F}{\partial \lambda} \quad [1-12]$$

However, we are interested in the shear stress ( $\tau$ ).

$$\tau = \frac{\partial F}{\partial \gamma} \quad [1-13]$$

where

$$\gamma = \left( \lambda - \frac{1}{\lambda} \right) \quad [1-14]$$

such that

$$\tau = \frac{\partial}{\partial \gamma} \left( \frac{1}{2} G \gamma^2 \right) \quad [1-15]$$

Thus, the shear stress ( $\tau$ ) is given by Equation 1-16.

$$\tau = G\gamma = G \left( \lambda - \frac{1}{\lambda} \right) \quad [1-16]$$

Following the approach of Haward (52),

$$\tau_y = \tau_r + G \left( \lambda - \frac{1}{\lambda} \right) \quad [1-17]$$

where  $\tau_y$  is the shear yield stress and  $\tau_r$  is the rejuvenated shear stress. We can relate  $\tau_y$  and  $\tau_r$  through the physical ageing constant ( $K_y$ ).

$$\tau_y = K_y \tau_r \quad [1-18]$$

By rearranging Equation 18 and substituting for  $\tau_y$ , we get

$$\frac{\tau_r}{G} = \frac{\left( \lambda - \frac{1}{\lambda} \right)}{K_y - 1} \quad [1-19]$$

Following a von Mises yield condition, the octahedral shear stress ( $\tau^{\text{oct}}$ ) is calculated according to Equation 1-20, and we can describe the shear stress in the rejuvenated regime in terms of the rejuvenated stress (Equation 1-21).

$$\tau^{\text{oct}} \equiv \frac{1}{3} \sqrt{(\sigma_1 - \sigma_2)^2 + (\sigma_2 - \sigma_3)^2 + (\sigma_3 - \sigma_1)^2} \quad [1-20]$$

$$\tau^{\text{oct}} = \frac{\sqrt{2}}{3} \sigma_r = \tau_r \quad [1-21]$$

Substituting for  $\tau_r$  in Equation 1-19 we obtain Equation 1-22, the shear band stability equation.

$$\frac{\sqrt{2}}{3} \frac{\sigma_r}{G} = \frac{(\lambda - 1/\lambda)}{K_y - 1} \quad [1-22]$$

The level of orientation required to stabilize shear bands in a given network is lower than that required for necking stability. Whereas the epoxy resins treated here are incapable of forming necks at the test temperature and strain rate used, the less stringent critical extension ratio requirements for shear banding could allow some resins to stabilize shear bands. To test the shear banding theory, samples were machined into notched rectangular compression specimens and tested in compression along the long axis of the specimens as depicted in Figure 1-8a.

In order to calculate the local shear strain a series of calibration lines were scratched into the surface of each sample perpendicular to the plane of shear. The local shear strain is calculated by dividing the displacement of each line in the direction of shear by the breadth of the sheared region according to Equation 1-23,

$$\gamma_{12} = \frac{u_{12}}{x_2} \quad [1-23]$$

where  $\gamma_{12}$  is the shear strain,  $u_{12}$  is the deformation along the plane of shear, and  $x_2$  is the width of the sheared region. Figure 1-8b shows the plastically deformed regions of a shear sample before and after loading as seen under circularly polarized light.

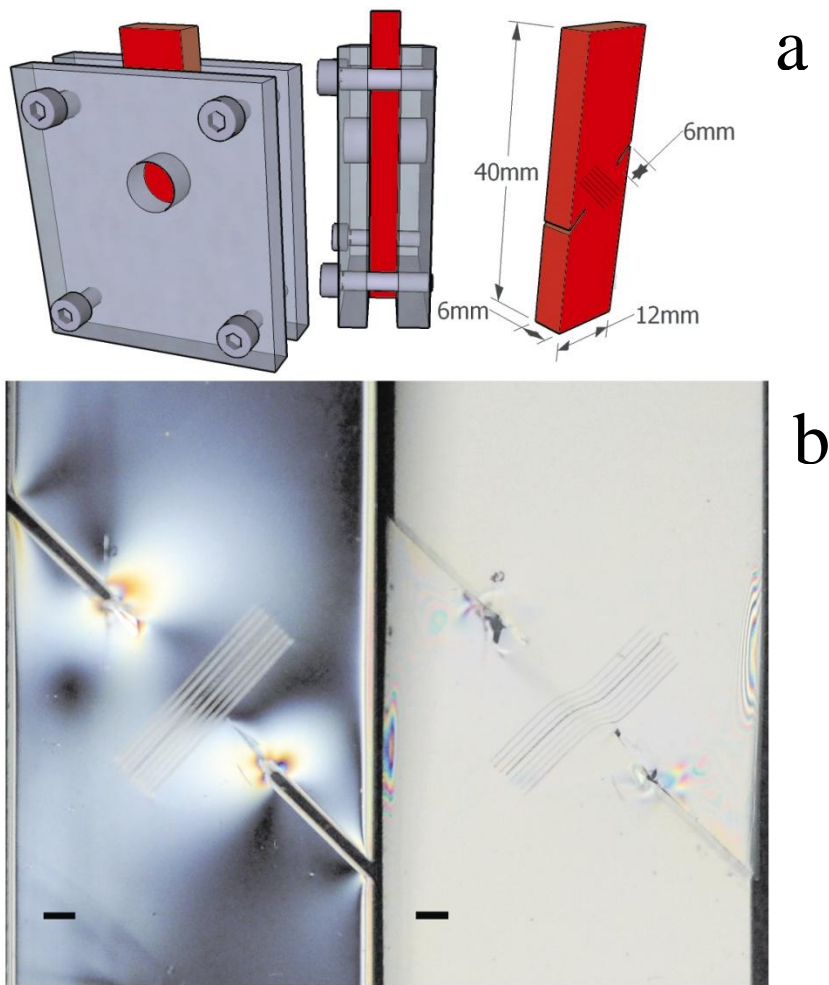


**Figure 1-8. a) Shear band support fixture and sample. b) Shear sample before (left) and after (right) testing. Scale bar is 1mm.**

Resins fabricated with various cure conditions were tested in order to determine the differences in shearing characteristics as a function of  $T_g$ . Highly undercured resins with  $T_g$  less than  $60^\circ\text{C}$  were unable to achieve yield in shear. Axial cracking dominated the deformation beyond the initial elastic deformation with no formation of shear bands. Resins with  $T_g$  greater than  $80^\circ\text{C}$  were able to achieve measurable shear strains along a shear band between the pre-cracked notches as observed in Figure 1-8b.

The resins that did not achieve yield are also unable to support the orientation required to stabilize shear bands. According to the trends of both  $\sigma_y$  and  $G_R$  versus  $T_g$ , the

resins which were unable to sustain plastic flow, even in compression, should have high yield stresses and very low strain hardening moduli. Therefore, strain localization should be quite severe in these resins, leading to fracture at low deformation, which we observe in compression testing. There appears to be a threshold of network formation necessary to support macroscopic non-linear deformation. In this work the threshold appears to be a  $T_g$  of approximately  $50^\circ\text{C}$ , which corresponds to a conversion of  $\chi \approx 0.6$  (i.e. the gel point).

Figure 1-9 is a map of the shear band stability calculated from Equation 1-22. Similar to the necking stability map in Figure 1-7, the data points in Figure 1-9 represent the intersection of the equilibrium ( $K_y$ ) lines and the values of  $\sigma_r/G_R$  determined from compression tests according to Equation 1-22. The values of  $\lambda$  corresponding to the data points are the critical extension ratios of material in a shear band necessary to stabilize the shear band. As  $K_y$  increases, the extension ratio necessary to stabilize a shear band increases, although less severely than for necking stability. Therefore, physical ageing, which increases  $K_y$ , imposes a more severe orientation requirement on material in a shear band. In the limit of no physical ageing (i.e.  $K_y$  equal to 1) the model predicts  $\lambda$  in the shear band to be equal to 1. This implies that rejuvenated polymers and cross-linked polymers above  $T_g$  should not undergo shear banding. Therefore, affine deformation is predicted in the case where  $K_y$  is equal to 1. Figure 1-9 shows that the measured values of  $\lambda$  from the shear test are higher than the predicted critical values calculated from compression data using Equation 1-22. This discrepancy suggests that material in the shear bands continues to orient beyond the critical extension ratio as deformation proceeds. One possible explanation for the excessive orientation behavior is local viscous heating caused by the flow.

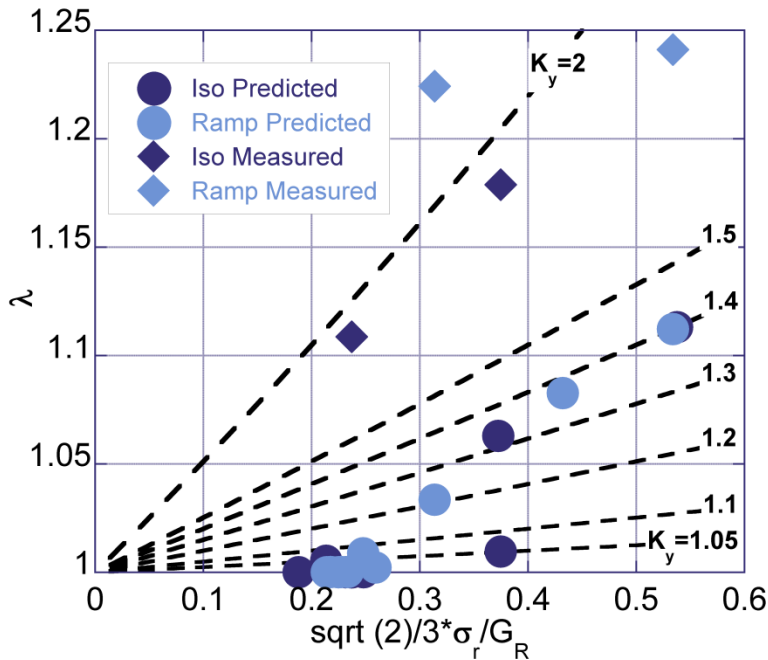


Figure 1-9. Shear band stability map. Values of  $\lambda$  are predicted by solving Equation 1-22.  $K_y$  equilibrium isolines are labeled with  $K_y$  values, and  $K_y$ ,  $\sigma_r$ , and  $G_R$  are measured from compression tests.

Other workers have shown that  $\sigma_r$  decreases as temperature increases (3,18,33,48,58,59).

The localized heating would increase the critical level of orientation of material in the shear band due to decreases in yield and rejuvenated stresses at higher temperatures.

However, material outside of the shear band would not be heated so it would still require the higher stresses associated with cooler temperatures before being incorporated into the shear band. This rationalization is also dependent on strain rate and test temperature.

Although local heating is a plausible explanation for the observed behavior, more work is needed to rigorously determine the deviations from the predicted behavior.

## Conclusions

This study analyzes network formation of two series of partially cured stoichiometric epoxy-amine resins using thermal, mechanical, and physical probes. By systematically varying the cure states of the resins using an isothermal and a ramp cure

condition we were able to map the mechanical responses of the resins at various stages of network formation.  $T_g$  was used as a metric of network formation due to its sensitivity to changes in network connectivity, particularly at high conversion. The physical and mechanical properties that are sensitive to molecular packing, such as density, compressive modulus, and yield stress were shown to be highly dependent on  $T_g$  as well. Qualitative changes in the density and yield stress were observed in the vicinity the gel point. The trends in the deformation behavior demonstrated inverse relationship between characteristics of physical ageing and network formation in terms of mechanical properties. The decrease in segmental mobility associated with physical ageing was attributed to the enhanced ability of unreacted amine and epoxide groups to pack within the network. Taking resins to full cure by either an initial high temperature cure or a high temperature post-cure was shown to remove any artifacts of physical ageing regardless of the initial cure state. High temperature curing also led to a decrease in room temperature density, consistent with the idea that the topologically constrained network is locked into a low density configuration when it is cooled in the glassy state. The result of advancing the cure state of a resin is the inhibition of physical ageing as measured by decreases in density, modulus, yield stress, and the strain localization constant.

The large-strain responses of the networks in the post-yield regime were found to have little dependence on cure path, whereas they showed strong dependences on network connectivity. The rejuvenated stress was found to be highly correlated with  $T_g$ , and insensitive to the cure path. The strain-hardening modulus increased linearly with  $T_g$ . The trends between  $M_c$  and  $T_g$ , where  $M_c$  was calculated using a mechanical and a thermal method, respectively, were in excellent qualitative agreement with each other.

However, the mechanical characterization underestimates  $M_c$  by a factor of approximately 100. This quantitative difference between  $M_c$  values is associated with the mechanical characterization of densely cross-linked epoxies in the glassy state.

The data from this work were also applied to two analyses of deformation instabilities. The resins were predicted to be able to stabilize necking in tensile tests, however mode I failure occurred before necking could be observed. When we applied our results to a shear banding stability model developed by our group, we found the resins were able to achieve sufficient extension ratios along a shear band to allow propagation of shear bands through the samples. In both necking and shear banding analyses decreases in the degree of strain localization were associated with increases in network formation in the epoxy resins.

## **References**

1. Cross A, Haward RN. Orientation hardening of PVC. *Polymer*. 1978; 19: p. 677.
2. Struik LCE. *Physical Ageing of Amorphous Polymers and Other Materials* Amsterdam: Elsevier; 1978.
3. van Melick HGH, Govaert LE, Meijer HEH. On the origin of strain hardening in glassy polymers. *Polymer*. 2003; 44: p. 2493-2502.
4. McKenna GB. Mechanical rejuvenation in polymer glasses: fact or fallacy? *Journal of Physics: Condensed Matter*. 2003; 15(11): p. 737-763.
5. Klompen ETJ, Engels TAP, Govaert LE, Meijer HEH. Modeling of the postyield response of glassy polymers: influence of thermomechanical history. *Macromolecules*. 2005; 38: p. 6997-7008.
6. Ellis B. *Chemistry and Technology of Epoxy Resins* New York: Chapman and Hall; 1993.
7. Lee A, McKenna GB. Effect of crosslink density on physical ageing of epoxy networks. *Polymer*. 1988; 29: p. 1812-1817.

8. Wang X, Gillham JK. Physical aging in the glassy state of a thermosetting system vs. extent of cure. *Journal of Applied Polymer Science*. 1993; 47: p. 447-460.
9. G'Sell C, McKenna GB. Influence of physical ageing on the yield response of model DGEBA/poly(propylene oxide) epoxy glasses. *Polymer*. 1992; 33(10): p. 2103-2113.
10. Detwiler AT, Lesser AJ. Aspects of network formation in glassy thermosets. *Journal of Applied Polymer Science*. 2010; 117: p. 1021-1034.
11. White SR, Mather PT, Smith MJ. Characterization of the cure state of DGEBA-DDS epoxy using ultrasonic, dynamic mechanical, and thermal probes. *Polymer Engineering and Science*. 2002; 42(1): p. 51-67.
12. Rana D, Sauvant V, Halary JL. Molecular analysis of yielding in pure and antiplasticized epoxy-amine thermosets. *Journal of Materials Science*. 2002; 37: p. 5267.
13. Wang X, Gillham JK. Tg-temperature property (TgTP) diagram for thermosetting systems: Anomalous behavior of physical properties vs. extent of cure. *Journal of Applied Polymer Science*. 1993; 47: p. 425-446.
14. Montserrat S. Vitrification and further structural relaxation in the isothermal curing of an epoxy resin. *Journal of Applied Polymer Science*. 1992; 44: p. 545.
15. Cook WD, Scott TF, Quay-Thevenon S, Forsythe JS. Dynamic mechanical thermal analysis of thermally stable and thermally reactive network polymers. *Journal of Applied Polymer Science*. 2004; 93: p. 1349-1359.
16. Tcharkhtchi A, Trotignon JP, Verdu J. Yielding and fracture in crosslinked epoxies. *Macromolecular Symposia*. 1999; 147: p. 221.
17. Madsen PA, Foister RT. Network structure and properties of imidazole-cured epoxy novolac adhesives. *Journal of Applied Polymer Science*. 1989; 37: p. 1931.
18. Calzia KJ, Lesser AJ. Post-Yield Deformation of Glassy Networks: Effects of Molecular Architecture. In ANTEC; 2006; Charlotte, NC.
19. Wang X, Gillham JK. Analysis of crosslinking in amine-cured epoxy systems: The one-to-one relationship between Tg and conversion. *Journal of Applied Polymer Science*. 1992; 45: p. 2127.

20. Jordan C, Galy J, Pascualt JP. Measurement of the extent of reaction of an epoxy-cycloaliphatic amine system and influence of the extent of reaction on its dynamic and static mechanical properties. *Journal of Applied Polymer Science*. 1992; 46: p. 859-871.
21. Verchere D, Sautereau H, Pascualt JP, Riccardi CC, Moschiar SM, Williams RJJ. Buildup of epoxy-cycloaliphatic amine networks. Kinetics, vitrification, and gelation. *Macromolecules*. 1990; 23: p. 725-731.
22. Charlesworth JM. Effect of cross-link density on the molecular relaxations in diepoxide-diamine network polymers 1. The glassy region. *Polymer Engineering and Science*. 1988; 28(4): p. 221-229.
23. Matejka L. Amine Cured Epoxide Networks: Formation, Structure, and Properties. *Macromolecules*. 2000; 33: p. 3611-3619.
24. Flory PJ. Molecular Size Distribution in Three Dimensional Polymers. I. Gelation. *Journal of the American Chemical Society*. 1941; 63: p. 3083-3090.
25. Flory PJ. *Principles of Polymer Chemistry* Ithaca: Cornell University Press; 1953.
26. Swier S, Van Assche G, Van Mele B. Reaction kinetics modeling and thermal properties of epoxy-amines as measured by modulated-temperature DSC. I. Linear step-growth polymerization of DGEBA + aniline. *Journal of Applied Polymer Science*. 2004; 91: p. 2798-2813.
27. Wang X, Gillham JK. Competitive Primary Amine/ Epoxy and Secondary Amine/Epoxy Reactions: Effect on the Isothermal Time-to-Vitrify. *Journal of Applied Polymer Science*. 1991; 43: p. 2267-2277.
28. Pang KP, Gillham JK. Anomalous behavior of cured epoxy resins: density at room temperature versus time and temperature of cure. *Journal of Applied Polymer Science*. 1989; 37: p. 1969-1991.
29. Ellis B, Found MS, Bell JR. Effects of cure treatment on glass transition temperatures for a BADGE-DDM epoxy resin. *Journal of Applied Polymer Science*. 1996; 59: p. 1493-1505.
30. Brady RF. Volume change in the polymerization of spirocyclic monomers - Causes, Effects, and Applications. *Journal of Macromolecular Science-Reviews in Macromolecular Chemistry and Physics*. 1992; C32: p. 135-181.

31. Shimbo M, Ochi M, Shigeta Y. Shrinkage and internal stress during curing of epoxide resins. *Journal of Applied Polymer Science*. 1981; 26: p. 2265-2277.
32. Varley RJ, Hodgkin JH, Simon GP. Toughening of trifunctional epoxy system. V. Structure-property relationships of neat resin. *Journal of Applied Polymer Science*. 2000; 77: p. 237-248.
33. Ferry JD. *Viscoelastic Properties of Polymers* New York: Wiley; 1980.
34. Venditti RA, Gillham JK, Jean YC, Lou Y. Free volume after cure vs. fractional conversion for a high-Tg epoxy/amine thermosetting system. *Journal of Applied Polymer Science*. 1995; 56: p. 1207-1220.
35. Kovacs AJ, Stratton RA, Ferry JD. Dynamic mechanical properties of polyvinyl acetate in shear in the glass transition temperature range. *Journal of Physical Chemistry*. 1963; 67: p. 152-161.
36. Johari GP. In Richert R, Blumen A, editors. *Disorder Effects on Relaxational Processes*. New York: Springer-Verlag; 1994. p. 627-657.
37. Haward RN, Young RJ. *The Physics of Glassy Polymers* New York: Chapman and Hall; 1997.
38. Halar J. Structure-Property Relationships in Epoxy-Amine Networks of Well-Controlled Architecture. *High Performance Polymers*. 2000; 12: p. 141-153.
39. Enns JB, Gillham JK. Effect of the extent of cure on the modulus, glass transition, water absorption, and density of an amine-cured epoxy. *Journal of Applied Polymer Science*. 1983; 28: p. 2831-2846.
40. Robertson RE. Theory for the Plasticity of Glassy Polymers. *The Journal of Chemical Physics*. 1966; 44(10): p. 3950-3956.
41. Golden JH, Hammant BL, Hazell EA. The effect of thermal pretreatment on the strength of polycarbonate. *Journal of Applied Polymer Science*. 1967; 11: p. 1571-1579.
42. Vardoulakis I, Labuz JF, Papamichos E, Tronvoll J. Continuum fracture mechanics of uniaxial compression on brittle materials. *International Journal of Solids and Structures*. 1998; 35: p. 4313.

43. Oyanguren PA, Vallo CI, Frontini PM, Williams RJJ. Rejuvenation of epoxy glasses subjected to uniaxial compression. *Polymer*. 1994; 35: p. 5279-5282.
44. Tervoort TA, Govaert LE. Strain hardening behavior in polycarbonate in the glassy state. *Journal of Rheology*. 2000; 44(6): p. 1263-1277.
45. Govaert LE, van Melick HGH, Meijer HEH. Temporary toughening of polystyrene through mechanical. *Polymer*. 2001; 42: p. 1271-1274.
46. van Melick HGH, Govaert LE, Raas B, Nauta WJ, Meijer HEH. Kinetics of ageing and re-embrittlement of mechanically. *Polymer*. 2003; 44: p. 1171-1179.
47. Hoy RS, Robbins MO. Strain hardening of polymer glasses: Effect of entanglement density, temperature, and rate. *Journal of Polymer Science: Part B: Polymer Physics*. 2006; 44: p. 3487-3500.
48. Boyce MC, Arruda EM. Constitutive models of rubber elasticity: A review. *Rubber Chemistry and Technology*. 2000; 73(3): p. 504-523.
49. Treloar LRG. *The Physics of Rubber Elasticity* Oxford: Clarendon Press; 1975.
50. Wang X, Foltz VJ. Crosslinking induced volume expansion in the glass state. *Polymer*. 2006; 47: p. 5090-5096.
51. Boyce MC, Arruda EM. An Experimental and Analytical Investigation of the Large Strain Compressive and Tensile Response of Glassy Polymers. *Polymer Engineering and Science*. 1990; 30(20): p. 12888-1298.
52. Haward RN. The application of a simplified model for the stress-strain curves of polymers. *Polymer*. 1987; 28: p. 1485.
53. Charlesworth JM. Effect of cross-link density on molecular relaxations in diepoxide-diamine network polymers 2. The rubbery plateau region. *Polymer Engineering and Science*. 1988; 28(4): p. 230-236.
54. Haward RN, Thackray G. The use of a mathematical model to describe isothermal stress-strain curves in glassy thermoplastics. *Proceedings of the Royal Society of London Series A*. 1968; 302: p. 453-472.
55. Lesser AJ, Crawford E. The role of network architecture on the glass transition temperature of epoxy resins. *Journal of Applied Polymer Science*. 1997; 66: p. 387-395.

56. Crawford ED, Lesser AJ. The effect of network architecture on the thermal and mechanical behavior of epoxy resins. *Journal of Polymer Science: Part B: Polymer Physics*. 1998; 36: p. 1371-82.
57. Crawford ED, Lesser AJ. Brittle to ductile: Fracture toughness mapping on controlled epoxy networks. *Polymer Engineering and Science*. 1999; 39: p. 385-392.
58. Arruda EM, Boyce MC, Jayachandran R. Effects of strain rate, temperature and thermomechanical coupling on the finite strain deformation of glassy polymers. *Mechanics of Materials*. 1995; 19: p. 193-212.
59. Kontou E. Modeling of postyield behavior of glassy polymers. *Journal of Applied Polymer Science*. 1996; 61: p. 2191-2195.

## CHAPTER 2

# MOLECULAR ASPECTS OF FRACTURE AND SELF-HEALING IN GLASSY THERMOSETS

### **Abstract**

The fracture and healing behavior of model amine cured epoxy resins with controlled network architectures is reported. The conversions and cross-link densities of the networks are controlled through the processing conditions and by varying the ratio of cross-linker to chain extender. The fracture toughness of virgin partially cured networks as well as healed networks is found to increase with cross-link density according to a network percolation model. Virgin fully cured networks are found to have much higher fracture toughness than partially cured networks with similar cross-link densities. The relationship between the non-linear fracture energy release rate and the molecular parameters of virgin and healed networks is captured by an effective crack length model. The inelastic component of the fracture energy release rate is attributed to the failure of network strands in a cohesive zone at the crack tip. The physical and mechanical properties of the material in the cohesive zone are calculated from a network percolation model. Excellent agreement between the fracture model and experimental data are obtained across four orders of magnitude of fracture energy release rates.

### **Introduction**

Materials that are able to be repaired without being replaced are attractive for many coatings and structural applications. There have been a number of different strategies developed to achieve healing in polymeric systems, and several reviews have recently been published (1,2,3,4,5). Perhaps the simplest method, commonly used with

thermoplastics, is to simply heat materials above their  $T_g$  or melting temperature and allow the chains to diffuse across the crack interface (6). This method, along with solvent welding and other diffusion based techniques, ostensibly have limited applicability to highly cross-linked thermosets due to the inherently short nature of chain ends at a crack interface. Other methods employ advanced chemistries that are capable of undergoing reverse reactions under certain conditions (7,8). Engineering approaches have incorporated capsules (9) or hollow fibers containing healing fluids that mimic vascular systems found in plants and animals (10). In general, these approaches employ thermosetting materials to generate the healing response.

The healing abilities of thermosetting resins themselves are of particular interest in structural adhesives and composites. However, glassy thermosets are often very brittle even before any healing procedures are attempted. A significant amount of work has been published on relationships between fracture properties and molecular weight between cross-links ( $M_c$ ) or, similarly, cross-link density ( $\nu$ ) in fully cured thermosets (11,12,13,14). However, much less work has considered partially cured resins (15,16). Before reaching the gel point thermosets are generally extremely brittle. Beyond the gel point fracture toughness has been reported to increase slightly, decrease slightly, or remain relatively constant as a function of conversion (15,16,17). These varied results can be attributed to a number of parameters that change during cure including modulus, yield stress, the strength of the  $\beta$ -transition, and cross-link density. LeMay and Kelley found a  $G \sim \nu^{-1/2}$  dependence for arrest fracture energies for a series of fully cured glassy DGEBA-DDS networks (13), which shows the same cross-link density dependence as the work of Lake and Thomas regarding tearing energy in elastomers (18). Other work by

Crawford and Lesser has investigated fracture toughness and critical crack tip opening displacement (COD) as a function of  $v$  and backbone stiffness (19,12). They found that  $\delta_c$  scaled with  $v^{-1}$  and  $\sigma_y^{-1}$ , as predicted by a Dugdale-Barenblatt cohesive zone model.

The healing behavior of cross-linked networks has received much less attention than the fracture behavior of virgin networks. In the absence of additional adhesives it is not clear how healing might occur in highly cross-linked vinyl esters or epoxies (20,21). In contrast to thermoplastics, thermosets have very short chain ends, so the diffusion mechanisms that can lead to cohesive strength from molecular entanglements are absent in thermosets. However, this also means that thermosets can make good model systems because the healing response becomes much simpler in the absence of the diffusion of chain segments that are capable of entangling. The majority of the healing response is expected to derive from chemical reactions. Therefore, by controlling the initial conversion of a thermosetting material, the residual functionality available for healing can be controlled. In this work we characterize some of the fundamental relationships between network structure, fracture, and healing of model epoxy networks by varying cross-link density, monomer chemistry, and curing conditions. More specifically, we analyze the contributions of residual functionality to the fracture properties of networks in the virgin and healed condition.

## **Method**

The epoxide monomer used in this work is D.E.R. 332, a purified diglycidylether of bisphenol A (DGEBA) with a degree of polymerization of  $n=0.03$  and epoxide equivalent weight of 175g/mol, provided by Dow. The epoxide monomer is stirred under vacuum at 80°C for two hours before blending. The curing agents ethylenediamine 99+%

(EDA), m-phenylenediamine 99% (mPDA) and N,N'-dimethylethylenediamine 90+% (DMEDA) are purchased from Sigma-Aldrich and used as received. The structures of all monomers can be found in Figure 2-1.

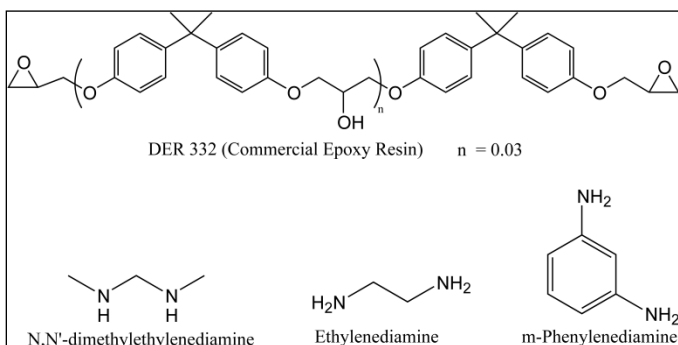


**Figure 2-1. Epoxy and amine monomers**

## Sample Preparation

Epoxy resins are prepared by mixing the DGEBA with stoichiometric amounts of the amine curing agents by stirring in a glass beaker. When a homogeneous solution is obtained (about 5 minutes of stirring) the resins are poured into cylindrical or rectangular glass molds treated with a mold release agent (Surfasil, Pierce Chemical).

The molds are placed in a 23°C water bath for several hours to control the exothermic reaction. Molds are transferred from the water bath to an oil bath at 25°C. The oil bath is then heated at a rate of 40°C per hour. At a range of different temperatures molds are removed and quenched to room temperature in water baths to give partially cured samples. The resins are stored in a freezer at -10°C to prevent further curing and to inhibit physical ageing until they are machined into compression bullets or compact tension samples.

## **Thermal Analysis**

The  $T_g$  of each resin is determined as the inflection point of the  $dH/dT$  curve from DSC heating at  $10^\circ\text{C}$  per minute in a TA Instruments DSC 2910. Conversion is measured as the integration of the exotherm in the  $dH/dT$  curve of each resin relative to that of an uncured sample.

## **Compression Testing**

Compression bullets are formed by cutting the cylinders into sections with height to diameter ratios of 1:1. Care is taken to machine the top and bottom faces of the cylinders such that they are parallel to each other and perpendicular to the sides of the cylinders. The faces are polished to give smooth, glassy surfaces. Density is measured at  $23^\circ\text{C}$  by the water displacement method (ASTM D792). Dimensions for compression testing are measured to the nearest 0.01 mm using calipers.

Immediately before compression testing a surfactant-PTFE film treatment is applied to the top and bottom surfaces of the compression specimens in order to produce a low friction surface which allows for affine deformation over a large range of strains. The samples are loaded in compression using an Instron 5800 fitted with a 50kN load cell and controlled using the Merlin software package. Samples are tested at  $20^\circ\text{C}$  and a constant true strain rate of  $0.1 \text{ min}^{-1}$  ( $1.67 \times 10^{-3} \text{ s}^{-1}$ ) is maintained during the entire test. Further details and analysis from compression testing were previously reported (22).

## **Fracture Toughness Testing**

The compact tension (CT) geometry as described in ASTM D5045 serves as the standard for fracture testing. Samples are prepared as above except the molds consist in

6mm thick PTFE spacers between 15 x 25 x 0.6 cm glass plates treated with the mold release. The specimens are machined to 5 x 6 x 0.6 cm, holes are drilled for loading pins, and a slot is cut with a diamond wafering blade. A sharp crack is produced by cooling samples to -10°C and tapping a fresh razor blade into the machined slot, thus advancing a sharp crack beyond the end of the slot. In addition, a hole 5mm in diameter is drilled in the plane of the precrack approximately 4 mm from the end of the CT specimen in order to arrest the crack during the fracture test. Arresting the crack before it propagates to the end of the CT specimen ensures that the crack faces maintain adequate registry, which aids in the intimate mating of the crack faces during healing (23). Dimensions and crack lengths are measured using calipers according to the standard. An Instron 4411 equipped with a 100N or 5kN load cell (depending on the maximum load necessary for fracture) is used to fracture the samples at a constant rate of 0.5 mm·min<sup>-1</sup>.

## **Healing**

Fractured samples are healed by placing them in spring-loaded steel frames that apply a pseudo-load controlled pressure of 0.4 MPa normal to the crack surfaces to ensure intimate contact between the fracture surfaces (24). Brass shims are inserted into the slot portion of the cracks before the healing process to prevent healing of the machined slot and unnecessary deformation. The healing frames are placed in N<sub>2</sub> purged ovens at T<sub>g</sub> + 20°C for four hours. Samples are removed from the loading frames and allowed to cool slowly to room temperature. The brass shims are removed from the machined slots and the samples are pre-cracked along the original crack interface and tested as described above.

## Results and Discussion

$K_q$  is reported for all measured fracture data instead of  $K_{IC}$  due to modifications to the compact tension specimens which deviate from the ASTM D5045 standard. The  $K_q$  values reported here are in excellent agreement with  $K_{IC}$  values reported elsewhere for comparable, fully cured epoxies (12,19).  $K_q$  is plotted versus  $T_g$  for virgin and healed networks in Figure 2-2. The data for healed networks are plotted at the  $T_g$  of the corresponding virgin networks for comparison.

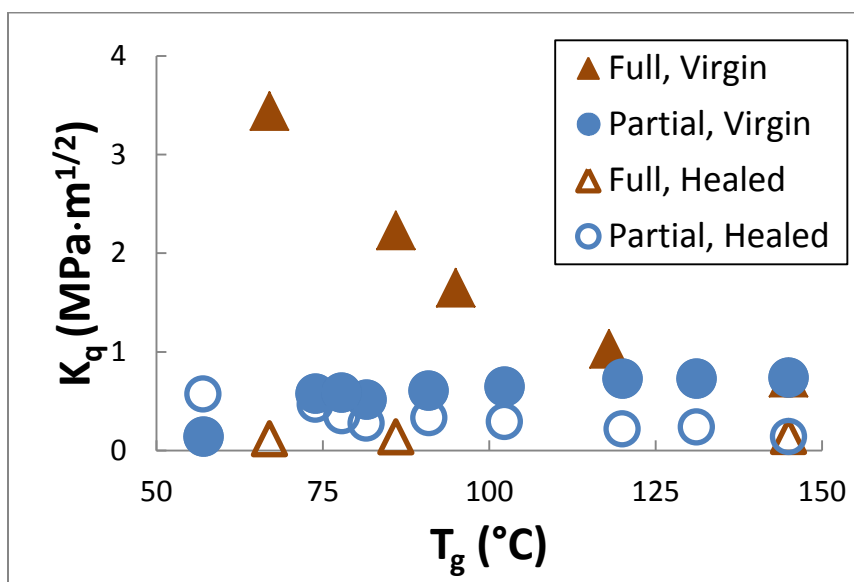


**Figure 2-2. Plot of mode I fracture toughness vs glass transition temperature. Fully cured EDA-DMEDA networks with chain extenders (brown triangles) and partially cured EDA 380 networks with no chain extenders (blue circles). Virgin networks have solid symbols and healed networks have hollow symbols. All  $K_q$  values are plotted at the  $T_g$  of the virgin networks. The partially cured networks are much weaker than fully cured chain extended networks with the same  $T_g$ . The partially cured networks recover a greater fraction of the virgin fracture toughness than the fully cured networks.**

The  $K_q$  values of the partially cured networks are surprisingly low, and they increase slightly as  $T_g$  of the partially cured networks approaches the  $T_g$  of the fully cured networks. Fully cured virgin chain extended resins show the expected large increase in fracture toughness as  $T_g$  decreases (12,13). Partially cured epoxies generally behave as antiplasticized materials with higher modulus and yield stress and lower  $T_g$  than fully

cured epoxies (15,22). They have also been shown to be susceptible to strain localization, which results from the inability of a material with a combination of high modulus, high yield stress, and low network connectivity to stabilize local strains. Therefore, partially cured epoxies are expected to be much weaker than fully cured epoxies based on the trajectories of modulus, yield stress, and network connectivity during the curing process (22). These arguments indicate a need for a full physical and mechanical characterization of partially cured epoxies in order to understand the effects of mechanical properties on fracture and healing behavior.

The measured physical and mechanical properties listed in Table 2-1 are used in the analysis of the fracture and healing data in this work. Glass transition temperature ( $T_g$ ) and conversion ( $x$ ) are measured with DSC, yield stress ( $\sigma_y$ ) and compressive modulus ( $E$ ) are measured from uniaxial compression, density ( $\rho$ ) is measured from water displacement, and fracture toughness ( $K_q$ ) is measured from compact tension specimens. Throughout this paper resins are referred to by their  $M_c$  values as calculated from stoichiometry, assuming tetrafunctional cross-links (19). Therefore, 380 refers to an epoxy resin cured with EDA only, 818 and 1452 refer to chain extended resins that are cured with a combination of EDA and DMEDA, and 404 refers to resins cured with the aromatic mPDA only. All monomers can be found in Figure 2-1. Since  $T_g$  is found to be more sensitive than conversion to the progress of network formation in partially cured resins (25,22),  $M_c$  is calculated from  $T_g$  according to Equation 2-1

$$M_c = \frac{\zeta}{T_g - T_{g\infty}} \quad [2-1]$$

where  $\zeta$  is a constant related to the decrease in entropy due to adding cross-links to a linear polymer, and  $T_{g\infty}$  is the glass transition temperature of a linear epoxy/amine chain of infinite molecular weight, i.e., difunctional amine cured epoxy resin (19,12). For the 380, 818, and 1452 resins  $\zeta = 39 \text{ kg}\cdot\text{K}\cdot\text{mol}^{-1}$  and  $T_{g\infty} = 38^\circ\text{C}$ . The values for the 404 resins are  $34 \text{ kg}\cdot\text{K}\cdot\text{mol}^{-1}$  and  $87^\circ\text{C}$ , respectively. The cross-link density is calculated from  $M_c$ , where  $v = \rho N_A / M_c$ , where  $N_A$  is Avogadro's number.

**Table 2-1. Physical and mechanical properties of epoxy-amine resins.**

Resin Description	$T_g$	$\rho$	$\sigma_y$	$x$	$E$	$v$	$K_q$ Virgin	$K_q$ Healed	$M_c$
	$^\circ\text{C}$	$\text{g}/\text{cm}^3$	$\text{MPa}$	Mol Fraction	$\text{MPa}$	$\times 10^{25} \text{ m}^{-3}$	$\text{MPa}\cdot\text{m}^{1/2}$	$\text{MPa}\cdot\text{m}^{1/2}$	$\text{g}/\text{mol}$
EDA 380	57	1.1910	102	0.63	3396	35	0.14	0.57	2053
EDA 380	74	1.1904	103	0.81	3304	66	0.58	0.47	1087
EDA 380	82	1.1907	103	0.87	3385	80	0.52	0.28	896
EDA 380	78	1.1906	102	0.82	3248	73	0.59	0.35	978
EDA 380	102	1.1906	100	0.91	3144	118	0.65	0.29	607
EDA 380	120	1.1903	100	0.96	2413	151	0.73	0.22	476
EDA 380	131	1.1904	99	0.99	2544	171	0.73	0.24	419
EDA 380	145	1.1893	102	0.999	2217	196	0.74	0.14	364
EDA-DMEDA 380	145	1.1893	102	0.999	2217	196	0.74	0.14	364
EDA-DMEDA 818	86	1.1640	76	0.999	2567	86	2.23	0.14	813
EDA-DMEDA 1452	67	1.1385	69	0.999	2468	51	3.44	0.12	1345
mPDA 404	72	1.1930	--	0.64	4017	--	0.17	0.59	--
mPDA 404	103	1.1930	118	0.82	2905	34	0.53	0.30	2087
mPDA 404	112	1.1930	117	0.83	2623	52	0.49	0.29	1369
mPDA 404	118	1.1930	117	0.86	2605	65	0.49	0.20	1099
mPDA 404	152	1.1930	116	0.94	2406	136	0.61	0.17	527
mPDA 404	182	1.1930	117	0.97	2355	201	0.66	0.07	357

It is clear from Table 2-1 that the modulus of the EDA 380 and mPDA 404 resins decreases significantly as  $T_g$  (and conversion) increase, whereas cross-link density increases with  $T_g$ . As indicated from previous work on partially cured epoxies (22), this evolution of properties suggests strain localization will decrease with increasing  $T_g$ . In fracture mechanics strain localization can be described in terms of the size of the process

zone. According to the Dugdale-Barenblatt zone model, the mode I fracture toughness ( $K_{IC}$ ) is related to the size of the cohesive zone at the crack tip by Equation 2-2.

$$r_p = \frac{\pi K_{IC}^2}{8 \sigma_y^2} \quad [2-2]$$

Where  $r_p$  is the cohesive zone radius and  $\sigma_y$  is yield stress, which is used to approximate the cohesive stress in the model (26). The size of the zone depends on the stress intensity and the cohesive stress of the material. For a material with a given fracture toughness, a decrease in the yield stress equates to an increase in the cohesive zone radius. In comparing partially cured EDA 380 networks with fully cured chain extended EDA-DMEDA networks, the yield stress becomes important to strain localization. The yield stress remains constant as a function of  $T_g$  (beyond the gel point) for partially cured networks, whereas it increases with  $T_g$  for fully cured chain extended networks. Therefore, the cohesive zones in the chain extended networks are expected to delocalize strain over a larger volume of material than in the partially cured networks. From a continuum mechanics perspective, differences in yield stress can begin to explain the low fracture toughness of partially cured epoxy networks relative to fully cured networks with similar  $T_g$ . However, in order to compare partially cured, fully cured, and healed networks, the molecular details of the networks must be incorporated into a continuum fracture model.

### **Molecular Considerations of Fracture**

The healed networks that achieved significant recovery of the virgin  $K_q$  values were initially very close to the critical conversion, so they had the most residual functionality after the initial fracture. Analysis of the fracture toughness of the healed

networks requires additional consideration of the physical properties of the networks, including network architecture. Clearly, the healed fully cured chain extended networks fail to recover a significant portion of their virgin fracture toughness. Since they do not possess any residual epoxide or amine functionality going into the healing process, there is no obvious source of a chemical reaction that would create bonds across the crack interface. The healed partially cured networks possess varying amounts of residual functionality, depending on their conversion in the virgin state. This residual functionality is capable of forming network chains across the cracked interface. However, the properties of the network near the crack interface will determine the fracture and healing behavior, and this network will be different from the bulk material after the fracture of the virgin network.

The connectivity of the network at the crack interface can be parameterized in terms of conversion ( $x$ ),  $T_g$ , and  $v$ . In a thermosetting system the connectivity percolation threshold for the network can be defined as statistical gelation using Equation 2-3 (27,28).

$$x_c = \frac{1}{[r(f_A - 1)(f_E - 1)]^{1/2}} \quad [2-3]$$

where  $x_c$  is the critical conversion,  $r$  is the stoichiometric imbalance ( $r=1$  for balanced systems),  $f_A$  is the average functionality of the amine, and  $f_E$  is the average functionality of the epoxide. Using tetrafunctional amines to cure difunctional epoxy resins gives a critical conversion of  $x_c=0.58$ . Below  $x_c$ , van der Waals forces are responsible for the majority of the cohesive strength of the material. However, in the vicinity of the critical conversion the network begins to percolate such that covalent

bonds form continuous structures throughout the entire material. As the conversion continues to increase above  $x_c$  the number of covalently bound network chains crossing a given plane in the material increases until complete conversion at  $x=1$ .

We extend the conceptual approach proposed by Wool (29), which relates the strain energy density ( $U$ ) in the system to the energy density stored in a percolated network (Equation 2-4).

$$U = \frac{\sigma^2}{2E} = D_0 v (p - p_c) \quad [2-4]$$

where  $U$  is the strain energy per unit volume,  $\sigma$  is the applied far-field stress,  $E$  is the elastic modulus,  $v$  is the cross-link density of a fully cured network,  $p$  is the fraction of bonds that are broken during fracture,  $p_c$  is the critical fraction of broken bonds necessary for failure, and  $D_0$  is the bond energy. For a typical carbon-carbon bond the bond energy is approximately 350 kJ/mol (30). In order for fracture to occur, a fraction ( $p-p_c$ ) of the bonds in a given volume must be broken. In a cross-linked epoxy  $p$  is equivalent to conversion ( $x$ ) and  $p_c$  is equivalent to  $x_c$ . Wool relates the stress at fracture ( $\sigma_c$ ) to molecular characteristics by rearranging Equation 2-4 to obtain Equation 2-5.

$$\sigma_c = [2ED_0 v (x - x_c)]^{1/2} \quad [2-5]$$

Equation 2-5 gives the stress required to fracture enough network bonds to cause macroscopic failure of the network.

We extend the concepts proposed by Wool to describe partially cured, fully cured, and healed systems by introducing the term  $v^*$  in Equation 2-6 to replace  $v(x-x_c)$  from Equation 2-5.

$$\sigma_c \sim [E\nu^*]^{1/2} \quad [2-6]$$

Where  $\nu^* = \nu(x - x_c)$  for partially cured networks,  $\nu^* = \nu(1 - x_c)$  for fully cured networks, and  $\nu^* = \nu(1 - x)$  for healed networks. In all cases, the initial conversion ( $x$ ) must be greater than the critical conversion ( $x_c$ ), such that a percolated network is formed. The percolation cross-link density ( $\nu^*$ ) essentially only counts the cross-links that exceed the critical threshold necessary for percolation because any cross-links which are connected to chains that do not percolate through the material are not involved in the transfer of stress along covalent bonds from one side of a potential crack plane to the other.

We then adopt a description of an effective crack length model, as described by Williams (26), which allows linear fracture mechanics to be extended to describe non-linear phenomenon in cases where the cohesive zone is small relative to the crack length, (i.e. where small-scale yielding applies).

$$\frac{J}{G} = \left[ 1 - \alpha \left( \frac{\sigma_c}{\sigma_y} \right)^2 \right]^{-1} \quad [2-7]$$

Where  $J$  is the total non-linear fracture energy,  $G$  is the mode I linear elastic fracture energy, and  $\alpha$  is a cohesive zone shape parameter.  $G$  is calculated from the fracture toughness and the modulus for plane strain conditions.

$$G = \frac{K^2(1 - \mu^2)}{E} \quad [2-8]$$

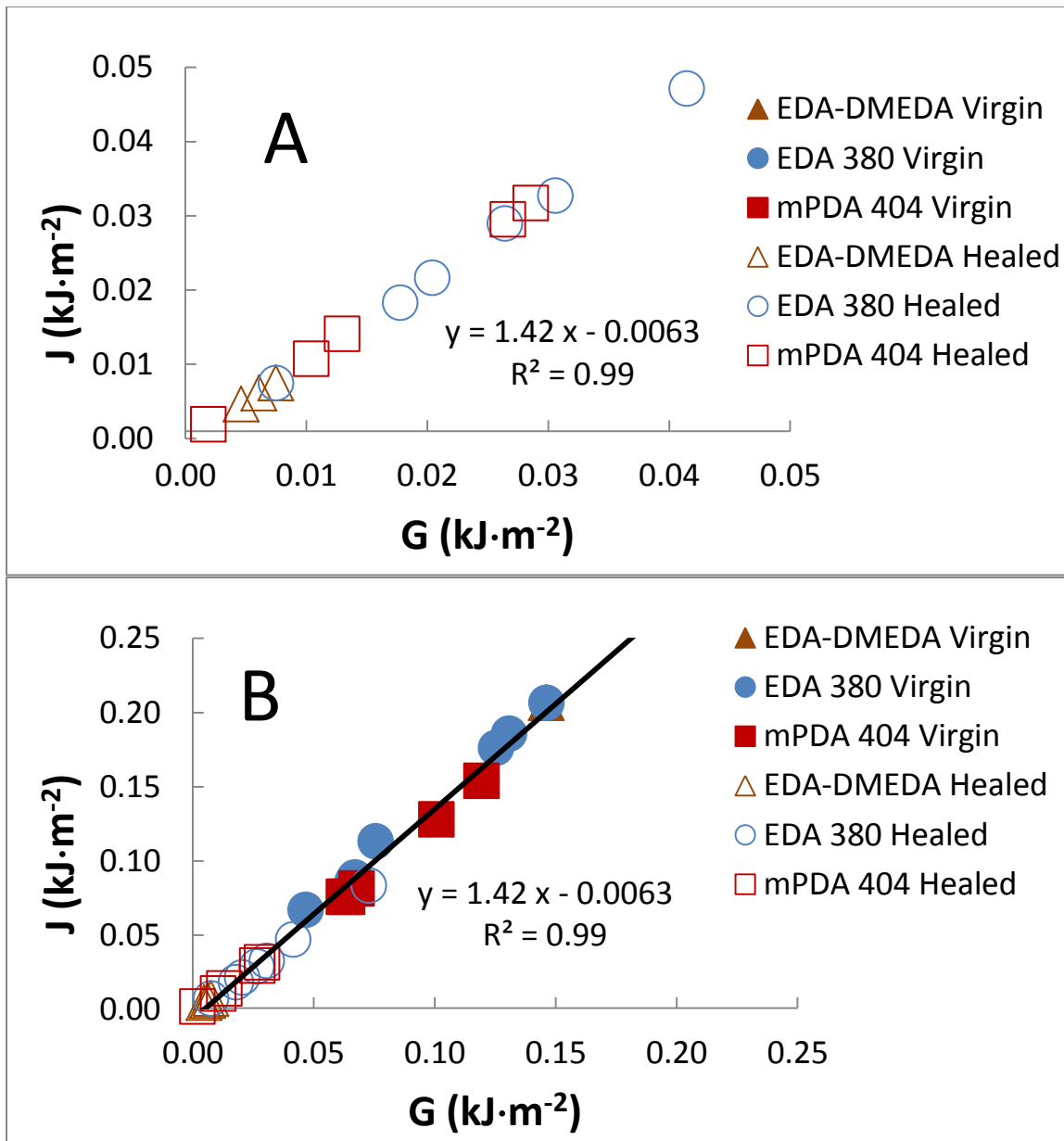
Where  $\mu$  is Poisson's ratio, which is assumed to be  $\sim 0.4$  for epoxies (31). For the Irwin correction used by Williams,  $\alpha = 1/2$ . Using a more accurate Dugdale-Barenblatt line zone model,  $\alpha = \pi/8$ , which amounts to a small variation from the Irwin correction. Equation 2-9 combines the expression for the network failure stress from Equation 2-6 into the effective crack length model.

$$\frac{J}{G} = \left[ 1 - \frac{D_0 E v^*}{\sigma_y^2} \right]^{-1} \quad [2-9]$$

Equation 2-9 can be rearranged to give G in terms of J and the molecular parameters of fracture.

$$G = J \left[ 1 - \frac{D_0 E v^*}{\sigma_y^2} \right] \quad [2-10]$$

The only unknown parameter in Equation 2-10 is the bond energy  $D_0$ . Figure 2-3A-D consists in plots of J vs G and the slope is equal to  $\left[ 1 - \frac{D_0 E v^*}{\sigma_y^2} \right]^{-1}$ .



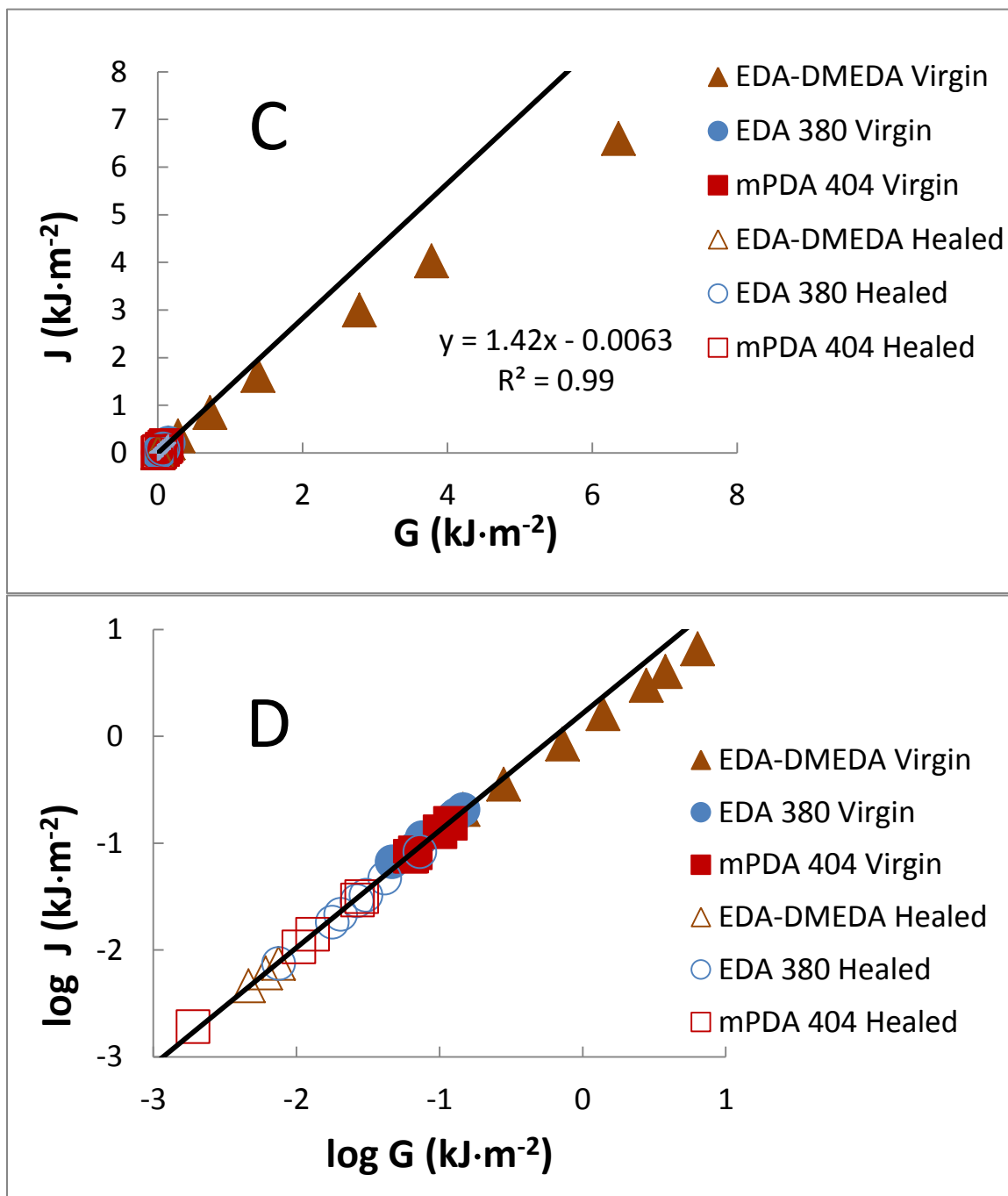


**Figure 2-3. Plots of the non-linear fracture energy (J) vs the linear component ( $J/(1+X)$ ). The linear fit is based on all networks where  $J < 0.25 \text{ kJ/m}^2$ . A) Low fracture energy networks comprising mainly healed networks B) Intermediate fracture energy networks including all EDA 380 and mPDA 404 networks (healed and partially cured virgin networks) C) All networks, including virgin EDA-DMEDA networks D) Log-Log plot of all networks.**

The same data are plotted on different scales in Figure 2-3A-C in order to show all data on a linear scale. The data scale almost four orders of magnitude, so plots with progressively larger scales collect the data from low fracture energy networks in the bottom left corner. Figure 2-3D captures all data in a single log-log plot. The EDA-DMEDA networks are fully cured chain extended networks. They show a departure from the fit of the other networks above  $J = 2 \text{ kJ/m}^2$ . The highest values from the EDA-DMEDA resins are taken from the data of Crawford and Lesser (12). These values were obtained using the single edge notch bend (SENB) fracture geometry to measure the non-linear fracture energy directly, whereas our data were obtained as fracture toughness from compact tension (CT) specimens.

The bond energy is calculated from the slope of the linear fits of Figure 2-3 A-C, which have a value of  $m = 1.42 = \left[1 - \frac{D_0 E v^*}{\sigma_y^2}\right]^{-1}$ . This slope gives average bond energies of  $D_0 \sim 1.0 \pm 0.1 \text{ kJ/mol}$  for the virgin aliphatic resins, and  $D_0 \sim 1.6 \pm 0.2 \text{ kJ/mol}$  for the virgin aromatic resins. The healed networks give values for  $D_0$  about 4 times the values of the virgin networks, and with larger scatter. These bond energy values are approximately two orders of magnitude lower than the typical value for a carbon-carbon bond  $D_0 \sim 350 \text{ kJ/mol}$  (30). This large deviation has been noted by others (29), and it has been attributed to the formation of radicals during the fracture process, which cause the rupture of additional bonds after a single mechanically induced scission event (32).

**Table 2-2. Fracture model parameters for virgin and healed networks.**

Resin	Virgin					Healed			
	T <sub>g</sub>	G	J	D <sub>0</sub>	r <sub>p</sub>	G	J	D <sub>0</sub>	r <sub>p</sub>
	°C	kJ/m <sup>2</sup>	kJ/m <sup>2</sup>	kJ/mol	μm	kJ/m <sup>2</sup>	kJ/m <sup>2</sup>	kJ/mol	μm
EDA 380	57	0.005	0.005	5.37	0.7	0.093	0.125	1.2	12.3
EDA 380	74	0.066	0.09	1.25	13	0.073	0.084	2.3	8.2
EDA 380	81	0.047	0.07	0.96	10	0.026	0.029	3.3	2.8
EDA 380	78	0.067	0.09	1.18	13	0.041	0.047	2.4	4.7
EDA 380	102	0.075	0.11	0.88	17	0.031	0.033	4.5	3.4
EDA 380	111	0.125	0.18	1.02	21	0.020	0.022	5.0	2.3
EDA 380	120	0.131	0.19	0.99	21	0.018	0.018	10	1.9
EDA 380	145	0.146	0.21	1.00	21	0.007	0.007		0.8
EDA-DMEDA 380	145	0.15	0.21	1.00	21	0.007	0.007		0.8
EDA-DMEDA 490	118	0.28	0.36	1.37	43				
EDA-DMEDA 670	95	0.73	0.85	2.05	124				
EDA-DMEDA 818	86	1.39	1.6	2.01	339	0.006	0.006		1.3
EDA-DMEDA 1040	71	2.79	3.0	4.14	445				
EDA-DMEDA 1452	67	3.78	4.0	4.76	989	0.005	0.005		1.1
EDA-DMEDA 2140	62	6.37	6.6	8.28	1289				
mPDA 404	103	0.07	0.08	1.74	8	0.029	0.032	2.9	2.5
mPDA 404	112	0.06	0.08	1.82	7	0.027	0.030	3.0	2.4
mPDA 404	118	0.06	0.08	1.65	7	0.013	0.014	3.6	1.1
mPDA 404	152	0.10	0.13	1.37	11	0.010	0.011	8.4	0.9
mPDA 404	182	0.12	0.15	1.30	12	0.002	0.002	16.5	0.2

Due to the short length of the chain fragments that are inevitably left on the fracture surfaces of fully cured epoxies, very little recovery of fracture toughness is expected from any healing procedure. There are a number of mechanisms that could potentially occur at intimately mated fracture surfaces during the healing process (24). Assuming intimate contact between the fracture surfaces, van der Waals forces would be expected to make a very small contribution to healing. However, the measured fracture toughness values are also at least an order of magnitude higher than the Griffith surface energy limit which gives  $K_{IC} \approx 0.013 \text{ Mpa}\cdot\text{m}^{1/2}$  (33). There could also be diffusion of the fractured chain fragments from one surface into the opposing surface. Due to the short chain lengths and the favorable interactions between the chemically similar surfaces it can be assumed that this process would occur on a timescale of seconds at temperatures above  $T_g$  (34,35). However, no meaningful entanglements are likely to occur, and this is demonstrated by the fact that all of the healed EDA-DMEDA resins recover approximately the same (very low) level of fracture toughness.

It has been argued that the maximum conversion possible in a densely cross-linked system is approximately 0.96 due to topological restrictions (36). However, techniques such as DSC and FTIR are not sensitive enough to be able to accurately measure residual functionality at conversions approaching the topological limit. There is likely a low level of unreacted functionality that is freed from its topological constraints due to the fracture event, but the probability of these unreacted moieties being situated close enough together and in the proper orientation to react across the crack interface is rather small. Despite the low probability for the development of significant strength through diffusion and epoxy-amine reactions in these fully cured networks, the samples

do heal in terms of a visual assessment. Weld lines are visible at the sample edges where deformation is expected to be greatest, but the crack interfaces do not scatter light after healing.

One plausible mechanism for the healing of fully cured epoxies is the formation of surface radicals during fracture (37). These radicals could recombine with other radical species from their side of the crack interface or react with oxygen and water in the air to form peroxides and oxiranes (38,39). This could explain the recovery of a minimum fracture toughness observed in the healed samples. The presence of other oxidative degradation products, such as the formation of amides, has also been observed in similar aliphatic cured epoxies, but there is an induction time of ~400 hours before FTIR analysis shows any significant signs of oxidative degradation in the spectra (40). Aliphatic epoxies are not expected to undergo significant radical reactions under thermo-oxidative conditions, as demonstrated by Burton (38), citing the ineffectiveness of commercial antioxidants in preventing amidation reactions. However, thermo-oxidative reactions do result in chain scission, which introduces a pathway for diffusion based healing. Aromatic systems, such as the mPDA based 404 resins, are expected to undergo radical reactions under healing conditions, but they exhibit behavior similar to the aliphatic resins upon healing so oxidative radical reactions are not considered to be important for healing here.

### **Designing a Healing System**

It would be useful to be able to apply the results presented in this paper to the design of self-healing systems that are engineered to take advantage of a number of the healing methods described in the Introduction. In any system that does not rely on

external stimuli to affect healing, diffusion of polymerizable moieties to the crack interface is required. Therefore, low viscosity healing agents can promote healing at the locations where they are needed. In order to promote faster reactions, particularly in epoxy-amine systems, amines can be activated by substituting N-methyl secondary amines for less reactive primary amines, which may also reduce hydrogen bonding and decrease viscosity. Assuming the healing reaction will not reach 100% conversion at ambient temperatures, increasing the functionality of the monomers can significantly lower the percolation threshold. As we observed in this work, a tetrafunctional amine reacting with a difunctional epoxide requires a conversion of at least 0.58 in order to percolate the network. By using a tetrafunctional epoxide with a tetrafunctional amine the critical conversion decreases to 0.33. Another parameter to consider is the molecular weight of the monomers involved in healing. A higher  $M_c$  translates to a higher fracture toughness, which can be seen by comparing the fracture toughness of the fully cured EDA-DMEDA series resins. However, fracture toughness is very low below the percolation threshold regardless of  $M_c$ . Therefore, higher molecular weight polyfunctional monomers can take advantage of the energy dissipation mechanisms that are accessible above the percolation threshold due to the relatively long backbones of healing monomers. However, monomers with longer backbones will typically have higher viscosity so optimization of the different molecular parameters would be necessary.

## **Conclusions**

A series of partially and fully cured aliphatic and aromatic amine cured epoxy networks with controlled conversions were prepared. The uniaxial compression and

fracture properties of the networks were used to evaluate the relationships between fracture and molecular parameters. To our knowledge, this effective crack length model is the first model able to fit the fracture behavior of partially cured networks, fully cured networks, and the corresponding healed networks based on their molecular parameters. Partially cured resins are significantly weaker in fracture than fully cured chain-extended resins with comparable cross-link densities due to the inability of the partially formed networks to transfer localized stresses to the rest of the network. This behavior is very similar to that observed in epoxy systems that contain significant levels of unreactive diluent. Applying the lessons from this work to the design of new self-healing materials, low viscosity thermosetting monomers with relatively high molecular weight between polyfunctional reactive end groups are predicted to be ideally suited to self-healing systems.

## **References**

1. Wu DY, Meure S, Solomon D. Self-healing polymeric materials: A review of recent developments. *Progress in Polymer Science*. 2008; 33: p. 470-522.
2. Wool RP. Self-healing materials: a review. *Soft Matter*. 2008; 4: p. 400-418.
3. Volynskii AL, Bakeev NF. Solvent Crazing of Polymers. *Polymer Science Series A*. 2009; 51: p. 1096-1126.
4. Urban MW. Stratification, stimuli-responsiveness, self-healing, and signaling in polymer networks. *Progress in Polymer Science*. 2009; 34: p. 679-687.
5. Murphy EB, Wudl F. The world of smart healable materials. *Progress in Polymer Science*. 2010; 35: p. 223-251.
6. Kim YH, Wool RP. A theory of healing at a polymer polymer interface. *Macromolecules*. 1983; 16: p. 1115-20.

7. Chen X, Dam MA, Ono K, Mal A, Shen H, Nutt SR, et al. A thermally remendable cross-linked polymeric material. *Science*. 2002; 295: p. 1802-1807.
8. Sivakova S, Bohnsack DA, Mackay ME, Suwanmala P, Rowan SJ. Interactions and phase segregation to yield highly thermosensitive supramolecular polymers. *Journal of the American Chemical Society*. 2005; 127: p. 18202-18211.
9. White SR, Sottos NR, Geubelle PH, Moore JS, Kessler MR, Sriram SR, et al. Autonomic healing of polymer composites. *Nature*. 2001; 409: p. 794-797.
10. Williams HR, Trask RS, Knights AC, Williams ER, Bond IP. Biomimetic reliability strategies for self-healing vascular networks in engineering materials. *Journal of the Royal Society of London Interface*. 2008; 5: p. 735-747.
11. Glad MD, Kramer EJ. Microdeformation and network structure in epoxies. *Journal of Materials Science*. 1991; 26: p. 2273-86.
12. Crawford ED, Lesser AJ. Brittle to ductile: Fracture toughness mapping on controlled epoxy networks. *Polymer Engineering and Science*. 1999; 39: p. 385-392.
13. Lemay JD, Kelley FN. Structure and ultimate properties of epoxy resins. *Advances in Polymer Science*. 1986; 78: p. 115-48.
14. Fischer M. Properties and failure of polymers with tailored distances between cross-links. *Advances in Polymer Science*. 1992; 100: p. 313-55.
15. Jordan C, Galy J, Pascualt JP. Measurement of the extent of reaction of an epoxy-cycloaliphatic amine system and influence of the extent of reaction on its dynamic and static mechanical properties. *Journal of Applied Polymer Science*. 1992; 46: p. 859-871.
16. Varley RJ, Hodgkin JH, Simon GP. Toughening of trifunctional epoxy system. V. Structure-property relationships of neat resin. *Journal of Applied Polymer Science*. 2000; 77: p. 237-248.
17. Marks MJ, Snelgrove RV. Effect of Conversion on the Structure-Property Relationships of Amine-Cured Epoxy Thermosets. *ACS Applied Materials & Interfaces*. 2009; 1: p. 921-926.
18. Lake GJ, Thomas AG. Strength of Highly Elastic Materials. *Proceedings of the Royal Society of London Series A-Mathematical and Physical Sciences*. 1967; 300: p. 108.

19. Crawford ED, Lesser AJ. The effect of network architecture on the thermal and mechanical behavior of epoxy resins. *Journal of Polymer Science: Part B: Polymer Physics*. 1998; 36: p. 1371-82.
20. Raghavan J, Wool RP. Interfaces in repair, recycling, joining and manufacturing of polymers and polymer composites. *Journal of Applied Polymer Science*. 1999; 71: p. 775-85.
21. Outwater JO, Gerry DJ. On the fracture energy, rehealing velocity and refracture energy of cast epoxy resin. *Journal of Adhesion*. 1969; 1: p. 290.
22. Detwiler AT, Lesser AJ. Aspects of network formation in glassy thermosets. *Journal of Applied Polymer Science*. 2010; 117: p. 1021-1034.
23. Chen X, Wudl F, Mal AK, Shen H, Nutt SR. New thermally remendable highly cross-linked polymeric materials. *Macromolecules*. 2003; 36: p. 1802-1807.
24. Wool RP, Yuan BL, McGarel OJ. Welding of polymer interfaces. *Polymer Engineering and Science*. 1989; 29: p. 1340-67.
25. Enns JB, Gillham JK. Effect of the extent of cure on the modulus, glass transition, water absorption, and density of an amine-cured epoxy. *Journal of Applied Polymer Science*. 1983; 28: p. 2831-2846.
26. Williams JG. *Fracture Mechanics of Polymers* New York, NY: Halsted Press: John Wiley & Sons Limited; 1984.
27. Miller DR, Macosko CW. Average Property Relations for Nonlinear Polymerization with Unequal Reactivity. *Macromolecules*. 1978; 11: p. 656-662.
28. Flory PJ. Molecular Size Distribution in Three Dimensional Polymers. I. Gelation. *Journal of the American Chemical Society*. 1941; 63: p. 3083-3090.
29. Wool RP. Rigidity percolation model of polymer fracture. *Journal of Polymer Science: Part B: Polymer Physics*. ; 43: p. 168-183.
30. Lide DR, editor. *CRC Handbook of Chemistry and Physics*. 90th ed. Boca Raton, Florida: CRC Press/ Taylor and Francis; 2010.
31. Verdu J, Tcharkhtchi A. Elastic properties of thermosets in glassy state. *Die Angewandte Makromolekulare Chemie*. 1996; 240: p. 31-38.
32. Kausch HH. *Polymer Fracture* Berlin Heidelberg: Springer-Verlag; 1978.

33. Griffith AA. The phenomena of rupture and flow in solids. *Philosophical Transactions of the Royal Society of London Series A*. 1921; 221: p. 163-198.
34. Beiner M, Ngai KL. Interrelation between primary and secondary relaxations in polymerizing systems based on epoxy resins. *Macromolecules*. 2005; 38: p. 7033-7042.
35. Montserrat S. Physical aging studies in epoxy resins. I. Kinetics of the enthalpy relaxation process in a fully cured epoxy resin. *Journal of Polymer Science: Part B: Polymer Physics*. 1994; 32: p. 509-522.
36. Oleinik EF. Epoxy-aromatic amine networks in the glassy state structure and properties. *Advances in Polymer Science*. 1986; 80(Part IV): p. 49-99.
37. Brown HR, Deline VR, Green PF. Evidence for cleavage of polymer chains by crack propagation. *Nature*. 1989; 341: p. 221-222.
38. Burton BL. The thermooxidative stability of cured epoxy resins. I. *Journal of Applied Polymer Science*. 1993; 47: p. 1821-1837.
39. Bellenger V, Verdu J. Oxidative skeleton breaking in epoxy–amine networks. *Journal of Applied Polymer Science*. 1985; 30: p. 363-374.
40. Delor-Jestin F, Drouin D, Cheval PY, Lacoste J. Thermal and photochemical ageing of epoxy resin - Influence of curing agents. *Polymer Degradation and Stability*. 2006; 91: p. 1247-1255.

## CHAPTER 3

# CHARACTERIZATION OF DOUBLE NETWORK EPOXIES WITH TUNABLE COMPOSITIONS

### **Abstract**

This article reports on the processing and characterization of epoxy resins with near constant molar cross-link density prepared from sequentially reacted amine cross-linking agents. Stoichiometric blends of curing agents with compositions ranging from all polyetheramine to all DDS are reacted with an epoxy monomer in a staged curing procedure. The low reactivity of the aromatic amine permits the selective reaction of the aliphatic amine in the first stage. The residual aromatic amine and epoxide functionality are reacted in a second stage at higher temperature. Above approximately 50% DDS content the first stage produces sol glasses which have not reached the gel point. The glass transition temperatures of the partially cured networks decrease monotonically with increasing DDS content. The partially cured networks can be characterized thermally and mechanically above their respective glass transitions without significantly advancing the reaction of the residual DDS and epoxide functionality. The networks formed after the second stage of the cure exhibit thermal and mechanical properties intermediate between those of the two individual amine cured networks, according to composition. The blends do not show any evidence of phase separation across the entire composition range in either the partially cured or fully cured state.

## **Introduction**

Amine cured epoxies are widely used as coatings, structural adhesives, and encapsulants for a variety of applications (1). By changing the nature of the epoxide and amine monomers it is possible to dramatically alter the physical and mechanical properties of the resulting networks. Although a variety of epoxide monomers are available, the diglycidylether of bisphenol A (DGEBA) and its oligomers are the most widely employed resins. On the other hand, there are comparatively far more curing agents available to react with the epoxides. The choice of curing agent is highly application driven since glass transition temperature ( $T_g$ ), solvent resistance, color, toughness, strength, and a number of other properties can be tailored by the choice of curing agent.

Aliphatic polyetheramine (PEA) curing agents are often employed when tough resins are needed and solvent resistance or high temperature properties are not critical. Diaminodiphenylsulfone (DDS) cured epoxies have excellent thermal stability and solvent resistance, but they tend to be brittle. They are often blended with high  $T_g$  thermoplastics to form phase separated composites with increased fracture toughness (2). There is relatively little published work on the physical and mechanical properties of blends of amine curing agents. Blends of PEAs have been studied in terms of the heterogeneity of the networks they form under various curing conditions (3,4,5). Aromatic diamines have been blended together to form low viscosity eutectics that facilitate mixing with epoxy resins at lower temperatures (6). Others have used blends of aromatic amines in order to control reaction kinetics and the incipient phase separation of thermoplastic additives (7). B-staged epoxy prepreg materials often contain blends of

amines and/or other latent curing agents where differences in reactivity are critical to shelf life and material handling characteristics (8,9). However, detailed analyses of relationships between physical properties, including non-linear mechanical properties, composition, and processing schemes in these systems are rare (5,10).

Part of the motivation for this work comes from recent studies in the literature where combinations of different monomers in hydrogels, advanced processing techniques in prestressed elastomers, and additives in IPNs have been exploited to create polymeric double network systems with improved properties. The double network hydrogels use combinations of rigid and flexible monomers to create hydrogels with increased fracture toughness. The order of network synthesis steps as well as the interconnectivity of the networks were observed to dramatically affect the properties of the final materials (11). Similarly, prestressed double network elastomers have been reported where a thermoplastic elastomer is stretched and cured by radical cross-linking while it is in the stretched state (12). This processing procedure generates networks with interesting stress-strain and thermal properties. However, little work has investigated double network glasses outside of phase separated systems. Single phase interpenetrating networks (IPNs) of polystyrene have been reported (13). One significant limitation of these systems is their reliance on specific chemistries with little flexibility in the synthesis and processing procedures. As noted above, epoxies offer significant flexibility in both of these aspects, thus allowing structure-property relationships to be explored across a wide range of network architectures and chemical functionalities.

In this work we investigate the basic physical and mechanical properties of double network epoxies formulated using stoichiometric blends of aromatic and aliphatic amine

curing agents. The curing agents are selected to have very similar molecular weight and to maintain miscibility of the mixtures at all conversions over the entire range of aromatic to aliphatic amine ratios. Effort is made in this paper to relate basic physical and mechanical properties to network architecture.

## Method

Stoichiometric mixtures of diglycidyl ether of bisphenol A (DGEBA)  $M_E=175$  g/mol, DER 332, supplied by Dow; 4,4'-diaminodiphenylsulfone (DDS) 97%, from Acros  $M_A=62$  g/mol; and  $\alpha,\omega$ -diaminopolypropyleneoxide (PEA), Jeffamine D230, courtesy of Huntsman  $M_A=60$  g/mol are prepared. The chemical structures of the monomers are given in Figure 2-1.

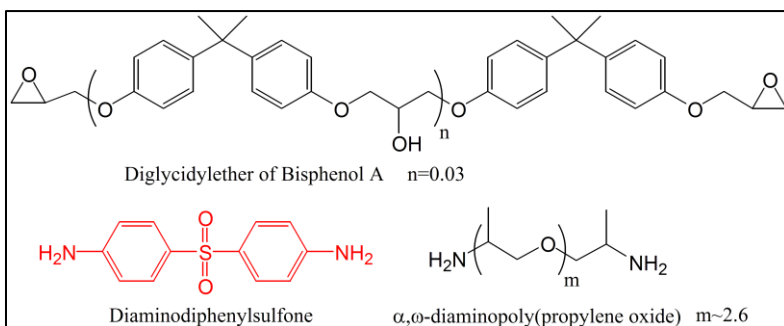


**Figure 3-1. Epoxy resin and amine cross-linkers.**

The DDS fraction of the curing agents ( $\phi$ ) is varied from 0 to 1 for different blends while maintaining stoichiometry between the amine and epoxide functionalities. The DDS component is stirred into DGEBA under vacuum at  $125^\circ\text{C}$  until it dissolves. The solution is cooled to  $80^\circ\text{C}$  before the PEA component is stirred in, and the mixtures are quickly poured into cylindrical glass molds (11.5 mm internal diameter) treated with a release agent (Sufasil, Pierce Chemicals). The molds are placed in a nitrogen purged oven at  $100^\circ\text{C}$  for 6 hours. Half of the molds containing each blend are cooled to room

temperature in a water bath, and half are postcured at 200°C for 6 hours before being cooled in a similar manner. Samples with  $\phi=0.8, 0.9,$  and 1.0 are postcured for 4 hours at 200°C and for 2 hours at 220°C. All samples are stored in their molds in a freezer at – 10°C until use.

The  $T_g$  of each resin is determined as the inflection point of the heat flow vs. temperature (dH/dT) curve from heating 5 mg samples at 10°C per minute in a DSC 2910 (TA Instruments). All samples from DSC are taken from bulk cast samples. Conversion is measured from the integration of the exotherm in the dH/dT curves. Density is measured at 21°C by the water displacement method (ASTM D792).

Samples for dynamic mechanical thermal analysis (DMTA) are machined to Length x Width x Thickness of 30 x 5 x 0.5 mm<sup>3</sup> for testing using single cantilever beam and tension geometries. Testing is conducted using a DMTA 2980 from TA Instruments at 1 Hz, 15  $\mu$ m displacement and a ramp rate of 3°C/min from -120-280°C. The storage modulus ( $E'$ ), loss modulus ( $E''$ ), and loss tangent ( $\tan \delta$ ) are recorded as a function of temperature. The full width at half maximum (FWHM) is calculated from  $\tan \delta$  in the  $\alpha$ -transition region, where the limits are taken as the minimum between  $T_\beta$  and  $T_g$  and the maximum associated with the  $\alpha$ -transition.

X-ray scattering is conducted on an evacuated Rigaku Molecular Metrology SAXS instrument using the  $\text{CuK}_\alpha$  spectral line with wavelength  $\lambda=0.1542$  nm, excited by 45kV and 0.67 mA. The slit collimated beam has a square cross-section of 0.3 x 0.3 mm. The detector for small angle X-ray scattering (SAXS) is a gas-filled 2D Multiwire detector, and the sample-to-detector length is  $L=1477$  mm as calibrated by the  $q=1.076$  nm<sup>-1</sup> peak from a silver behenate standard. Here,  $q=4\pi/\lambda\sin\theta$  and  $2\theta$  is the scattering

angle. Wide angle x-ray scattering (WAXS) is conducted on the same instrument, but a Fujifilm CR HR-V image plate at  $L=139$  mm is used to record the scattering.  $L$  is calibrated using the  $q=15.197$  nm<sup>-1</sup> 110 peak from a tricosane standard. The scattering intensities are transferred to a computer using a Fujifilm Bas-2500 image reader at 200  $\mu$ m resolution, 16 bit gradation, and a dynamic range of 30 000. Scattering patterns from SAXS and WAXS are circularly integrated to give scattering profiles with intensity in arbitrary units versus  $q$  in nm<sup>-1</sup>.

For compression testing, samples are removed from the molds and machined into compression bullets with a height to diameter ratio of 1:1. A drop of soapy water is placed on each face of the bullets and on the compression platens. PTFE film is placed on the top and bottom faces of the bullets. An Instron 5800 universal tester is used for compression testing at 20°C using a constant true strain rate of  $1.67 \times 10^{-3}$  s<sup>-1</sup>. Elevated temperature compression experiments are conducted on the same instrument in a nitrogen-purged oven that surrounds the compression platens. Samples are equilibrated at the testing temperature for 30 minutes prior to testing. High molecular weight silicone oil is used as the liquid lubricant at elevated temperatures.

## **Results and Discussion**

### **Partially Cured Networks**

In this work we use DDS as a latent curing agent such that the aliphatic amine and a corresponding fraction of the epoxide form a partially cured network after the initial cure stage at 100°C. In all cases the unreacted DDS and epoxide components act to reduce the  $T_g$  of an otherwise fully cured aliphatic amine cured network. The depression

of  $T_g$  with increasing DDS fraction in the partially cured networks is clear from the plots of the storage modulus ( $E'$ ) versus temperature in Figure 3-2.

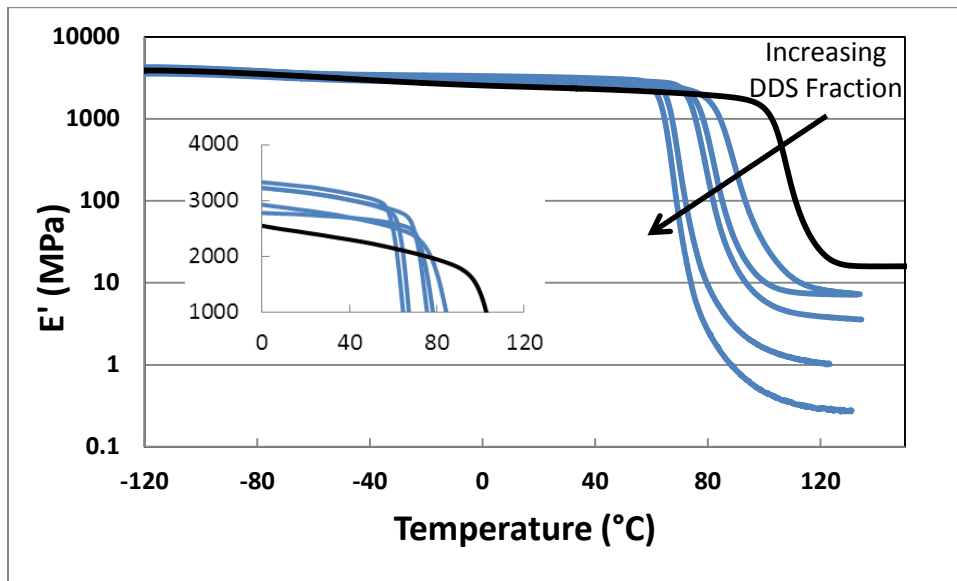


**Figure 3-2. Plot of storage modulus vs. temperature from DMTA temperature scans of partially cured networks. Arrow highlights the decrease in  $T_g$  and  $E'_R$  with increasing DDS content. Inset highlights increase in glassy storage modulus with increasing (unreacted) DDS fraction.**

Closer inspection of  $E'$  in the glassy state also shows that  $E'$  increases with DDS fraction. The presence of both decreased  $T_g$  and increased  $E'$  with increasing DDS fraction indicates that the unreacted epoxy and DDS components act as internal antiplasticizers for the aliphatic network (14,15). In Figure 3-3 the low segmental mobility below  $T_g$  is evidenced by the strong decrease in the strength of the  $\beta$ -transition with increasing DDS fraction. Since segmental mobility is depressed below  $T_g$  (antiplasticization), the glassy moduli of partially cured materials is higher than that of fully cured materials. The networks formed in the first stage of the curing scheme are effectively epoxide rich formulations with an additional unreactive diluent in the form of the unreacted DDS, which is in stoichiometric balance with the unreacted epoxide functionality. The presence of a single glass transition in DMTA temperature scans

(Figure 3-3) indicates the partially cured networks are miscible and contain a single phase. DMTA measurements were unable to be obtained in either tension or single cantilever beam geometries on samples where the DDS content was greater than 50% due to sample failure during clamping.

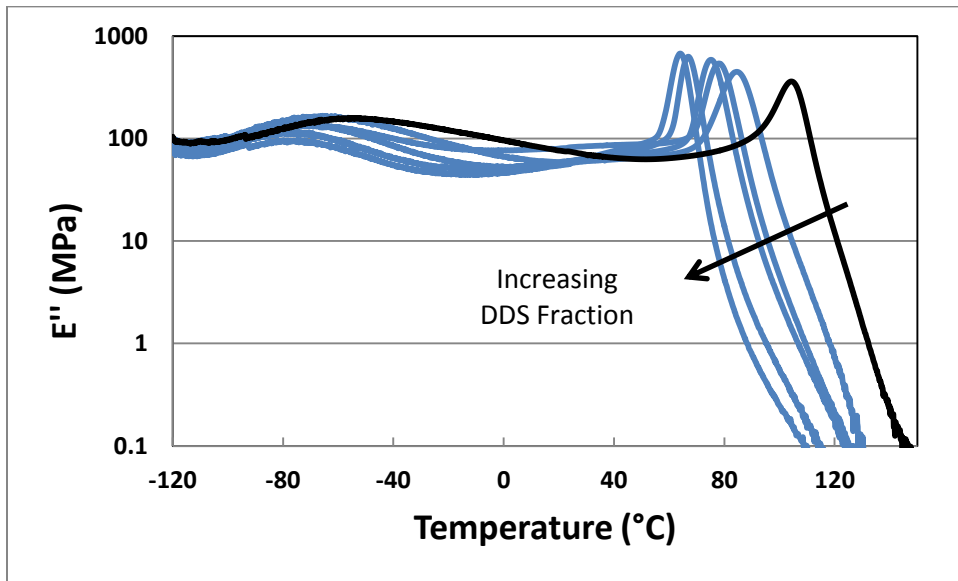


**Figure 3-3. Plot of loss modulus vs. temperature from DMTA temperature scans on partially cured networks. The arrow indicates the trend of decreasing  $T_a$  with increasing DDS content. There is also a clear decrease in the amplitude of the  $\beta$ -transition in the vicinity of  $-60^{\circ}\text{C}$ . Both trends are consistent with internal antiplasticization in a partially cured epoxy.**

Partially cured epoxy resins fabricated from low molecular weight epoxide and amine monomers are notoriously difficult to machine or test mechanically in the glassy state until the conversion is well beyond the critical conversion (15,16). For a difunctional epoxy and tetrafunctional amine the critical conversion is  $\sim 0.58$  (17). For compositions with greater than 50% DDS the conversion after the first cure stage falls below the gelation threshold, so the materials are extremely brittle sol glasses.

Figure 3-4 is a plot of true stress vs. Neo-Hookian strain from compression tests run on samples at  $120^{\circ}\text{C}$  after the first stage of the cure. Based on DSC and DMTA

results, 120°C is well above  $T_g$  for all networks after the first stage of curing so they should behave as rubbers, as opposed to glasses.

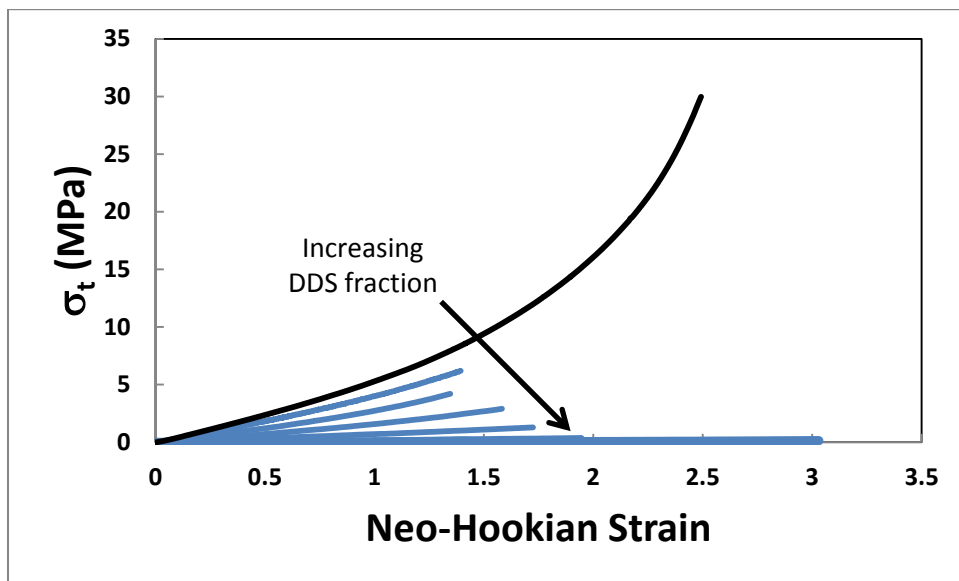


**Figure 3-4. Plot of true stress vs Neo-Hookian strain from uniaxial compression testing of partially cured networks. Testing was done at 120°C in order to measure the rubbery responses of the networks.**

The sample with only the aliphatic curing agent is fully cured, whereas the majority of the DDS, in networks that contain it, remains unreacted. Samples that contain greater than 50% DDS behave as viscous liquids because they do not yet have topologically percolating cross-linked networks. The low strain moduli scale inversely with DDS content, as expected for systems with increasingly diluted network chains. However, the networks with unreacted DDS ( $0 < \phi < 0.6$ ) tend to fail at relatively low strains. This failure behavior indicates the low connectivity of the partially cured networks imparts low cohesive strength, even in the rubbery state.

### **Fully Cured Networks**

The partially cured materials are postcured at 200°C (additional step at 220°C for samples with greater than 80% DDS). They show no change in  $T_g$  between the first and

second temperature sweeps in DSC, which indicates they are fully cured. The  $T_g$  values, measured from DSC, of the fully cured networks are compared those of the partially cured networks in Figure 3-5.

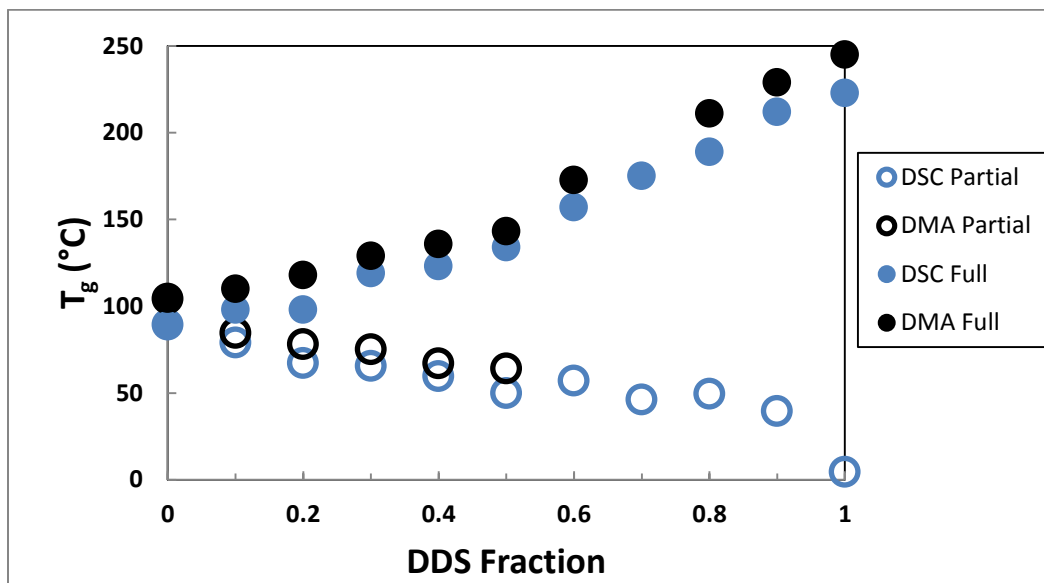


Figure 3-5. Plot of  $T_g$  of double networks as a function of DDS fraction. Data from DSC (Blue) and DMTA (Black) are from measurements made after the first (Open symbols) and second (closed symbols) cure stages.

Clearly,  $T_g$  increases with DDS fraction in the fully cured networks, and this trend is the same whether  $T_g$  is measured thermally or mechanically. Figure 3-6 and Figure 3-7 show how the storage and loss moduli curves change systematically with DDS fraction. Unlike the partially cured networks, the fully cured networks have nearly identical  $\alpha$ -transitions across the composition range as shown in Figure 3-7.  $T_g$  shifts to higher temperatures with increasing DDS, and the breadth of the transition increases. However, there is no splitting of the loss modulus into two  $\alpha$ -transition peaks. A single  $\alpha$ -transition indicates that the networks remain miscible across the entire composition range.

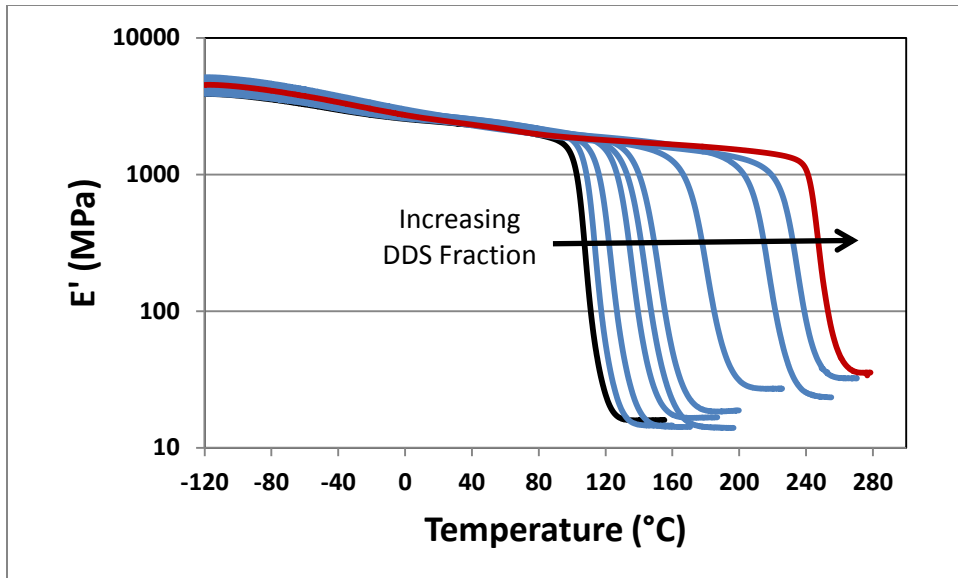


Figure 3-6. Plot of storage modulus vs Temperature scans from DMTA analysis. The arrow indicates the direction of increasing DDS content. The trend is for increasing  $\alpha$ -transition temperature and plateau modulus with increasing DDS content.

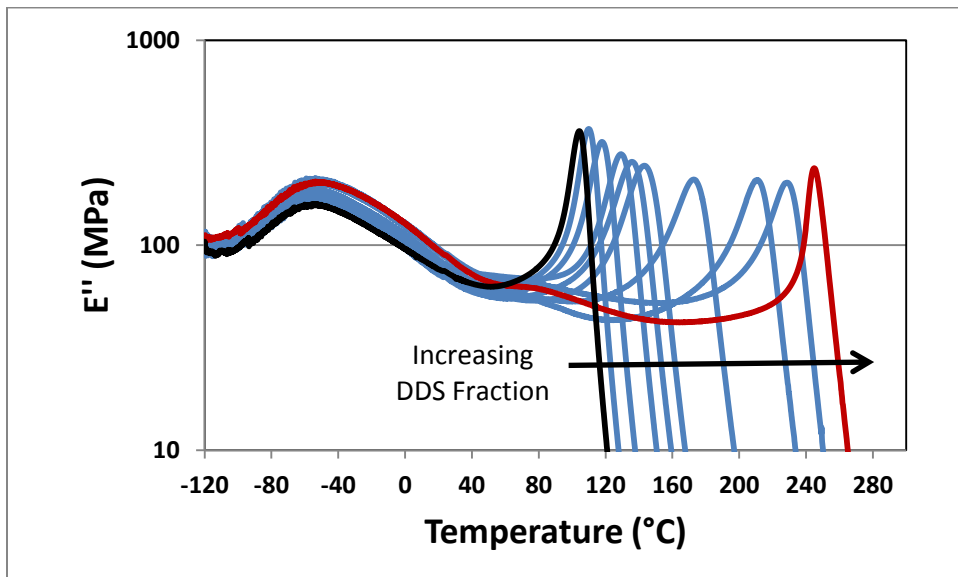


Figure 3-7. Plot of loss modulus vs Temperature scans from DMTA analysis. The arrow indicates the direction of increasing DDS content. The trend indicates that the  $\alpha$ -transition temperature increases and there is no change in the  $\beta$ -transition temperature with increasing DDS content.

The  $\alpha$ -transition appears to be narrowest for the pure aliphatic and pure aromatic compositions based on the normalized and shifted loss modulus curves presented in

Figure 3-8. As blends approach 50% of either component the  $\alpha$ -transition becomes much broader, particularly on the low temperature side of the transition.

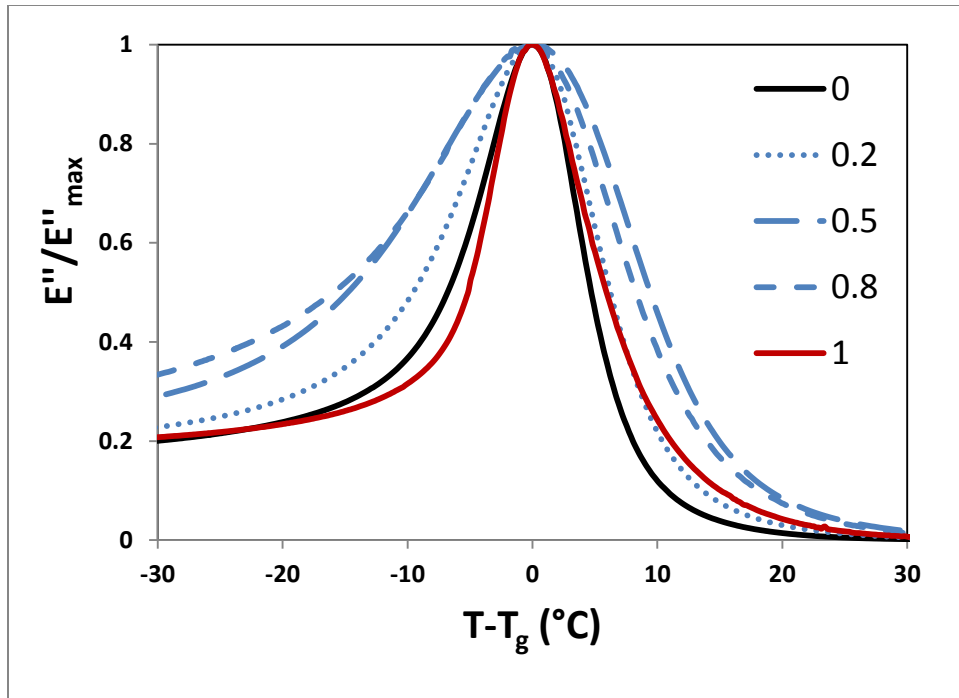
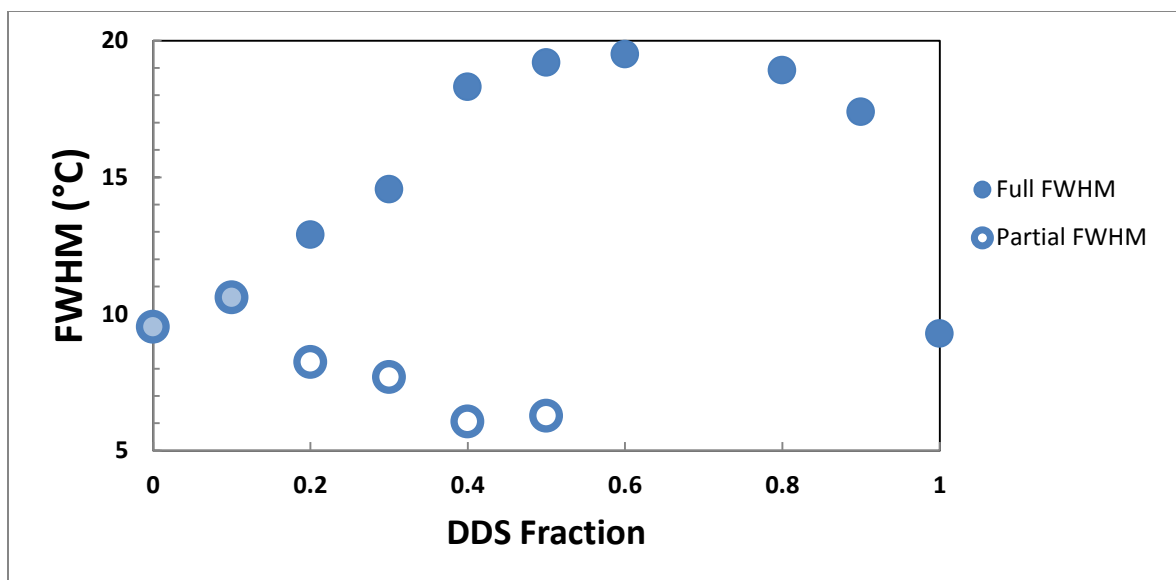


Figure 3-8. Normalized loss modulus vs shifted  $T_g$  plotted from DMTA temperature scans of selected network compositions. The temperature is shifted by the temperature at which the loss modulus exhibits a maximum during the  $\alpha$ -transition. The loss modulus is normalized by the maximum value of the loss modulus during the  $\alpha$ -transition.

This relationship has been observed in epoxies cured with blends of m-phenylenediamine and PEA (10). The broader  $\alpha$ -transition associated with the blends indicates that the pure networks are more homogeneous than the blended networks (18). Heterogeneity, as measured by the breadth of the  $\alpha$ -transition, arises due to the differences in local segmental mobility associated with the two different curing agents. The change in breadth of the  $\alpha$ -transition is quantified by measuring the full width at half maximum (FWHM) of the loss modulus peak in the  $\alpha$ -transition region. Data for FWHM are presented in Figure 3-9.



**Figure 3-9. Plot of full width at half-maximum vs. DDS fraction from the  $\alpha$ -transition region of DMTA temperature scans. Partially cured (hollow circles) and fully cured networks (filled circles). FWHM increases in proportion to the heterogeneity of segmental mobility on the timescale of the 1Hz oscillations.**

Heterogeneity in double network epoxies can result from different combinations of topological connectivity. An epoxide monomer may react with zero, one, or two DDS molecules. Therefore, counting only nearest neighbor connectivity, there are three types of epoxide segments in the networks. However, the  $\alpha$ -transition, occurring on the time scale of seconds (19), has been shown to arise from the cooperative motions of at least 10-20 atoms in the polymer chain (107,108). This cooperative region can contain a significantly larger number of combinations of aliphatic and aromatic components, so the distribution of aliphatic and aromatic cross-linkers can cause molecular scale dynamic heterogeneity. The two-stage cure schedule promotes this molecular scale heterogeneity. The aliphatic amine components all react in the first stage, and there is the potential to form large clusters of aliphatic amine rich regions. The DDS and DGEBA that remain unreacted must permeate these clusters because there is no evidence of more than one  $T_g$ . However, this topological heterogeneity can have important contributions to toughening a

single phase epoxy, as demonstrated by Wu et al. (5). The fracture behavior of these networks will be investigated in a second paper in this series (22).

### **X-Ray Scattering**

Although WAXS and SAXS are sensitive to local density fluctuations in a material, they are not able to provide information about compositional heterogeneity on the segmental level in most amorphous materials (5,23). Both WAXS and SAXS data indicate that the samples are amorphous due to the absence of sharp scattering peaks. In the WAXS scan presented in Figure 3-10 the broad peaks arising from the amorphous halo are the most prominent features (24).

The low  $q$  peak is shifted to lower  $q$  for the blended system, which indicates that the length scale of the electron density contrast increases slightly in networks of blended amines relative to networks composed of a single curing agent. These peaks arise at  $q = 6.8 \text{ nm}^{-1}$  and  $q = 8.3 \text{ nm}^{-1}$  or length scales of slightly less than 1 nm. This corresponds to the size scale of the monomer units, which should exhibit a characteristic length scale and electron density contrast due to compositional differences (25).

The SAXS data presented in Figure 3-11 also indicate that the networks are amorphous, with no long range order. The only feature resolvable from the scattering profile is the increase in scattering at low  $q$ , which is attributed to the approach to the beam stop. Therefore, the X-Ray scattering data are consistent with the conclusion that these double network epoxies are single phase miscible systems across the composition range.

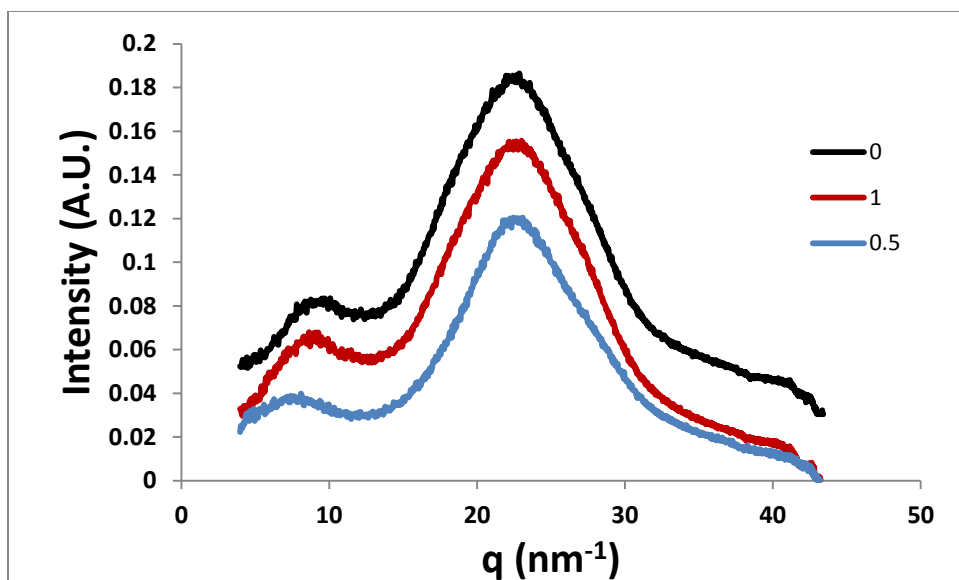


Figure 3-10. Plot of wide angle x-ray scattering profile vs. scattering vector from fully cured networks. DDS fractions of 0 (black), 1 (red) and 0.5 (blue). The broad amorphous halo depicted with no sharp scattering peaks indicates that the networks are amorphous.

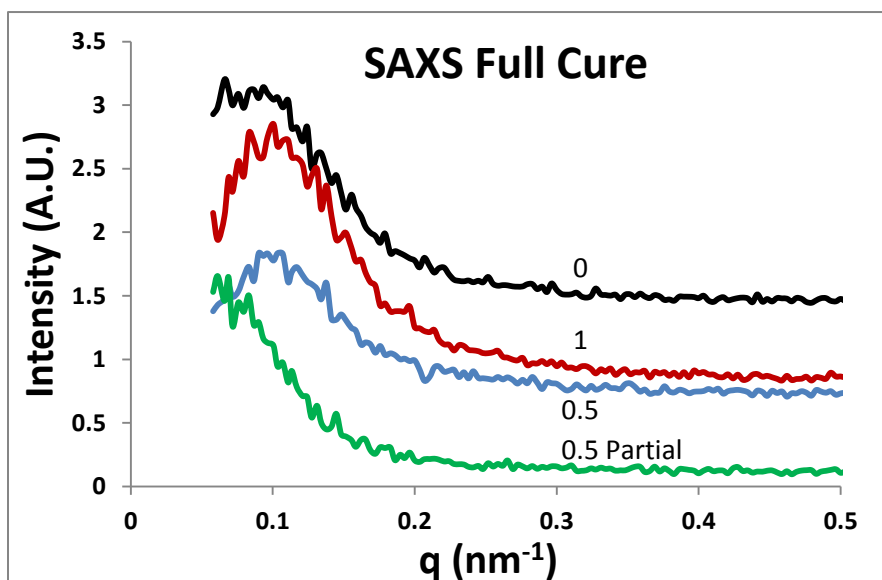


Figure 3-11. Plot of small angle x-ray scattering profile vs. scattering vector from fully cured networks. DDS fractions of 0 (black), 1 (red), 0.5 (blue), and a partially cured network with 0.5 DDS (green). The increase in scattered intensity in all profiles is attributed to the approach to the beam stop. No peaks arising from large scale structures are resolved in this  $q$  range, as expected from an amorphous single phase material.

## COMPRESSION TESTING

Affine deformation in compression probes both the pre-yield and post-yield responses of materials. In contrast to uniaxial extension, uniaxial compression does not create a neck or promote fracture that otherwise complicates the analysis of the true stress-true strain responses of polymers (26). Below  $T_g$ , the low strain response of polymers is sensitive to their thermomechanical history and local segmental dynamics (27,28). The high strain response, beyond the yield strain, is sensitive to cross-link density in thermosets (29) and entanglement density in thermoplastics (30). There is some debate in the literature in terms of how to characterize the high strain response of thermoplastics and thermosets. Although the strain hardening response has been shown by numerous authors to correlate with entanglement density or cross-link density (31,32), the mechanical response does not scale with temperature or strain rate as one might predict from rubber elasticity arguments (30,33). The discrepancy arises from the intermolecular interactions present during inelastic deformation, and the viscous dissipation of strain energy is, predictably, rate and temperature dependent (30,33). Haward and Thackeray proposed that glassy polymers undergoing post-yield deformation should behave like cross-linked elastomers where entangled chains in the glass are analogous to cross-linked chains in a rubber (34). Strain hardening is, thus, thought to result from the loss of entropy as entangled chains align (32). This non-linear behavior can be captured by using a neo-Hookian measure of strain (32,35). Here, the strain hardening modulus ( $G_R$ ) is the slope of the true stress ( $\sigma_T$ ) versus neo-Hookian strain curve as given by Equation 3-1.

$$G_R = - \frac{\partial \sigma_t}{\partial (\lambda^2 - 1/\lambda)} \quad [3-1]$$

Where  $\lambda$  is the extension ratio.  $M_c$  is calculated from the strain hardening response using Equation 3-2, or from stoichiometric considerations using Equation 3-3,

$$M_c = \frac{\varphi \rho RT}{G_R} \quad [3-2]$$

$$M_c = 2(M_E + M_A) \quad [3-3]$$

Where  $\rho$  is the mass density,  $R$  is the ideal gas constant,  $T$  is the absolute temperature, and  $\varphi$  is a constant related to cross-link mobility and is assumed to be equal to 1 for immobile cross-links (36).  $M_E$  is the epoxide equivalent weight and  $M_A$  is the amine equivalent weight.

Equations 3-1 and 3-2 provide a way to interpret the strain-hardening responses of networks in terms of network architecture (34,37). The strain hardening modulus is the value of the slope of the true stress-NeoHookean strain curve (Equation 3-1) measured at 90% of the ultimate true strain. Using the slope at 90% of the ultimate true strain ( $\epsilon_b$ ) allows one to sample  $G_R$  at a standardized location deep in the non-linear deformation region, where the connectivity of cross-links should have the greatest relative influence over the change in true stress with increasing strain. Equation 3-2 uses the strain hardening response to calculate the molecular weight between cross-links.

Although the strain hardening responses of a number of glassy polymers correlate with entanglement or cross-link density, as calculated from the plateau modulus (37), the theory fails to account for the temperature and strain rate dependence of strain hardening, as well as the ~2 order of magnitude quantitative discrepancy in the calculated entanglement density (16,30,38,39). On these grounds, strain hardening is thought to originate from a combination of local segmental interactions, and the larger scale entanglement network, which both depend on temperature and the number of segments

between entanglements (38). Changes in chain conformation during large deformations cause the relative contributions of inter-segmental interactions and network connectivity to change. It has proven to be challenging to identify individual contributions experimentally (38,40).

Most work on the large strain mechanics of glassy polymers has focused on thermoplastics, such as PC, PS, PPO, PMMA, and PETG (41). A few authors have looked at cross-linked systems such as cross-linked PS (30), cross-linked PMMA (40), and epoxies (16,29,42). Particularly in epoxy systems, the molecular weight between cross-links (hundreds of g/mol) is on the order of a tenth of the entanglement molecular weight of thermoplastics (thousands of g/mol). Therefore, the cross-links in epoxy resins are expected to affect local segmental mobility at a much smaller scale than the entanglements of thermoplastics. This reduction in segmental mobility is the main reason  $T_g$  increases with cross-link density (43).

Uniaxial compression tests on fully cured samples in Figure 3-12 demonstrate that the networks exhibit qualitatively similar true stress-Neo-Hookean strain responses across the entire composition range, but the curves are shifted to higher stresses with increasing DDS content in the non-linear deformation region. The elastic modulus, measured at small strains, decreases with DDS fraction as demonstrated in Figure 3-13. This inverse relationship between  $T_g$  and elastic modulus has been observed in other fully cured epoxy systems (44) where the glassy modulus is inversely proportional to the intensity of the low temperature  $\beta$ -relaxation. The trends of loss modulus with DDS fraction in Figure 3-7 are consistent with this explanation.

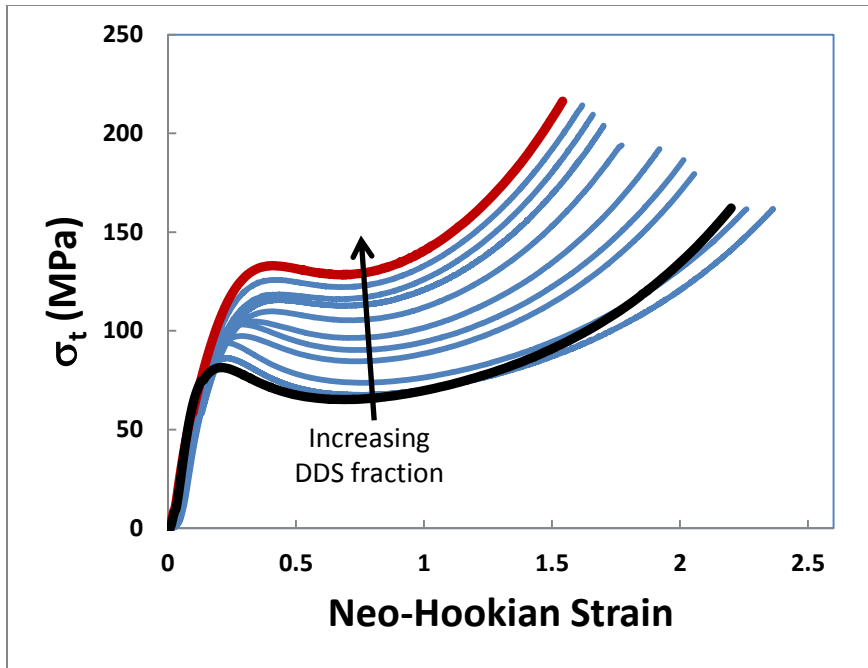


Figure 3-12. Plot of true stress vs Neo-Hookian strain from uniaxial compression tests on fully cured networks conducted at 20°C. Increasing DDS content shifts the curves to higher stresses and decreases the strain at which the networks fail, but the qualitative shape of the curves is unchanged.

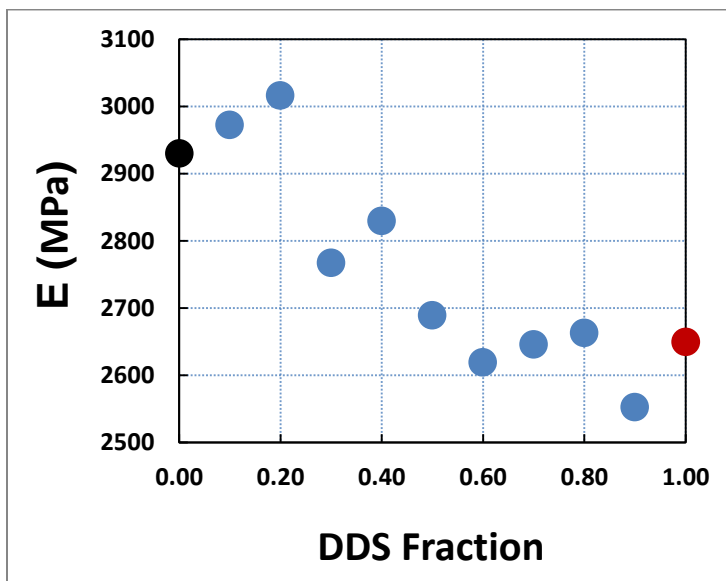
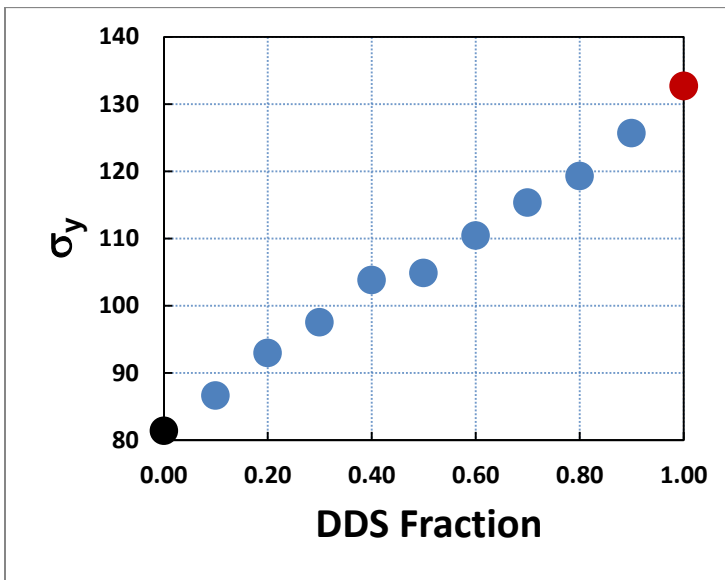


Figure 3-13. Plot of compressive modulus vs DDS fraction measured at 20°C. Modulus decreases with increasing DDS content.

Figure 3-14 indicates that yield stress increases with DDS content. Yield is a stress induced thermally activated transition from low segmental mobility to high segmental mobility (45). It is sensitive to localized segmental interactions such as Van

der Waals forces and hydrogen bonding that restrict segmental mobility. These non-covalent interactions are functions of density, thermomechanical history, chemical composition, and test temperature (27,46,47,48). Since the chemical compositions of the networks vary it is difficult to quantitatively describe the thermomechanical histories of the samples except to say that they have all experienced a similar aging time (several days) and temperature (-10°C). Under these conditions, physical aging is expected to be a relatively slow process, occurring over thousands of hours (49,50).



**Figure 3-14. Plot of yield stress vs DDS fraction. Yield stress increases in proportion to DDS fraction.**

Since both density in Figure 3-15 and  $T_g$  in Figure 3-5 increase with increasing DDS fraction, one would correctly predict that yield stress increases with DDS content as well. These double network epoxy systems allow for precise control over physical and mechanical properties, such as  $T_g$ , yield stress, and density by simply changing the DDS fraction in the networks.

It has been argued in the thermoplastic (34,35) and thermoset literature (16,29) that the strain hardening modulus, measured in the glassy state, scales with entanglement

density and cross-link density, respectively. The DDS and aliphatic curing agents used in this study were selected, in part, because they have nearly identical molecular weight.

Therefore, changes in the composition should not affect the molar cross-link density.

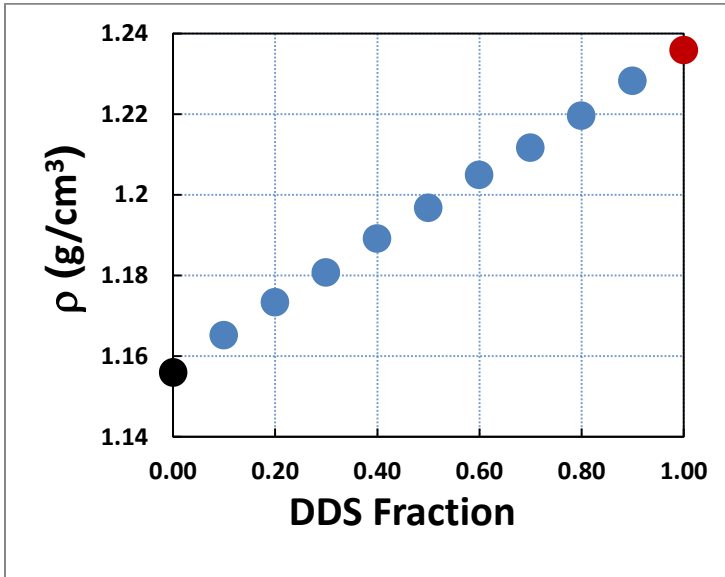


Figure 3-15. Plot of density vs DDS fraction measured by the water displacement method at 21°C. Density increases linearly with DDS fraction.

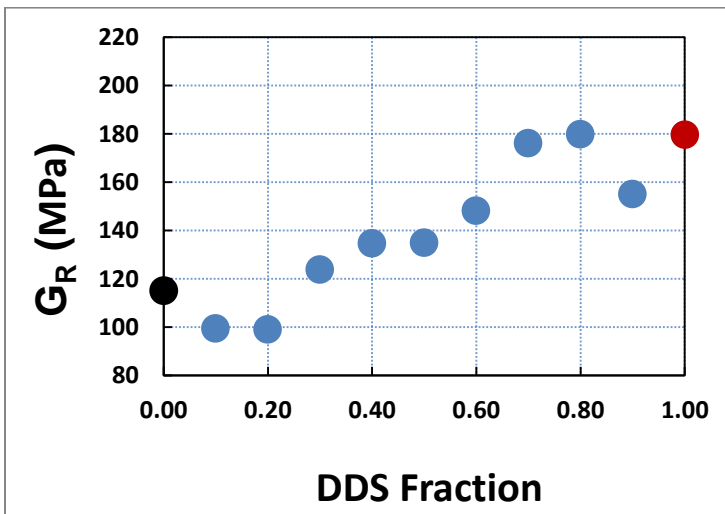


Figure 3-16. Plot of strain hardening modulus vs DDS fraction. The strain hardening modulus at 90% of the ultimate strain increases with DDS content. This trend indicates the DDS fraction increases the stiffness of networks relative to the aliphatic fraction.

However, the strain hardening responses of the double network epoxies in Figure 3-16 do show dependence on DDS content. Since the mass density increases with DDS content,

the cross-link density, in terms of cross-links per unit volume, does increase with DDS content.

The cross-link density, as calculated from  $G_R$ , is plotted in Figure 3-17 against the cross-link density calculated from stoichiometric considerations. The slope of the line between the all aliphatic and all aromatic networks has a slope of approximately 180. Clearly, the cross-link density calculated from the strain hardening modulus increases with DDS content faster than it does based on stoichiometric considerations. This behavior reaffirms the notion that the strain hardening response depends on both cross-link density and the chemical nature of the cross-links and the chain segments between them in the glassy state.

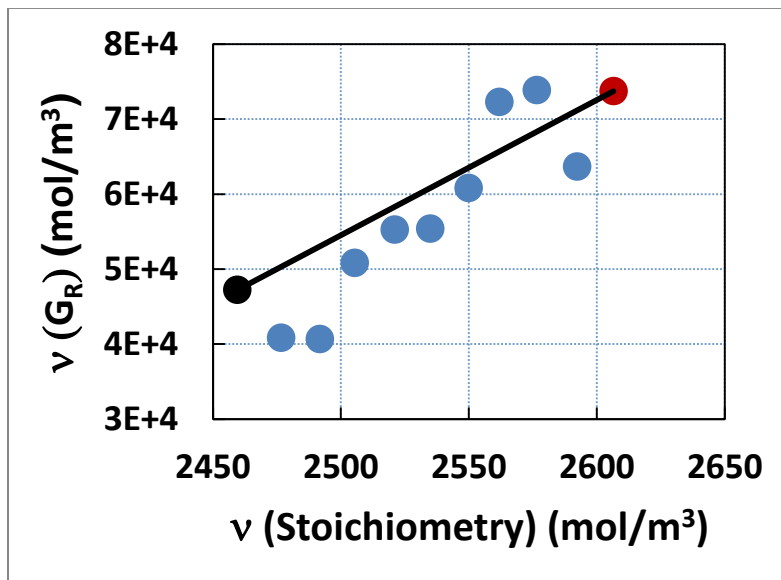
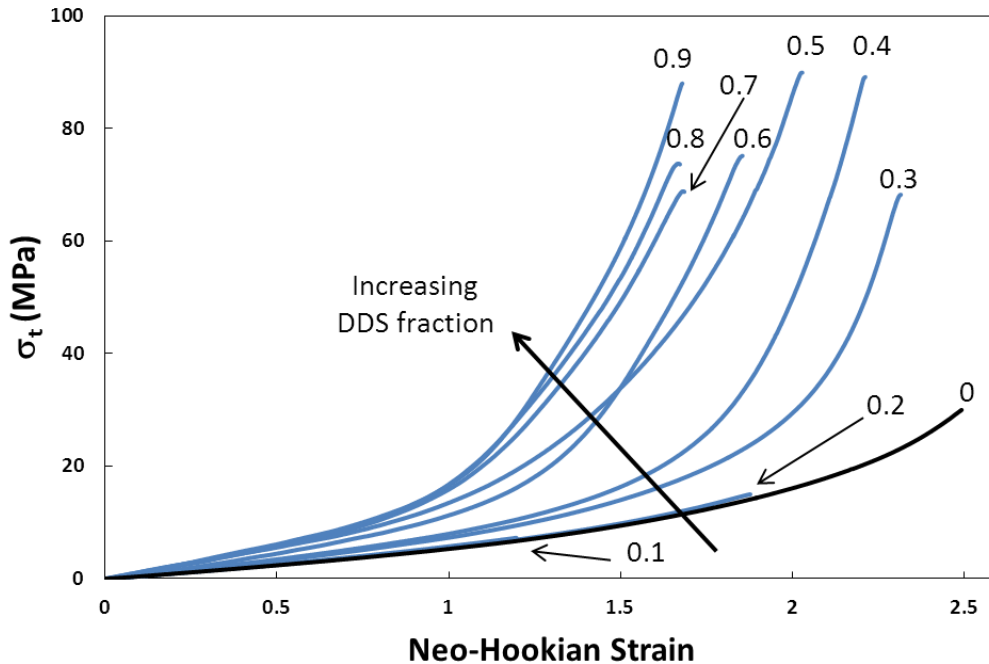


Figure 3-17. Plot of cross-link density calculated from the strain hardening modulus vs cross-link density calculated from the stoichiometric balance of monomers. Both measures of cross-link density are functions of the mass density of the networks, which increases with DDS fraction. The black line has a slope of  $\sim 180$ , which indicates that  $v(G_R)$  increases much faster than would be expected from stoichiometric considerations.

The true stress versus Neo-Hookean strain curves of fully cured networks tested  $20^\circ\text{C}$  above  $T_g$  are plotted in Figure 3-18. In the low strain region the true stress is a linear function of strain. However, the data in Figure 3-19 show that the shear modulus

(G), from the linear portion of the curves, increases with DDS content. A linear relationship between the true stress and Neo-Hookian strain is predicted for a Gaussian network (32). The strong strain hardening above  $-(\lambda^2 - 1/\lambda) = 1$  indicates a departure from linear behavior. This trend confirms that the composition affects the mechanical behavior, even at elevated temperature, where large thermally induced segmental fluctuations diminish the effects of intersegmental interactions. If the rubbery modulus, obtained from elevated temperature compression tests ( $E_R$ ) is substituted for  $G_R$  in Equation 3-2, the resulting  $M_c$  values can be calculated.



**Figure 3-18.** Plot of true stress vs. Neo-Hookian strain from compression tests conducted at  $T_g+20^\circ\text{C}$  for double networks. The arrow indicates the trend of increasing stiffness at large strains with increasing DDS fraction.

Figure 3-20 compares the  $M_c$  values obtained from the strain hardening modulus, obtained in both the glassy and rubbery state; the low strain shear modulus from the rubbery state, and the value calculated from stoichiometric considerations according to Equation 3-3 (labeled Stoichiometry in Figure 3-20).

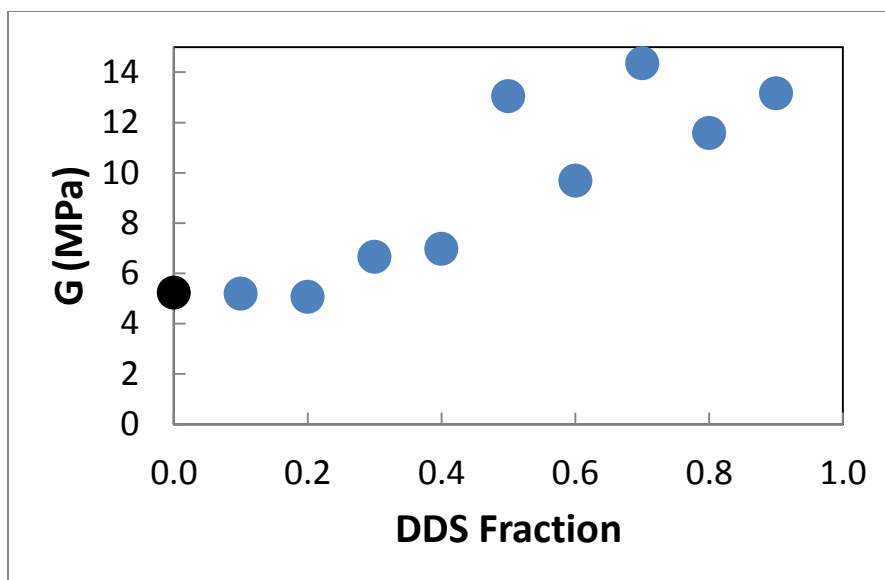


Figure 3-19. Plot of compressive modulus vs DDS fraction measured in the low strain region of compression tests conducted at  $T_g+20^\circ\text{C}$ . The increase in the low strain rubbery modulus with DDS fraction indicates that the DDS component of the networks increases the apparent cross-link density relative to the polyetheramine component.

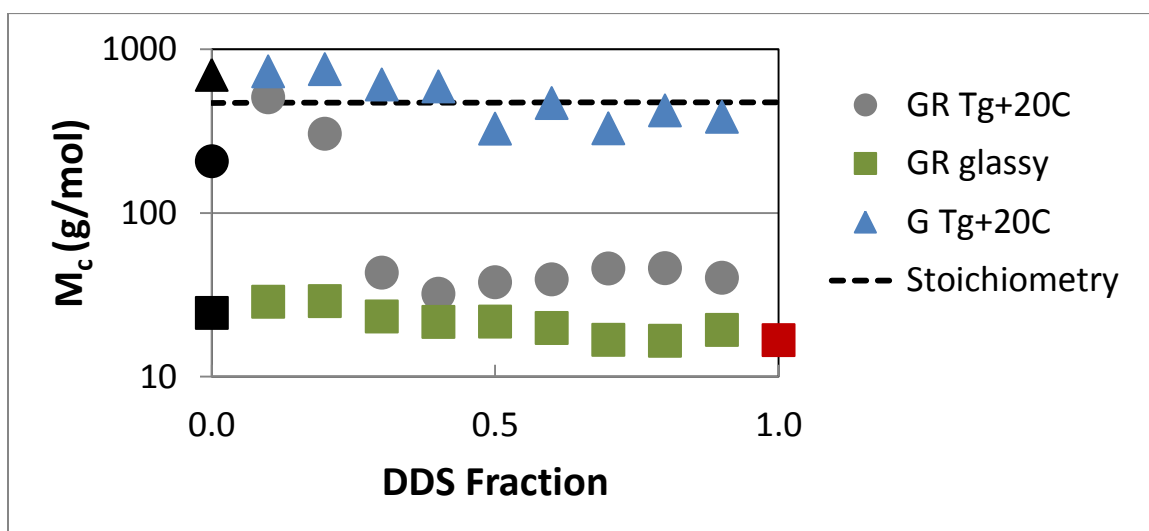


Figure 3-20. Plot of molecular weight between cross-links vs DDS fraction.  $M_c$  is calculated using four different data sets: strain hardening modulus of compression curves acquired at  $T_g+20^\circ\text{C}$  (blue circles), strain hardening modulus of compression curves tested at  $20^\circ\text{C}$  (green squares), low strain modulus of compression curves acquired at  $T_g+20^\circ\text{C}$  (blue triangles), stoichiometric calculations based on tetrafunctional cross-links (dashed line).

The  $M_c$  values calculated from the low strain modulus measurements obtained above  $T_g$  are in relatively good quantitative agreement with the stoichiometrically calculated values. Although the mechanical measures of  $M_c$  all have qualitatively similar

trends with respect to changing DDS content, measuring the mechanical response of networks with varying compositions in the glassy state clearly introduces large quantitative discrepancies.

The effects of cross-linker structure on rubber elasticity have been studied by numerous authors over many years (48,53,54). Differences in mechanical response as a function of composition in the current networks likely arise from differences in cross-link mobility, which is related to the chemical structures of the cross-linker units. The DDS amine groups are attached to rigid and bulky phenylene groups which reduce cross-link mobility relative to the secondary carbon, and relatively flexible poly(propylene oxide) chains of the aliphatic amines (36). Reduced cross-link mobility increases the stiffness of a material for a given cross-link density (28,29,42), which is in agreement with the observed compression response of the double network epoxies above  $T_g$ .

Although DDS and the aliphatic diamine have similar molecular weights, they have approximately 4 and 11 rotatable bonds along their backbones, respectively, as counted by Bicerano (53). Several authors have argued that the number of rotatable bonds between cross-links, as opposed to  $M_c$  or  $\nu$ , is ultimately responsible for correlations between  $M_c$ ,  $T_g$ , and mechanical properties (36,54). The decrease in the number of rotatable bonds with increasing DDS content in the double networks explains the increase in rubbery modulus with DDS content. Also, the greater extensibility of the aliphatic amine-rich networks, as measured by the strain at break from compression tests (Figure 3-21), correlates well with the presence of more rotatable bonds in those networks. The upturn in the true stress vs Neo-Hookean strain curves occurs at higher strains as the DDS fraction decreases. This dramatic increase in the modulus at large strains is observed in

other elastomeric systems at high extensions where it is attributed to the finite extensibility of chain segments.

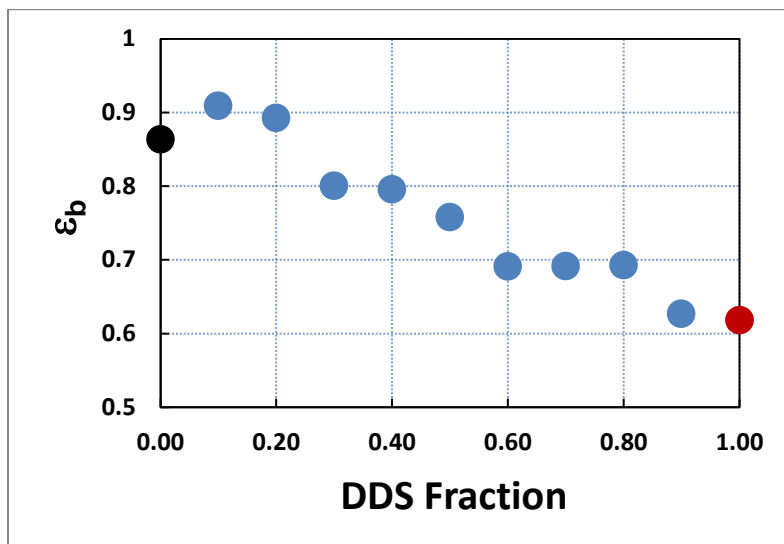


**Figure 3-21.** Plot of true strain at break vs DDS fraction from compression testing. The decrease in strain at break with increasing DDS fraction indicates that the DDS fraction reduces the extensibility of the networks. This is evidence of the rigid nature of the diphenylsulfone segments relative to the polyether segments in the aliphatic amine.

Since the DDS segments have fewer rotatable bonds than the ether-amine segments, the shift from linear stress-strain behavior to strain hardening is expected to take place at lower strains for networks with higher DDS fractions.

## **Conclusions**

Double network epoxies cured in a two-stage process with varying ratios of aromatic and aliphatic amines form model network systems with tunable physical and mechanical properties. The networks formed by the reaction of the aliphatic amine component at 100°C show strong evidence of internal antiplaticization below  $T_g$ . Above  $T_g$ , the partially cured networks behave as elastomers with rubbery moduli that depend on network connectivity. The fully cured networks are characterized by compositionally dependent modulus, yield, post-yield, and thermal properties. The difference in molecular

architecture between the two curing agents leads to a broadening of the  $\alpha$ -transition in the blended networks. This heterogeneity plateaus when the DDS forms the majority of the amine component. The yield and rejuvenated stresses increase linearly with DDS content, which indicates the sensitivity of these two parameters to intersegmental interactions in the glassy state. The strain hardening moduli in both the glassy and rubbery states increase with DDS content. However, the mechanical properties of the networks are strongly affected by intersegmental interactions in the glassy state. The connectivity of the networks, as measured mechanically, is most accurately calculated from the linear portion of true stress vs Neo-Hookean strain curves measured above  $T_g$ . A second paper in this series will evaluate the fracture behavior of double network glasses as a function of composition (22).

## **References**

1. Ellis B. Chemistry and Technology of Epoxy Resins New York: Chapman and Hall; 1993.
2. Bucknall CB, Partridge IK. Phase-separation in epoxy resins containing polyethersulfone. *Polymer*. 1983; 24(5): p. 639-644.
3. Wu WL, Bauer BJ. Network Structure in Epoxies. 6. The Growth Process Investigated By Neutron Scattering. *Polymer*. 1989; 30: p. 1384-1388.
4. Beck Tan NC, Bauer BJ, Plestil J, Barnes JD, Liu D, Matejka L, et al. Network structure of bimodal epoxies--a small angle X-ray scattering study. *Polymer*. 1999; 40: p. 4603-14.
5. Wu WL, Hu JT, Hunston DL. Structural heterogeneity in epoxies. *Polymer Engineering and Science*. 1990; 30(14): p. 835-840.
6. Philipson J, inventor; Method and composition for curing epoxy resins. patent 2891927. 1959.

7. Lahlali N, Naffakh M, Dumon M. Cure kinetics and modeling of an epoxy resin cross-linked in the presence of two different diamine hardeners. *Polymer Engineering and Science*. 2005; 45: p. 1581-89.
8. Wiggins PL, inventor; Epoxy curing agent composition. USA patent 4,775,736. 1988 October 4.
9. Tesch H, Heym M, Doerflinger W, Stutz H, Neumann P, Nissen D, et al., inventors; Curable compositions based on epoxy resins. USA patent RE32,628. 1988 March 22.
10. de Nograro FF, Llano-Ponte R, Mondragon I. Dynamic and mechanical properties of epoxy networks obtained with PPO based amines/MPDA mixed curing agents. *Polymer*. 1996; 37(9): p. 1589-1600.
11. Nakajima T, Furukawa H, Tanaka Y, Kurokawa T, Osada Y, Gong JP. True chemical structure of double network hydrogels. *Macromolecules*. 2009; 42: p. 2184-2189.
12. Singh NK, Lesser AJ. Mechanical and Thermo-Mechanical Studies of Double Networks Based on Thermoplastic Elastomers. *Macromolecules*. 2010; 44: p. 1480-1490.
13. Thiele JL, Cohen RE. Synthesis, characterization, and viscoelastic behavior of single-phase interpenetrating polystyrene networks. *Polymer Engineering and Science*. 1979; 19(4): p. 284-293.
14. Bellenger V, Dhaoui W, Verdu J. Internal Antiplasticization in Diglycidyl Ether of Bisphenol A Diamino Diphenyl Methane Non-Stoichiometric Epoxy Networks. *Polymer Engineering and Science*. 1990; 30(6): p. 321-325.
15. Jordan C, Galy J, Pascual JP. Measurement of the extent of reaction of an epoxy-cycloaliphatic amine system and influence of the extent of reaction on its dynamic and static mechanical properties. *Journal of Applied Polymer Science*. 1992; 46: p. 859-871.
16. Detwiler AT, Lesser AJ. Aspects of network formation in glassy thermosets. *Journal of Applied Polymer Science*. 2010; 117: p. 1021-1034.
17. Flory PJ. Molecular Size Distribution in Three Dimensional Polymers. I. Gelation. *Journal of the American Chemical Society*. 1941; 63: p. 3083-3090.
18. Cook WD, Scott TF, Quay-Thevenon S, Forsythe JS. Dynamic mechanical thermal analysis of thermally stable and thermally reactive network polymers. *Journal of Applied Polymer Science*. 2004; 93: p. 1349-1359.

19. Adam G, Gibbs JH. On the temperature dependence of cooperative relaxation properties in glass-forming liquids. *Journal of Chemical Physics*. 1965 July; 43(1): p. 139-146.
20. Boyer RF. The relation of transition temperatures to chemical structure in high polymers. *Rubber Chemistry and Technology*. 1963; 46: p. 1303.
21. Hale A, Macosko CW, Bair HE. Glass transition temperature as a function of conversion in thermosetting polymers. *Macromolecules*. 1991; 24: p. 2610-2621.
22. Zhan HY, Detwiler AT, Lesser AJ. Manuscript in review. 2011.
23. Beck Tan NC, Bauer BJ, Plestil J, Barnes JD, Liu D, Matejka L, et al. Network structure of bimodal epoxies--a small angle X-ray scattering study. *Polymer*. 1999; 40: p. 4603-4614.
24. Lovell R, Windle AH. WAXS investigation of local structure in epoxy networks. *Polymer*. 1990; 31(4): p. 593-601.
25. Wu Wl, Bauer BJ. Network structure of epoxies - a neutron scattering study: 2. *Polymer*. 1986; 27: p. 169-180.
26. Arruda EM, Boyce MC. Evolution of plastic anisotropy in amorphous polymers during finite straining. *International Journal of Plasticity*. 1993; 9: p. 697-720.
27. Kovacs AJ, Aklonis JJ, Hutchinson JM, Ramos AR. Isobaric Volume and Enthalpy Recovery of Glasses II. A Transparent Multiparameter Theory. *Journal of Polymer Science: Polymer Physics Edition*. 1979; 1097-1162.
28. Lesser AJ, Calzia KJ. Molecular parameters governing the yield response of epoxy-based glassy networks. *Journal of Polymer Science Part B: Polymer Physics*. 2004; 42: p. 2050-2056.
29. Crawford ED, Lesser AJ. The effect of network architecture on the thermal and mechanical behavior of epoxy resins. *Journal of Polymer Science: Part B: Polymer Physics*. 1998; 36: p. 1371-1382.
30. van Melick HGH, Govaert LE, Meijer HEH. On the origin of strain hardening in glassy polymers. *Polymer*. 2003; 44: p. 2493-2502.
31. Cross A, Haward RN. Orientation hardening of PVC. *Polymer*. 1978; 19: p. 677.
32. Treloar LRG. *The Physics of Rubber Elasticity* Oxford: Clarendon Press; 1975.

33. Arruda EM, Boyce MC, Jayachandran R. Effects of strain rate, temperature and thermomechanical coupling on the finite strain deformation of glassy polymers. *Mechanics of Materials*. 1995; 19: p. 193-212.
34. Haward RN, Thackray G. The use of a mathematical model to describe isothermal stress-strain curves in glassy thermoplastics. *Proceedings of the Royal Society of London Series A*. 1968; 302: p. 453-472.
35. Tervoort TA, Govaert LE. Strain hardening behavior in polycarbonate in the glassy state. *Journal of Rheology*. 2000; 44(6): p. 1263-1277.
36. Charlesworth JM. Effect of cross-link density on molecular relaxations in diepoxide-diamine network polymers 2. The rubbery plateau region. *Polymer Engineering and Science*. 1988; 28(4): p. 230-236.
37. Porter RS, Johnson JF. The entanglement concept in polymer systems. *Chemical Reviews*. 1966; 66(1): p. 1-27.
38. Hoy RS, Robbins MO. Strain hardening of polymer glasses: Effect of entanglement density, temperature, and rate. *Journal of Polymer Science: Part B: Polymer Physics*. 2006; 44: p. 3487-3500.
39. Haward RN, Young RJ. *The Physics of Glassy Polymers* New York: Chapman and Hall; 1997.
40. Wendlandt M, Tervoort TA, Suter UW. Strain-hardening modulus of cross-linked glassy poly(methyl methacrylate). *Journal of Polymer Science: Part B: Polymer Physics*. 2010; 48: p. 1464-1472.
41. Govaert LE, Engels TAP, Wendlandt M, Tervoort T, Suter UW. Does the strain hardening modulus of glassy polymers scale with the flow stress? *Journal of Polymer Science: Part B: Polymer Physics*. 2008; 46: p. 2475-2481.
42. Lesser AJ, Crawford E. The role of network architecture on the glass transition temperature of epoxy resins. *Journal of Applied Polymer Science*. 1997; 66: p. 387-395.
43. Fox TG, Loshaek S. Influence of molecular weight and degree of crosslinking on the specific volume and glass temperature of polymers. *Journal of Polymer Science*. 1955; 15: p. 371-390.
44. Espuche E, Galy J, Gerard JF, Pascualt JP, Sautereau H. Influence of crosslink density and chain flexibility on mechanical properties of model epoxy networks. *Macromolecular Symposia*. 1995; 93: p. 107-115.

45. Robertson RE. Theory for the Plasticity of Glassy Polymers. *The Journal of Chemical Physics*. 1966; 44(10): p. 3950-3956.
46. Calzia KJ, Lesser AJ. Correlating yield response with molecular architecture. *Journal of Materials Science*. 2007; 32: p. 5229-5238.
47. Bree HW, Heijboer J, Struik LCE, Tak AGM. The effect of densification on the mechanical properties of amorphous glassy polymers. *Journal of Polymer Science: Polymer Physics Edition*. 1974; 12: p. 1857-1864.
48. Charlesworth JM. Effect of cross-link density on the molecular relaxations in diepoxide-diamine network polymers 1. The glassy region. *Polymer Engineering and Science*. 1988; 28(4): p. 221-229.
49. G'Sell C, McKenna GB. Influence of physical ageing on the yield response of model DGEBA/poly(propylene oxide) epoxy glasses. *Polymer*. 1992; 33(10): p. 2103-2113.
50. Wang X, Gillham JK. Physical aging in the glassy state of a thermosetting system vs. extent of cure. *Journal of Applied Polymer Science*. 1993; 47: p. 447-460.
51. Boyce MC, Arruda EM. Constitutive models of rubber elasticity: A review. *Rubber Chemistry and Technology*. 2000; 73(3): p. 504-523.
52. Rivlin RS, Saunders DW. Large elastic deformations of isotropic materials. VII. Experiments on the deformation of rubber. *Philosophical Transactions of the Royal Society of London Series A*. 1951; 243: p. 251-288.
53. Bicerano J. Prediction of polymer properties. 3rd ed. New York: Marcel Dekker, Inc.; 2002.
54. Bicerano J, Sammler RL, Carriere CJ, Seitz JT. Correlation between glass transition temperature and chain structure for randomly crosslinked high polymers. *Journal of Polymer Science: Part B: Polymer Physics*. 1996; 34: p. 2247-2259.

## CHAPTER 4

### THE EVOLUTION OF STRESS AND STRENGTH DEVELOPMENT IN EPOXY BASED COATINGS

#### **Abstract**

Techniques are developed to monitor the evolution of residual stresses and the strength of complex multicomponent epoxy-amine based coatings. Industrial wall coatings typically contain an array of low molecular weight components. In certain environments these low molecular weight compounds may be extracted. As their concentration decreases, the physical and mechanical properties of a coating may change dramatically. We demonstrate that the loss of volatile components causes non-linear increases in density, stiffness, and  $T_g$ , of epoxy-based wall coatings. When placed under biaxial constraint, the loss of volatile components generates large residual stresses in the membranes. The development of residual stresses is monitored using acoustic excitation and inflation techniques. A third method applies fracture mechanics to simultaneously follow the evolution of stress and strength in a membrane by monitoring the growth of a crack introduced in the center of the membrane. Regardless of the complexity of the mechanisms that may cause dramatic changes in the physical properties of the membrane materials, the material properties that are critical to the integrity of the coatings can be monitored by simply measuring the dimensions of a crack and the modulus of the material. These techniques can be applied to any self-supporting membrane undergoing a variety of curing, ageing, or degradation processes.

## **Introduction**

Epoxies have been used as coatings since the development of epoxy chemistry in the 1930's (1). The prevalent use of epoxies is attributed to their favorable handling characteristics, good adhesion, strength, toughness, and solvent resistance. In addition, a wide variety of curing agents can be used to tailor their physical and mechanical properties. The reactions between epoxide monomers and amine or anhydride curing agents do not generate any small molecule condensation byproducts, and they are relatively insensitive to adventitious moisture and oxygen. Therefore, epoxy based materials can often be processed without special environmental controls such as the exclusion of oxygen and moisture or rigorous surface preparation.

Due to the ease of handling and tunability of epoxy amine formulations, they are often employed in coatings applications. Cross-link density and thermal and mechanical properties can be controlled by the ratios of different epoxide and amine monomers. In order to facilitate application by spraying, rolling, or painting onto surfaces, thixotropic fillers, solvents, and other rheological modifiers are introduced into the epoxy-amine base. Pigments, stabilizers, and antioxidants are other additives that might also be included. In order to compatibilize all the components, various solvents, dispersants and emulsifiers are added. Different formulations can be created to meet specific requirements such as fast cure times, low volatile organic compounds (VOC) content, and resistance to specific chemical environments. The results of all this tunability are complex multicomponent formulations. The physical and mechanical properties evolve through curing and/or drying processes from the time the coating is mixed and applied to a wall as a liquid, and throughout its service lifetime as a cross-linked solid. Additional

factors such as coating thickness, the substrate, temperature, humidity, and exposure to other chemicals may change how the physical and mechanical properties of the coating evolve over its service lifetime.

Since coatings are often applied to protect vulnerable surfaces from any number of aggressive environments, resistance to cracking is one of the basic requirements. Numerous authors have investigated model systems in order to gain a fundamental understanding of the structure-process-property relationships that control failure in coatings. Two critical factors that govern coating integrity are the solvent and the conversion. Loss of solvent causes a decrease in the volume of a coating. If the coating is constrained by a substrate the change in volume may be limited to certain directions, such as orthogonal to the surface of the coating. Therefore, the change in volume of a geometrically constrained coating leads to the development of residual stresses. Reaction of an epoxide with an amine or anhydride curing agent results in cure shrinkage, which adds to the stresses generated from loss of solvent.

Changes in intermolecular and inter-particle interactions due to solvent loss and curing will change the cohesive strength of a coating. The presence of any flaws such as bubbles, scratches, or cracks will concentrate any residual or applied stresses that are acting on a coating. The local stress field in the vicinity of these flaws may exceed the strength of the coating, at which point a crack will grow. In the case of a coating where cracks are not actively growing, the strength of the coating is greater than the combination of stresses generated internally and externally. However, the strength of a coating and the stresses induced by the many processes that occur simultaneously (i.e. curing, drying, physical ageing, mechanical deformation, etc.) may evolve along

convoluted non-linear paths over the lifetime of the coating. Therefore, in order to avoid crack growth, formulations must be tailored to develop low residual stresses and to achieve sufficiently high strength.

In this work we investigate the evolution of residual stresses in complex multicomponent epoxy-amine based coatings. The coatings are biaxially constrained circular membranes which model the stress state experienced by wall coatings in service. The development of residual stresses is monitored using three different methods. The first method relates the resonant frequencies of acoustically excited membranes to their residual stresses. The second method relates the orthogonal displacement of the center of a membrane to the air pressure applied to the opposite side to determine the residual stress. The third method uses fracture mechanics to simultaneously follow the evolution of stress and strength in a membrane by monitoring the growth of a large crack in the center of the membrane. The power of these techniques arises from the fact that they are able to characterize the evolution of those materials properties which are most relevant to the integrity of a coating, regardless of the complicated mechanisms that cause these changes.

## **Method**

The two part coating formulation consists in the epoxide part, based on DGEBA-type epoxide monomers and the amine part, based on isophorone diamine (IPDA). Both parts also contain inorganic silica and titania fillers, other solvents and numerous proprietary additives. The epoxide and amine parts are mixed together in a 3:1 ratio in a glass beaker with a PTFE coated magnetic stir-bar and a stirring rods for five minutes, yielding a viscous opaque white liquid.

Two glass plates with dimensions 15 x 25 x 0.6 cm are coated with a silane based release agent (Surfasil, Pierce Chemicals). A border of tape 12 mm wide and 0.15 mm thick is applied to the periphery of three sides of one plate to serve as a spacer between the glass plates. Approximately 10 g of the coating mixture is poured in a thick line near the bottom of the plate. The other plate is pressed onto the plate with the tape border to spread the coating over the entire inside surface of the mold. Metal binder clips are placed around the border of the plates to hold them together. The coating is allowed to cure at 23°C for 4 days. After four days, the glass molds are cooled to -10°C in a freezer in order to facilitate the separation of the plates. The coating membrane is carefully removed from the plates to avoid stretching or tearing.

A circular template is placed on the free films, and circles 63.5 mm in diameter are cut from the film using a razor blade to trace the template. If the films are to be precracked, a template is used to guide a razor blade which cuts a 12 mm crack ( $2a = 12\text{mm}$ ) in the center of the circle. Steel washers 0.79 mm thick with inner diameter 45 mm, and outer diameter 70 mm, are used to provide radial constraint on the membranes. A thin layer of 5-minute epoxy (Devcon) is applied to one side of each washer. A circular membrane is centered on one washer, and the other is pressed on top, thus permanently binding the membrane and washers and preventing slippage between the membranes and the washers. Six binder clips are distributed around the circumference of the washers to hold them together while the 5-minute epoxy cures. Membranes containing a 12 mm center crack and membranes without precracks are placed in an oven at  $55 \pm 2^\circ\text{C}$ . Crack length ( $2a$ ) and crack opening displacement ( $2\delta$ ) are measured optically from

photographs of cracked membranes (Nikon D40 with 55 mm zoom lens) using Image J software (2). The cracked membranes are photographed through a window in the oven.

Glass transition temperatures ( $T_g$ ) are measured with a DSC Q200 (TA Instruments) differential scanning calorimeter from the inflection point of the heat flow vs. temperature ( $dH/dT$ ) curve from heating 5 mg samples at 10°C per minute. Initial density is calculated by dividing the weight of a 63.5 mm diameter circular membrane by its volume, where the thickness is taken as the average of five measurements at different locations measured to the nearest 2  $\mu\text{m}$  with a micrometer. Densities of conditioned membranes are calculated from the values measured for free membranes with comparable conditioning histories. The masses of free-standing films of known dimensions are used to calculate weight loss.

Samples for dynamic mechanical thermal analysis (DMTA Q800 from TA Instruments) are cut to approximate values of Length x Width of 30 x 5 mm<sup>2</sup> for testing using the tension geometry. Temperature sweeps are run at 1 Hz, 15  $\mu\text{m}$  displacement and a ramp rate of 3°C/min from -120-120°C. The storage modulus ( $E'$ ), loss modulus ( $E''$ ), and loss tangent ( $\tan \delta$ ) are recorded. The tensile modulus ( $E$ ) is measured in an isothermal test at 55°C and a strain rate of 2 %/min.

Thermal gravimetric analysis (TGA) of 10 mg samples is done under a nitrogen atmosphere and a heating rate of 10°C per minute using a TGA Q500 (TA Instruments). The weight loss observed at 275°C in the TGA trace is taken as the total content of volatile components. An isothermal condition is also used to measure weight loss as a function of time at 55°C.

An acoustic frequency sweep is applied to excite uncracked membranes for acoustic stress analysis. The Sound Forge (Sony) software program is used to generate frequency sweeps from 60-2060 Hz at a rate of 1000 Hz/min. The signals are converted to sound using an HK 195 (Harman/Kardon) computer speaker. Membrane assemblies are placed on a cedar board with a 50 mm diameter hole in it for sound transmission. Sound is recorded with a Snowball (Blue Microphones) omni-directional USB microphone in the 10 dB PAD mode. The data is acquired by the Sound Forge software as sonograms which consist in the amplitude with units of sound pressure level (SPL) at a sampling rate of 44.1 kHz. Polyurethane foam is used to isolate the microphone from sounds that are not emitted by the membrane.

For the membrane inflation experiment biaxially constrained membranes are placed in an oven at 55°C to accelerate the evaporation of volatile components. In order to inflate the membranes, they are clamped between two flanges with rubber gaskets to form seals. The opening in the flange on the atmospheric pressure side of the membrane is large enough to avoid interference with the inflating membrane. Pressurized air is routed through a manually operated back-pressure controlled regulator (Bellofram Type 70, 0-30 psi range). An Omega PX300-100GV pressure transducer is used to measure the inflation pressure. An Omega LD300-25 linear variable differential transformer (LVDT) is used to measure displacements at the center of membranes. The LVDT is interfaced with a National Instruments 1540 SCXI data acquisition card and a Labview program to coordinate data collection. The LVDT voltage/displacement response is calibrated over a 25 mm range with a Boeckeler micrometer.

## **Results and Discussion**

The evolution of the basic physical and mechanical properties of the epoxy-amine based membrane materials will be described first, followed by discussion of the more advanced experiments used to monitor the evolution of stresses and strength as biaxially constrained membranes are subjected to elevated temperature conditioning. The membrane materials are cured between glass plates at room temperature for four days prior to any testing, which allows the reactive components to approach the maximum conversion possible at room temperature without evaporation of solvent. When the coatings are first removed from the glass plates they are pliable and leathery. Based on DSC temperature scans,  $T_g$  is initially below room temperature, and it increases with conditioning at 55°C, as indicated in Figure 4-1. Therefore, the curing at room temperature takes place while the membrane material is rubbery.

Although  $T_g$  is a function of conversion in epoxy resins, it can be significantly decreased by the presence of a plasticizer, such as a solvent. Based on a TGA temperature sweep of the membrane material immediately after removal from the glass mold (Figure 4-2), it appears that approximately 20% of the initial weight is lost before the epoxy component begins to degrade around 325°C. Since the proprietary formulation is known to contain benzyl alcohol, which has a boiling point of 209°C, and other low molecular weight additives the initial weight loss can be attributed loss of these compounds. IPDA is a tetrafunctional amine so there should be an insignificant amount of completely unreacted amine molecules that might volatilize. The ~25% residual weight at 600°C is attributed to the inorganic fillers that are typically present in industrial epoxy-amine coatings.

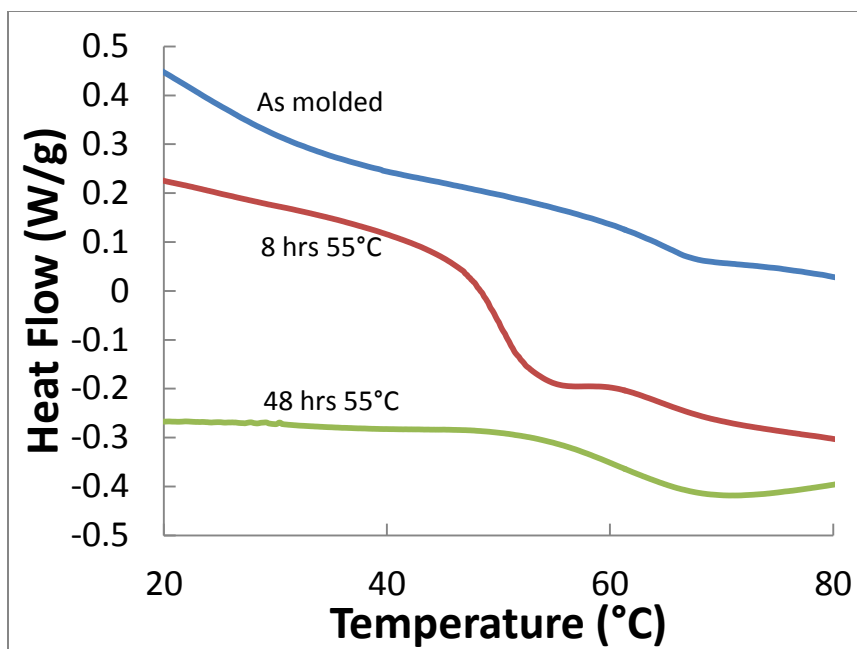


Figure 4- 1 DSC temperature scans of membrane materials. Tested immediately upon removal from the mold (top), after 8 hours of conditioning at 55°C, and after 48 hours of conditioning at 55°C. The membrane materials exhibit a clear progression toward higher  $T_g$  during conditioning at 55°C.

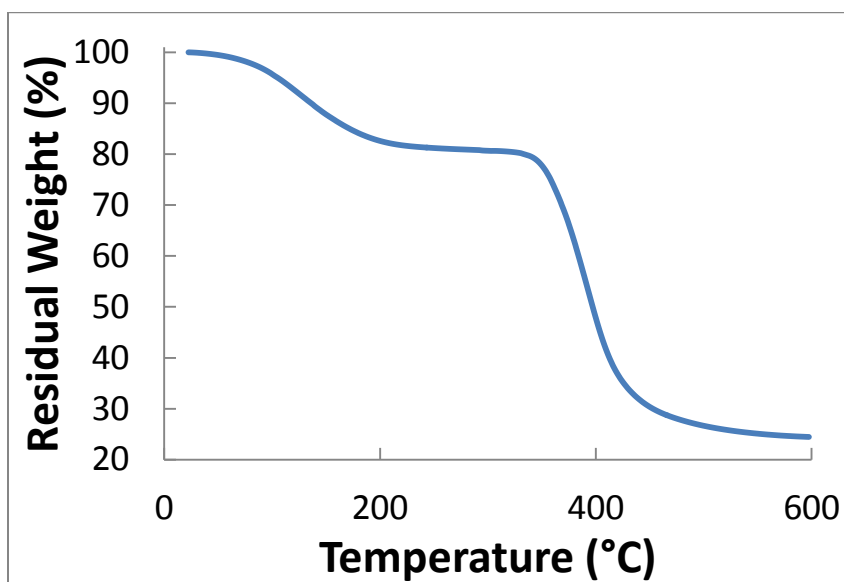
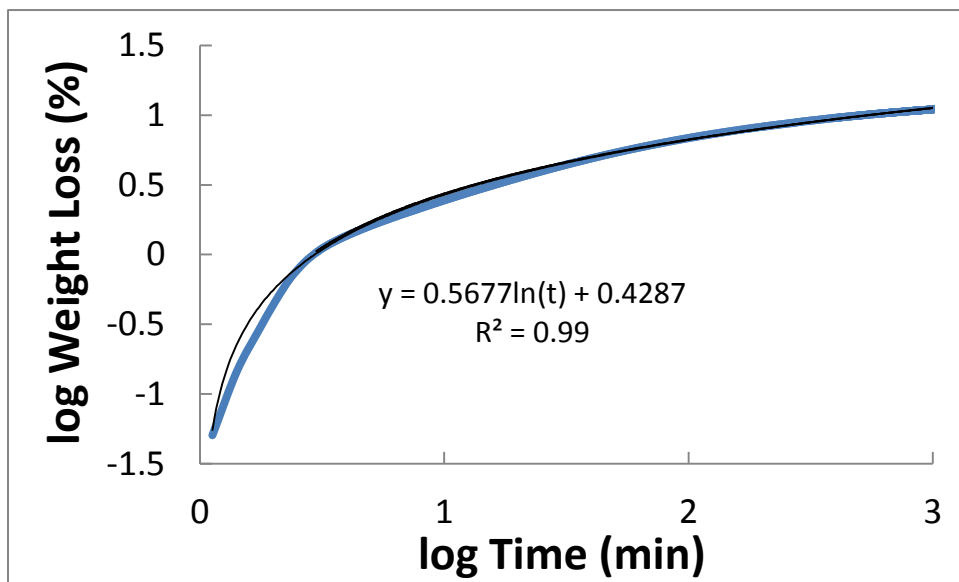


Figure 4-2 Residual weight vs temperature from a TGA temperature scan on membrane material immediately after removal from glass molds. The initial weight loss is attributed to loss of benzyl alcohol and other small molecules. The second drop is due to thermal degradation of the epoxy. The residual weight at 600°C indicates the presence of ~25wt% inorganic fillers.

Although the weight loss observed at 55°C in Figure 4-2 is approximately 1%, the small molecule components have some finite vapor pressure, and they are expected to evaporate over time at any temperature that might be encountered by a coating in service.

Figure 4-3 shows weight loss of the membrane material as a function of time from an isothermal TGA experiment run at 55°C.

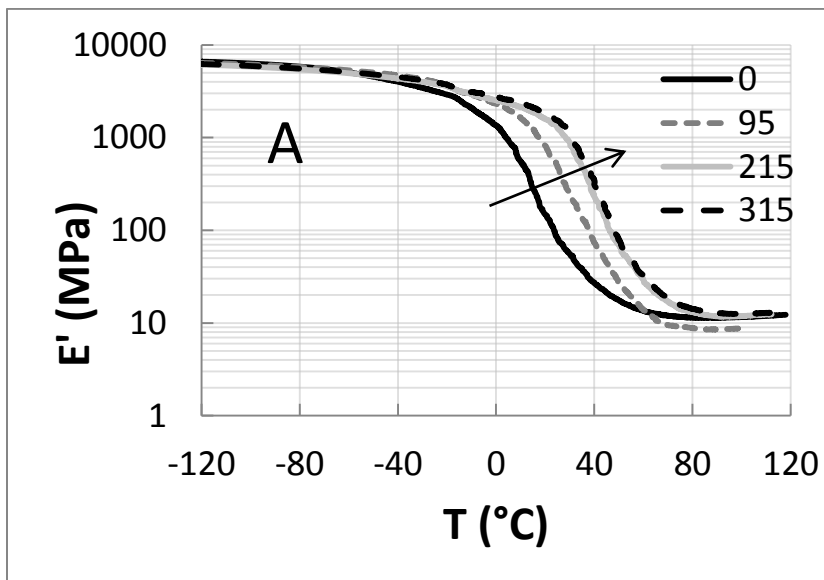


**Figure 4-3. Log-log plot of weight loss vs time during isothermal conditioning of membrane material freshly removed from glass mold. The rate of weight loss is initially much higher than the rate after ~10 minutes at 55°C, which indicates that a much more volatile solvent is initially depleted, followed by evaporation of the less volatile benzyl alcohol.**

The logarithmic fit to the weight loss curve in Figure 4-3 indicates a logarithmic decay from a relatively high rate of weight loss initially to a much lower rate at longer times. The decay in rate of weight loss can be attributed to both the depletion of the solvent very near the surface of the membrane material and the diffusion of the solvent from the bulk.

The low molecular weight components in the coatings do not contribute to the cross-linked network, and they act as plasticizers, which depress  $T_g$ . As these compounds evaporate, the  $T_g$  increases, as observed from the DSC traces in Figure 4-1. Another

effect of plasticizers is to reduce the stiffness of a cross-linked network by interfering with the intermolecular interactions between network chain segments. By removing the small molecules, the fraction of the organic material that is involved in the cross-linked network increases, the intermolecular interactions of the network chain segments strengthen, and the effective fraction of inorganic content increases. All of these changes, which arise from loss of small molecules, increase the stiffness of a coating material. Temperature scans of the membrane material using DMTA in the tension geometry highlight some of the changes that are observed in the mechanical behavior of the coating material during conditioning at 55°C.



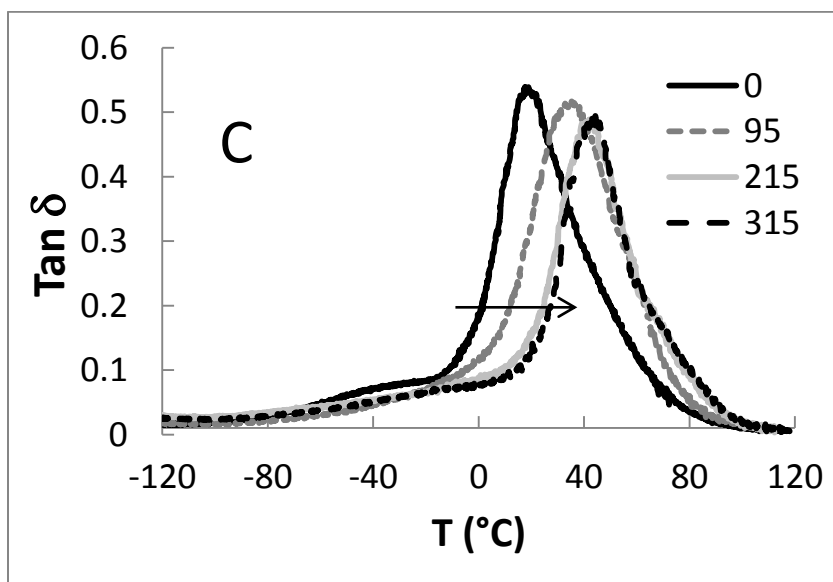
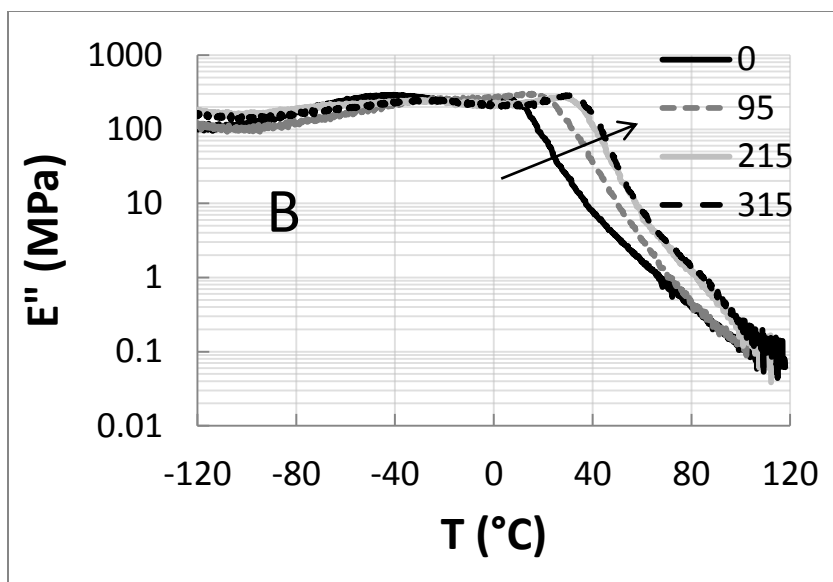


**Figure 4-4 DMTA temperature sweeps of coating material conditioned at 55°C. Conditioning time is given in minutes for each curve in the legend of each plot, and the arrows point in the direction of increasing time. A) Storage modulus B) Loss modulus C)  $\tan \delta$ . The DMTA curves indicate that  $T_g$  shifts to higher temperature during conditioning, and the broad  $\tan \delta$  peaks indicate the materials are very heterogeneous.**

From Figure 4-4 it is clear that there is a  $\sim 40^\circ\text{C}$  shift in the  $T_g$  during the conditioning procedure at 55°C. However, based on the  $\tan \delta$  curves the  $T_g$  transition spans  $\sim 80^\circ\text{C}$ . Therefore, the mechanical properties of the membrane materials are extremely sensitive to temperature in the vicinity of room temperature and above. In

agreement with the weight loss data,  $T_g$  initially shifts significantly with time, and the changes slow down dramatically, for example, between 215 minutes and 315 minutes. In addition, at these longer times  $T_g$  approaches the conditioning temperature. Therefore, the membrane materials approach a glassy state at 55°C where they have higher modulus and greater energy dissipation capabilities. Figure 4-5 shows the increase in the elastic modulus with weight loss, as measured in tension at 55°C.

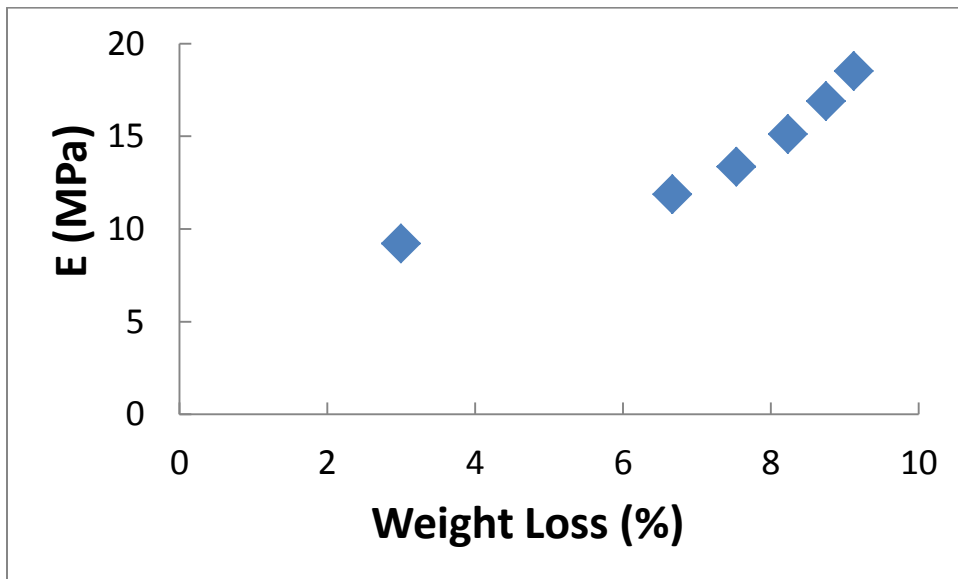


**Figure 4-5. Elastic modulus versus weight loss measured in tension at 55°C. The elastic modulus increases due to the loss of volatile components.**

It is clear from the characterization of the thermal and mechanical properties of the membrane materials that the loss of solvent has a dramatic effect on the evolution of the materials properties during conditioning at elevated temperature. The next section will address the techniques and analysis necessary to characterize the evolution of stresses and the strength of biaxially constrained membranes under elevated temperature conditioning.

## Acoustic Stress Measurement

A circular membrane which is bound around its circumference has some radius (a) and thickness ( $h_0$ ), where  $h_0 \ll a$ . In the case of an ideal membrane, the membrane has zero bending stiffness, whereas it behaves as a plate when bending stiffness is finite. However, as the ratio of the radius to the thickness increases, ideal behavior is approximated. The membranes in the current work have  $a/h_0 > 100$ , so they can be treated as ideal membranes, as opposed to plates. An ideal membrane can be modeled as a mechanical resonator with simple relationships between frequency, the speed of transverse waves in the membrane, the tension on the membrane, and the mass per unit area (3). The angular frequencies at which normal modes resonate are functions of tension (T) and areal density (M), according to Equation 4-1.

$$T = \left( \frac{\omega_{mn} a}{\gamma_{mn}} \right)^2 M \quad [4-1]$$

Where  $\omega_{mn}$  is the angular frequency in (*rad/s*) and  $\gamma_{mn}$  is a coefficient that depends on the mode and order of free vibrations of the membrane. The subscripts refer to the n-th mode of the m-th order vibration. Values for the constant  $\gamma_{mn}$  are given in Table 4-1 for the first few normal modes. The fundamental frequency ( $\omega_{01}$ ) is the frequency at which the entire membrane vibrates in phase. It has zero lines of radial symmetry, given by m, and one line of axial symmetry, given by n, which occurs about the circumference.

**Table 4-1. Values of  $\gamma_{mn}$  determining the frequencies of free vibration of a circular membrane (3).**

n	m = 0	m = 1	m = 2	m = 3
1	2.405	3.832	5.136	6.380
2	5.520	7.016	8.417	9.761
3	8.654	10.173	11.620	13.015

The (0,1) mode represents the lowest resonant frequency of a membrane.

Essentially any excitation of the membrane, through the action of an oscillating force, an impulse, or some other forcing function; will cause the membrane to vibrate. However, the symmetry of the membrane limits the resonant frequencies to specific values that satisfy Equation 4-1. Other frequencies are strongly attenuated. Unlike in 1-dimensional systems, resonant frequencies in two dimensional membranes are not harmonic.

Vibrations in two dimensions are described as leaving a wake, where the wavelength of a two dimensional wave changes as it propagates, as opposed to merely decreasing its amplitude (4).

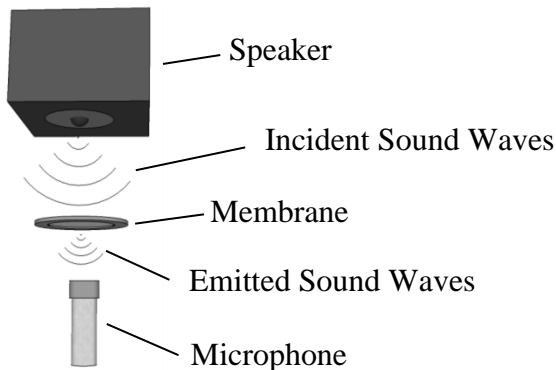


**Figure 4-6. Acoustic testing assembly. The microphone is acoustically isolated from the speaker, but this is not shown in order to simplify the schematic.**

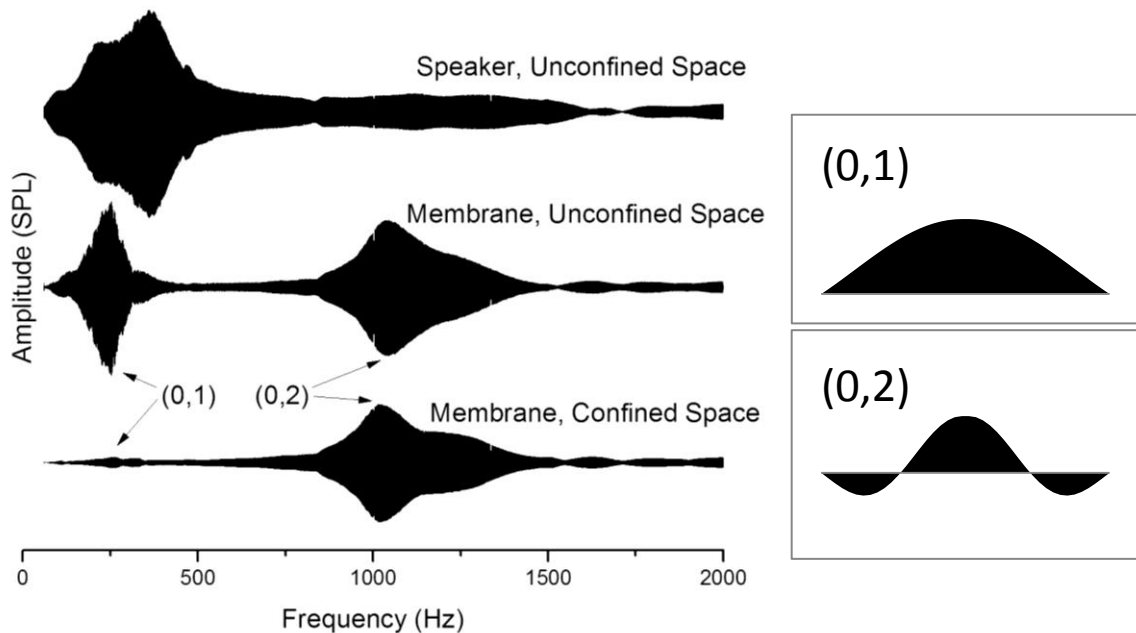
A simplified diagram of the acoustic stress measurement setup is depicted in

Figure 4-6.

Sonograms are the digitized response of the microphone to the sound emitted from the membrane, which is excited by the incident sound waves from the speaker. The membrane is placed over a circular hole in a sound-insulating cabinet such that the sound emitted by the membrane forms the vast majority of the sound energy impinging on the microphone. The volume of the frequency sweep for the speaker was set to half that used for the membrane measurements to avoid clipping of the loudest sounds. A Fast Fourier Transform (FFT) can be applied to the sonograms to obtain the data in terms of the amplitude of the membrane response versus the frequency of the response. The peaks observed in the FFT (not shown) correspond to the sweeping frequency as well as any lower resonant frequencies. Therefore, the peaks in the sonograms represent the frequencies of the normal modes of the membranes. It is assumed that the first peak in the middle sonogram of Figure 4-7 corresponds to the (0,1) mode, wherein the entire membrane oscillates up and down in phase. The peak occurring around 1000 Hz in the sonogram is the second resonance, corresponding to the (0,2) mode. The (0,2) mode has two circular nodes with zero displacement; one at the outer radius and one at  $r=a(\omega_{01}/\omega_{02})$

(4). Out-of-plane displacements are radially symmetric, as depicted in Figure 4-8.

Techniques such as holographic interferometry or laser Doppler velocimetry can give direct images or measurements of displacements on a membrane while it is vibrating. However, these techniques require significant investments in equipment and experimental setup. A much simpler method of determining whether a vibration might be the (0,1) mode versus the (0,2) mode is to place the membrane over a confined space. Since the (0,1) mode displaces air on each side of the membrane as it oscillates up and down, the volume of the confining space changes continuously.



**Figure 4-7. Sonograms representing the amplitude in units of sound pressure level of the measured responses of membranes to acoustic frequency sweeps. Top curve: baseline response of the speaker and microphone with no membrane. The middle curve is the sonogram of a membrane where both sides of the membrane are open to atmospheric pressure. The bottom curve is the sonogram of the membrane response where the membrane forms a seal over a chamber containing the microphone such that pressure equilibration between the chamber and the atmosphere is much slower than the acoustic frequencies. The profiles at the right show the shapes of the (0,1) and (0,2) modes.**

The air in the confined space resists these volume changes and the amplitude of the oscillations is reduced. The (0,2) mode has displacements both into and out of the plane of the membrane so the volume change during each oscillation is very small. One would predict the (0,2) mode to be slightly damped, but much less so than the (0,1) mode. The sonogram labeled “Confined Space” in Figure 4-7 was recorded by placing the microphone in a jar. A soft gasket formed from modeling clay was placed around the rim of the jar, and the membrane assembly was pushed onto the clay to form a seal. The first peak in the sonogram near 250 Hz is strongly damped in the “Confined Space” configuration, whereas the peak at 1000 Hz is only slightly damped, as expected.

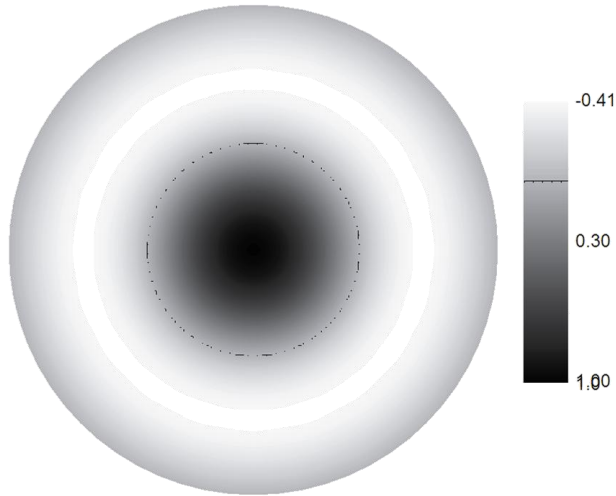


**Figure 4-8. Contour plot of (0,2) normal mode. Darker regions are projected out of the plane and lighter regions project into the plane. The hashed circle represents the nodal circle with zero displacement.**

In considering which vibration mode to use for analysis it should be noted that any displacement of the membrane also displaces air, thus increasing the effective mass of the membrane. The result is that resonant vibrations are shifted to higher frequencies. This effect has been demonstrated experimentally by Chobotov and Binder in their work on membranes at sub-atmospheric pressures (5) and is treated theoretically by Morse (3). Farris et al. have used piezoelectric motors to vibrate membranes at controlled frequencies under vacuum (6). Using real-time holographic interferometry they were able to measure stresses on the membranes without the effects of air resistance. However, the velocities of sound waves in air (~331 m/s) are much higher than transverse wave speeds in membranes (~80m/s), so the *average* displacement of the membranes governs the effect of the air on the resonance. By using the second resonance mode (0,2), which has low net displacement, we are able to obtain more accurate values for the tension on the membranes. The progression of the frequencies of the (0,2) resonance mode is plotted as a function of weight loss in Figure 4-9.

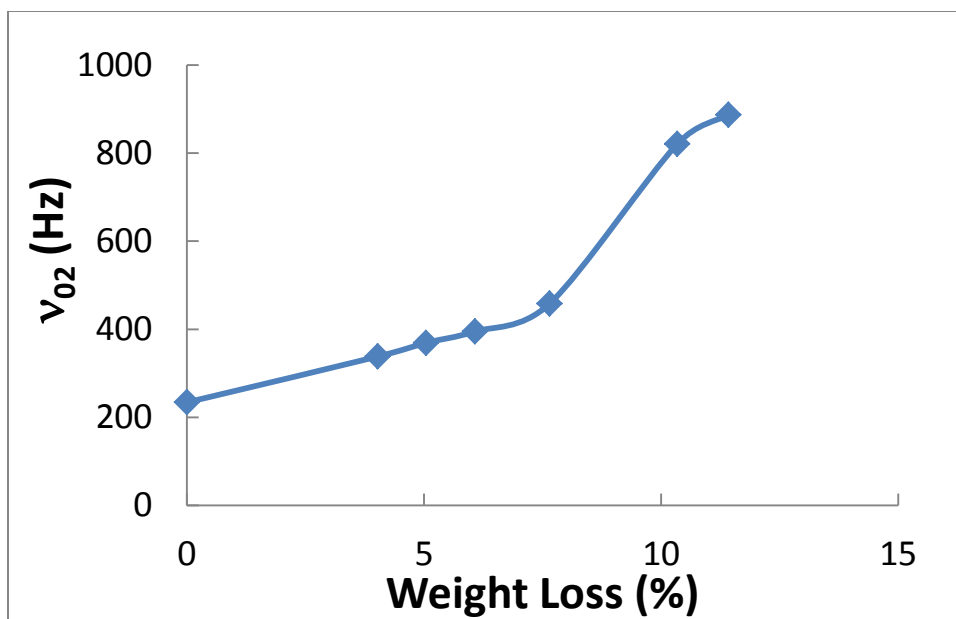


**Figure 4-9. Resonant frequency of the (0,2) mode as a function of weight loss for a membrane conditioned at 55°C. The increase in the resonant frequency with weight loss indicates increasing tension on the membrane. The line is to guide the eye.**

Once the resonant frequency and the vibration mode are known these values can be plugged into Equation 4-1 to calculate the tension ( $T$ ). The tension is divided by the thickness ( $h_0$ ) to give the stress. It is clear from the stress versus weight loss data plotted in Figure 4-10 that there is a certain amount of weight loss required before large stresses develop that might drive crack growth. The increase in stress due to weight loss accelerates around 7% weight loss. This acceleration of stress development is caused by the increase in the stiffness of the material, which is also related to the increase in  $T_g$  that accompanies loss of solvent. Glassy materials are much stiffer than rubbery materials, so as  $T_g$  increases toward the conditioning temperature the stiffness of the material increases. This behavior is obvious from both DMTA and tensile modulus measurements. However, the acoustic technique was used at room temperature as opposed to 55°C where the conditioning takes place.

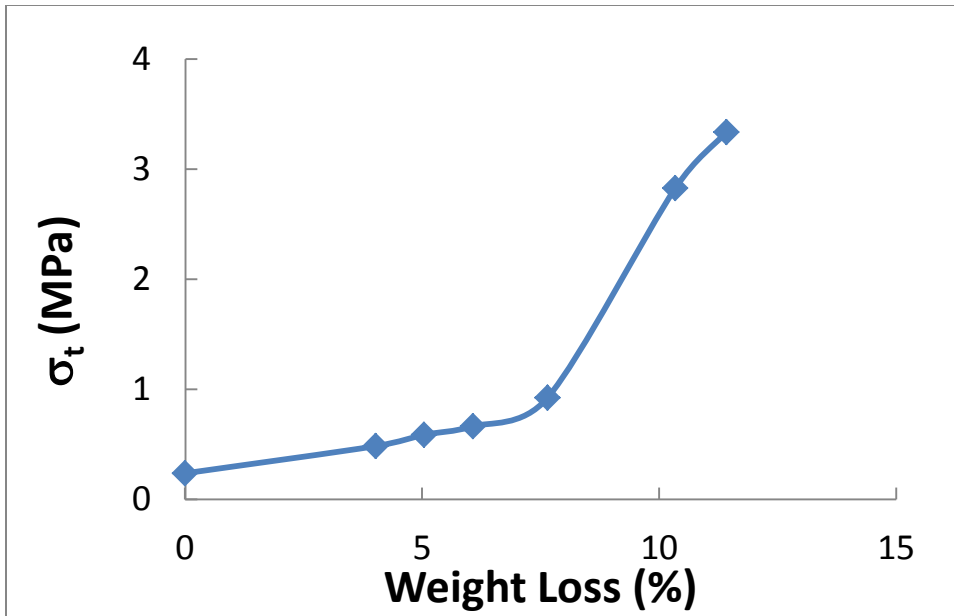


**Figure 4-10. Stress vs weight loss. Stress is calculated based on the (0,2) mode. Line is to guide the eye.**

Therefore, the stresses measured at 23°C are artificially high relative to the stresses generated at 55°C. A different technique allowing stress to be measured at 55°C in an oven is more attractive since it should eliminate the additional complication of interpreting the effects of thermal expansion and large changes in modulus over this temperature range.

### **Stress Measurement: Inflation**

The setup for this stress measurement is shown in Figure 4-11 below. A small dot of chalk is used to mark the center of the membrane assembly. This dot will serve as the target for the LVDT probe. The membrane assembly is then placed between two steel flanges. The membrane assembly, with the gaskets in place, is sealed between the two flanges by tightening the four flange nuts and bolts to finger tightness. The flanges with the membrane assembly are fastened to the testing frame with C-clamps. The position is adjusted such that the LVDT probe contacts the chalk mark at the center of the

membrane. An air hose with the pressurized air from the pressure regulator is attached to the rear of one of the flanges. This air hose should be sufficiently long that ~2 meters of hose are able to fit in the oven such that any air that contacts the membrane assembly is preheated before reaching the flange connection.

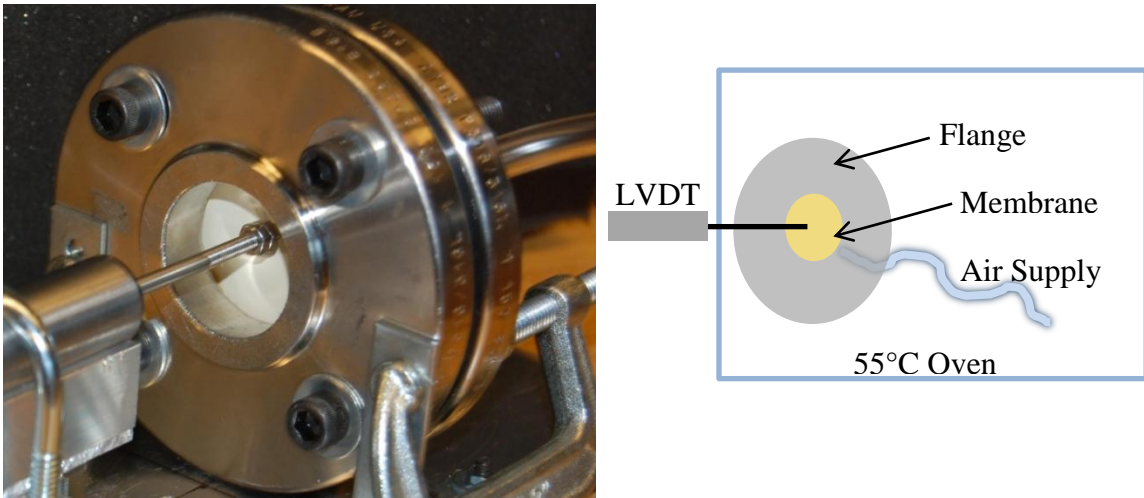


**Figure 4-11. Photograph (left) of the inflation setup with LVDT, flange, membrane, and air supply. Schematic (right) with components labeled and sealed in an oven during a measurement.**

In order to seal the flange, membrane assembly, and air hose in the oven while the LVDT remains outside, a polycarbonate window is inserted between the body of the LVDT and the flange. A hole just large enough to accommodate the LVDT probe is cut in the window so the probe of the LVDT can enter the oven while minimizing heat loss. Any spaces between the oven and the window are insulated with soft polyurethane foam to reduce heat loss. Once the test setup is in the oven with the window in place, the test setup is allowed to heat up to the oven temperature for 20 minutes. The steel flanges are stored at 55°C between measurements to reduce temperature equilibration time.

In the membrane inflation technique a pressure gradient is applied across a membrane, and the resulting deformation is measured at the pole of the membrane. The stress state at the pole is one of biaxial tension. Assuming a spherical shape for the

membrane as it inflates, it is then possible to calculate the extension ratios in the circumferential and radial directions.

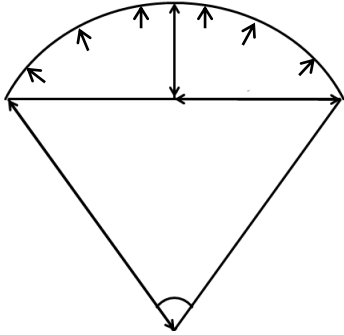


**Figure 4-12 Membrane Inflation Diagram**

In the bubble inflation diagram the displacement of the pole of the membrane from its initial position is given by  $L$ .  $R_0$  is the initial radius of the membrane,  $\rho$  is the radius of curvature, and  $\theta$  is the angle between the edges of the membrane and the vertex at the radius of curvature. Equations 4-2 through 4-5 outline the calculations involved in calculating the true stress at the pole ( $\sigma_t$ ) as a function of inflation pressure ( $P$ ), biaxial extension ratio ( $\lambda$ ), and initial membrane thickness ( $h_0$ ).

$$\sigma_t = \frac{P\lambda^2\rho}{2h_0} \quad [4-2]$$

$$\rho = \frac{R_0^2 + L^2}{2L} \quad [4-3]$$

$$\lambda = \frac{\rho\theta}{2R_0} \quad [4-4]$$

$$\theta = \sin^{-1} \frac{R_0}{\rho} \quad [4-5]$$

Equation 4-2 relates the stress on the membrane to the displacement of the pole of the membrane and the inflation pressure. By extrapolating the stress-pressure curve to zero pressure we are able to calculate the stress on the membrane caused by the loss of volatile components. This procedure is demonstrated in Figure 4-13.

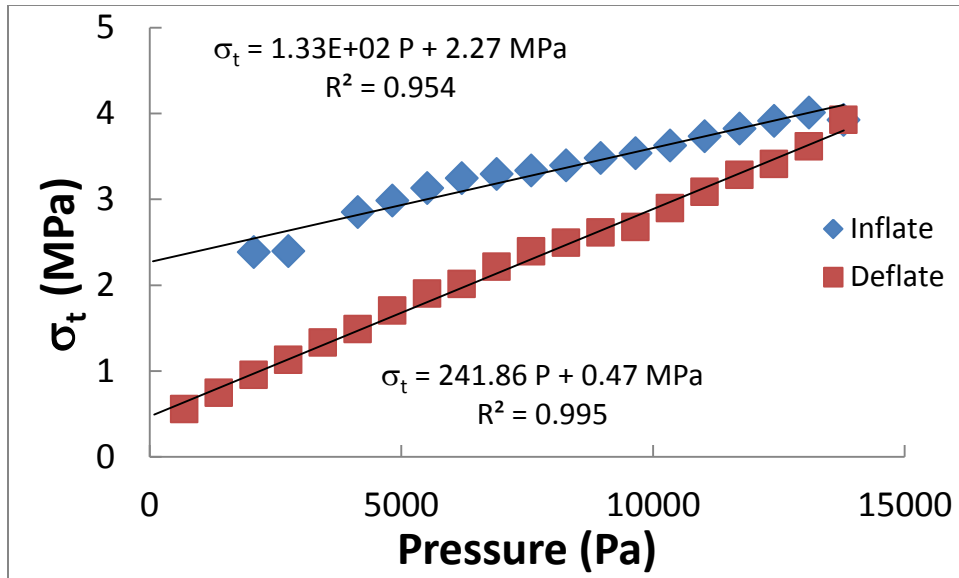


Figure 4-13. Plot of membrane stress vs inflation pressure measured at 55°C during inflation (blue diamonds) and deflation (red squares) at 6.3% weight loss, corresponding to the initiation of macroscopic crack extension at 55°C. The black linear regression lines are extrapolated to zero inflation pressure. The intercept of the regression line with the stress axis is the residual biaxial stress on the membrane.

The residual stress that develops in a biaxially constrained membrane is taken as the intercept of the linear regression of the stress at the center of a membrane versus the applied air pressure. This measurement can be made relatively easily at elevated temperatures or with the membrane immersed in a liquid, which makes it somewhat more flexible than the acoustic stress measurement technique. However, viscoelastic effects from the large stresses and very low strains that are applied to the membrane cause the membrane to achieve a certain amount of creep during the measurement. This phenomenon causes the difference in the slope and intercept of the inflation data relative to the deflation data. The residual stress that was measured during inflation appears to decrease significantly in the deflation data due to the applied stress and deformation the membrane has experienced. These results demonstrate the importance of the thermomechanical history of these membrane materials when they are being

characterized. Therefore, this technique can only be used to measure the stress on a membrane once.

Crack growth also dissipates strain energy, so the stresses measured in uncracked membranes do not account for the strain energy that has been dissipated by crack growth. Instead, uncracked membranes provide a measure of the maximum stress able to be generated due to solvent loss. Simultaneous measurements of both stress and the characteristic dimensions of a crack from the same sample are necessary to be able to monitor stress and strength in cracked membranes. However, the two techniques for stress measurement described above are unable to be used on cracked membranes. The vibrations imposed on a cracked membrane using the acoustic technique would cause fatigue crack growth, particularly as the stresses become high. The inflation technique fails with a cracked membrane due to the lack of a proper seal. Although alternative processes might be proposed, two relatively simple experimental techniques are developed in the next section to treat the evolution of both stress and strength in center-cracked biaxially constrained membranes as functions of solvent loss.

### **Membrane Strength Measurements**

The solutions for the stress intensity factors for circular membranes under biaxial stress fields have been reported by Bowie (7) and Tada (8). The stress intensity factor for a center cracked biaxially constrained membrane is given by Equation 4-6.

$$K_{\sigma_{\infty}} = \sigma_{\infty} \sqrt{\pi a} \cdot F_1\left(\frac{a}{b}\right) \quad [4-6]$$

Where  $\sigma_{\infty}$  is the far-field stress,  $a$  is the half crack length,  $b$  is the radius of the membrane, and  $F_1(a/b)$  is a function which corrects the stress intensity factor for the

biaxial constraint condition. This solution was obtained by Bowie (7). Figure 4-14 displays a polynomial fit to the graphical solution provided by Bowie.

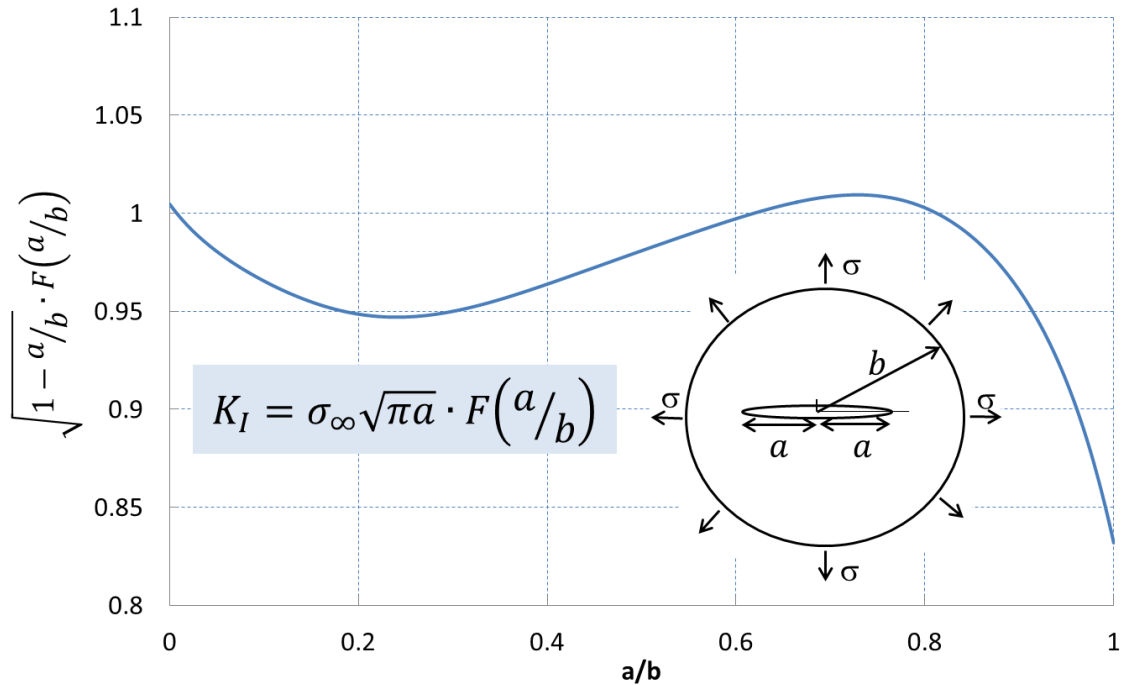


**Figure 4-14. Polynomial fit of the graphical solution for  $K_I$  for equibiaxial stress on a center cracked membrane. Inset is a schematic of the geometry of the cracked membrane.**

The stress intensity factor for a point load is given by Equation 4-7.

$$K_q = \frac{q}{\sqrt{\pi a}} \cdot F_2\left(\frac{a}{b}\right) \quad [4-7]$$

Where  $F_2(a/b)$  is given by a polynomial fit to the graphical solution provided by Tada (8) in Figure 4-15. The stresses on a cracked membrane cannot be determined directly as was done with uncracked membranes using the acoustic and inflation techniques above. Therefore, it is necessary to relate the displacement field to the stresses in a cracked membrane.

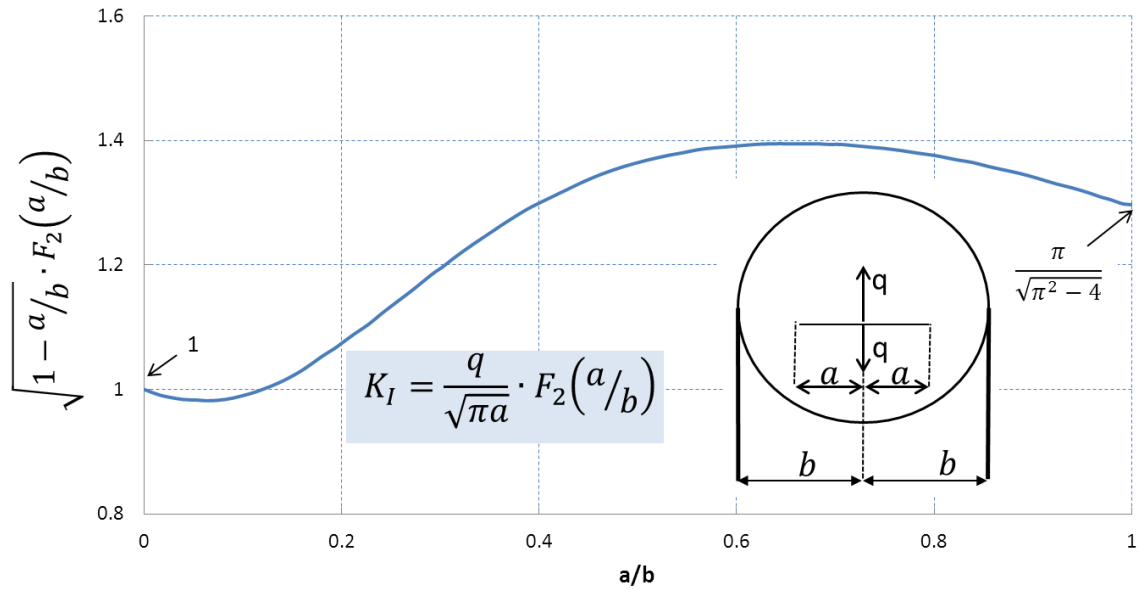


Figure 4-15. Polynomial fit to the solution curve for the stress intensity due to a point load on a circular membrane. Solution is from Tada (8).

### Method of Virtual Work

The method of virtual work allows one to determine the displacement at a specific point in based on the virtual work done on a mechanical system to achieve the displacement. In the current analysis, we have the stress intensity factors for an elliptical crack in the center of a biaxially constrained membrane, and that for a point load acting on the membrane. In the limit that the point load is equal to zero, the displacement at a given point along the crack can be determined from the derivative of the elastic potential (II) with respect to the point load (q), evaluated for q=0. The elastic potential is equal to the integral of the strain energy taken over the length of the crack. The derivation which leads to the determination of the displacement is given below.

The total stress intensity factor ( $K_T$ ), according to the method of virtual work, in this case is the sum of that contributed by the far-field stresses ( $K_{\sigma\infty}$ ) and the point load ( $K_q$ ) as given by Equation 4-8.

$$K_T = K_{\sigma\infty} + K_q \quad [4-8]$$

Based on linear elastic fracture mechanics (LEFM), the energy release rate is the derivative of the elastic potential ( $\Pi$ ) with respect to the crack length ( $a$ ). Thus the energy release rate is equal to the integral of the energy release rate integrated over the entire crack.

$$G = \frac{\partial \Pi}{\partial a} = \int_{-a}^a \frac{K_T^2}{E'} dx \quad [4-9]$$

The displacement at the center of the crack is equal to the derivative of the energy release rate with respect to the virtual load applied at the center of the crack, where the virtual load is taken to be equal to zero.

$$\delta_c = \left[ \frac{\partial}{\partial q} \frac{\partial \Pi}{\partial a} \right]_{q=0} = \int_{-a}^a \left[ \frac{\partial}{\partial q} \left( \frac{K_T^2}{E'} \right) \right]_{q=0} dx \quad [4-10]$$

Since the total stress intensity factor is the sum of  $K_{\sigma\infty}$  and  $K_q$ , the square of  $K_T$  can be expanded.

$$= \int_{-a}^a \left[ \frac{\partial}{\partial q} \left( \frac{K_{\sigma\infty}^2 + 2K_{\sigma\infty}K_q + K_q^2}{E'} \right) \right]_{q=0} dx \quad [4-11]$$

$K_{\sigma\infty}$  and  $K_q$  can be further expanded by substituting with their respective solutions.

$$= \frac{1}{E'} \int_{-a}^a \left[ \frac{\partial}{\partial q} \left( \left( \sigma_{\infty} \sqrt{\pi a} \cdot F_1(a/b) \right)^2 + 2\sigma_{\infty} \sqrt{\pi a} \cdot F_1(a/b) \cdot \frac{q}{\sqrt{\pi a}} \cdot F_2(a/b) + \left( \frac{q}{\sqrt{\pi a}} \cdot F_2(a/b) \right)^2 \right) \right]_{q=0} dx \quad [4-12]$$

The first term is zero order in  $q$  so the derivative with respect to  $q$  is zero.

$$= \frac{1}{E'} \int_{-a}^a \left[ 0 + 2\sigma_{\infty} F_1(a/b) \cdot F_2(a/b) + \frac{2q}{\sqrt{\pi a}} \left( F_2(a/b) \right)^2 \right]_{q=0} dx \quad [4-13]$$

The derivative of the second term is independent of q and the derivative of the third term is linear in q. Evaluating these terms at q=0 simplifies the expression for the center crack displacement to Equation 4-14.

$$\delta_c = \frac{2\sigma_{\infty}}{E'} \int_{-a}^a F_1(a/b) \cdot F_2(a/b) dx \quad [4-14]$$

The crack is symmetric about x=0, so the limits can be changed to go from 0 to a, and a factor of 2 comes out.

$$\delta_c = \frac{4\sigma_{\infty}}{E'} \int_0^a F_1(a/b) \cdot F_2(a/b) dx \quad [4-15]$$

The functions F<sub>1</sub> and F<sub>2</sub> are determined by fifth order polynomial fits of the solutions from Bowie and Tada, respectively. These fits were found to give R<sup>2</sup>>0.995. The polynomials are given as functions of (a/b) below.

$$\begin{aligned} \sqrt{1 - (a/b)} \cdot F_1(a/b) &= P_1(a/b) = \\ &= -3.243 (a/b)^5 + 6.621 (a/b)^4 - 5.674 (a/b)^3 + 2.770 (a/b)^2 - 0.643 (a/b) + 1.0037 \end{aligned} \quad [4-16]$$

$$\begin{aligned} \sqrt{1 - (a/b)} \cdot F_2(a/b) &= \\ = P_2(a/b) &= -5.5227 (a/b)^5 + 17.993 (a/b)^4 - 21.559 (a/b)^3 + 10.336 (a/b)^2 - 0.9545 (a/b) + 1 \end{aligned} \quad [4-17]$$

The polynomials must be multiplied together, and separated into terms of the same order with respect to a/b. The product of the sums of the two polynomials is given as P<sub>T</sub>(a/b).

$$P_T = P_1(a/b) \cdot P_2(a/b) = \alpha_0\beta_0 + (\alpha_0\beta_1 + \alpha_1\beta_0)(a/b) + (\alpha_0\beta_2 + \alpha_1\beta_1 + \alpha_2\beta_0)(a/b)^2 + \dots \quad [4-18]$$

$$\delta_c = \frac{4\sigma_{\infty}}{E'} \int_0^a \frac{1}{(1-a/b)} P_T(a/b) dx \quad [4-19]$$

The limits can be changed such that m=a/b, dm=da/b, da=b·dm. Thus, m=0 at a=0 and m=a/b at a=a. The limits can now be expressed as 0 and a/b.

$$\delta_c = \frac{4\sigma_{\infty}}{E'} \int_0^{a/b} \frac{1}{(1-m)} P_T(m) \cdot b dm \quad [4-20]$$

Since b is a constant it can be moved to the outside of the integrand.

$$\delta_c = \frac{4b\sigma_\infty}{E'} \int_0^{a/b} \frac{1}{(1-m)} P_T(m) dm \quad [4-21]$$

Equation 4-21 can be integrated by parts, and the general formula is given in Equation 4-22.

$$\int u dv = uv - \int v du \quad [4-22]$$

Where  $u = 1/(1-m)$ ,  $du = -\frac{1}{(1-m)^2} dm$ ,  $v = P_T^{+1}(m)$ , and  $dv = P_T(m) dm$ . In this notation,  $P_T^{+1}(m)$  indicates the integral of  $P_T(m)$  with respect to  $m$ .

$$P_T^{+1}(m) = \int P_T(m) dm \quad [4-23]$$

Substituting the parts into Equation 4-24 gives the first iteration of the integration.

$$\int \frac{1}{(1-m)} P_T(m) dm = \frac{P_T^{+1}(m)}{(1-m)} - \int \frac{-P_T^{+1}(m)}{(1-m)^2} dm \quad [4-24]$$

A second iteration gives additional terms, where the superscripts refer to the number of integrations to perform.

$$\int \frac{1}{(1-m)} P_T(m) dm = \frac{P_T^{+1}(m)}{(1-m)} - \left[ \frac{P_T^{+2}(m)}{(1-m)^2} - \int \frac{2P_T^{+3}(m)}{(1-m)^3} dm \right] \quad [4-25]$$

After executing sufficient iterations to achieve the desired accuracy (ten were used in this work), the expression for  $\delta_c$  contains many polynomial terms of the form

$$A_n \cdot P_T^{+n}(m)/(1-m)^n.$$

$$\delta_c = \frac{4b\sigma_\infty}{E'} \left[ \frac{P_T^{+1}(m)}{(1-m)} - \frac{P_T^{+2}(m)}{(1-m)^2} + \frac{2P_T^{+3}(m)}{(1-m)^3} - \frac{6P_T^{+4}(m)}{(1-m)^4} + \frac{24P_T^{+5}(m)}{(1-m)^5} + \dots \right]^{a/b} \quad [4-26]$$

The coefficients of the polynomials  $P_T^{+n}(m)$  are tabulated in Table 4-2 in the form given in Equation 4-27.

$$P_T^{+n}(m) = \sum_{i=0}^{10} C_i \left( \frac{a}{b} \right)^i \quad [4-27]$$

Where  $C_i$  are the coefficients of the terms with different powers of  $(a/b)$ .  $A_i$  are the numerical prefactors that arise from the multiple integration.

Equation 4-26 represents the solution for  $\delta_c$  in terms of  $\sigma_\infty$ . Equation 4-26 can be rearranged to give  $\sigma_\infty$  in terms of the displacements.

$$\sigma_\infty = \frac{E' \delta_c}{4b} \quad [4-28]$$

The far-field stress can then be substituted into Equation 4-6 to give the mode I stress intensity factor  $K_I = \sigma_\infty \sqrt{\pi a} \cdot F_1(a/b)$ .

**Table 4-2. Prefactors and coefficients of the polynomials  $P_T^{+n}(m)$ .**

$A_i$	Integral	$C_0$	$C_1$	$C_2$	$C_3$	$C_4$
1	$P_T^{+1}(a/b)$	1.0067 E+0	-8.1704 E-1	4.6249 E+0	-9.2316 E+0	1.4690 E+1
-1	$P_T^{+2}(a/b)$	5.0335 E-1	-2.7235 E-1	1.1562 E+0	-1.8463 E+0	2.4483 E+0
2	$P_T^{+3}(a/b)$	1.6778 E-1	-6.8086 E-2	2.3124 E-1	-3.0772 E-1	3.4975 E-1
-6	$P_T^{+4}(a/b)$	4.1946 E-2	-1.3617 E-2	3.8541 E-2	-4.3960 E-2	4.3719 E-2
24	$P_T^{+5}(a/b)$	8.3892 E-3	-2.2695 E-3	5.5058 E-3	-5.4950 E-3	4.8577 E-3
-120	$P_T^{+6}(a/b)$	1.3982 E-3	-3.2422 E-4	6.8822 E-4	-6.1056 E-4	4.8577 E-4
720	$P_T^{+7}(a/b)$	1.9974 E-4	-4.0528 E-5	7.6469 E-5	-6.1056 E-5	4.4161 E-5
-5040	$P_T^{+8}(a/b)$	2.4968 E-5	-4.5031 E-6	7.6469 E-6	-5.5505 E-6	3.6801 E-6
40320	$P_T^{+9}(a/b)$	2.7742 E-6	-4.5031 E-7	6.9518 E-7	-4.6254 E-7	2.8308 E-7
-362880	$P_T^{+10}(a/b)$	2.7742 E-7	-4.0937 E-8	5.7931 E-8	-3.5580 E-8	2.0220 E-8

$A_i$	Integral	$C_5$	$C_6$	$C_7$	$C_8$	$C_9$	$C_{10}$
1	$P_T^{+1}(a/b)$	-2.4200 E+1	3.4645 E+1	-3.5355 E+1	2.3283 E+1	-8.9508 E+0	1.5283 E+0
-1	$P_T^{+2}(a/b)$	-3.4572 E+0	4.3306 E+0	-3.9284 E+0	2.3283 E+0	-8.1371 E-1	1.2736 E-1
2	$P_T^{+3}(a/b)$	-4.3215 E-1	4.8118 E-1	-3.9284 E-1	2.1166 E-1	-6.7809 E-2	9.7967 E-3
-6	$P_T^{+4}(a/b)$	-4.8016 E-2	4.8118 E-2	-3.5713 E-2	1.7638 E-2	-5.2161 E-3	6.9976 E-4
24	$P_T^{+5}(a/b)$	-4.8016 E-3	4.3743 E-3	-2.9761 E-3	1.3568 E-3	-3.7258 E-4	4.6651 E-5
-120	$P_T^{+6}(a/b)$	-4.3651 E-4	3.6453 E-4	-2.2893 E-4	9.6915 E-5	-2.4839 E-5	2.9157 E-6
720	$P_T^{+7}(a/b)$	-3.6376 E-5	2.8041 E-5	-1.6352 E-5	6.4610 E-6	-1.5524 E-6	1.7151 E-7
-5040	$P_T^{+8}(a/b)$	-2.7982 E-6	2.0029 E-6	-1.0901 E-6	4.0381 E-7	-9.1318 E-8	9.5284 E-9
40320	$P_T^{+9}(a/b)$	-1.9987 E-7	1.3353 E-7	-6.8133 E-8	2.3754 E-8	-5.0732 E-9	5.0149 E-10
-362880	$P_T^{+10}(a/b)$	-1.3325 E-8	8.3454 E-9	-4.0078 E-9	1.3196 E-9	-2.6701 E-10	2.5075 E-11

## Monitoring Stress and Strength

The analysis detailed above allows the far-field stress acting on biaxially constrained membranes with center cracks to be determined from the displacements.

Figure 4-16 shows how the far-field stress in a cracked membrane increases as a function of weight loss at 55°C.

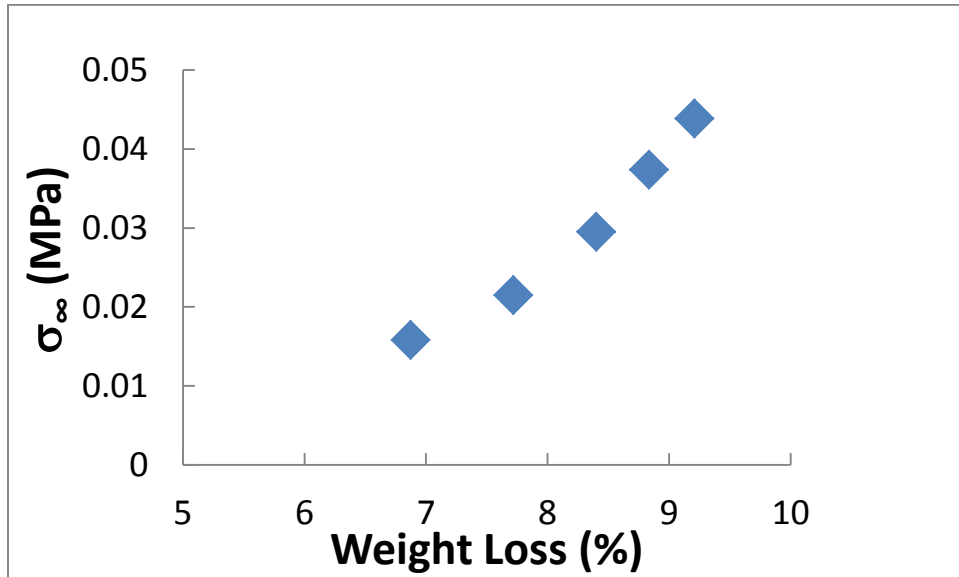


**Figure 4-16 Plot of far-field stress vs weight loss for a center cracked biaxially constrained membrane.**

The stress appears to increase in a non-linear fashion. Since  $T_g$  and the elastic modulus both increase with weight loss, the membranes begin to take on a more glassy nature where a relatively small change in volume due to loss of small molecules can create higher stresses. The fracture toughness of the membranes also increases with weight loss, as shown in Figure 4-17.

In order for  $K_I$  to be equal to  $K_{IC}$ , the crack must be on the verge of actively growing. At the values of weight loss in Figure 4-17 the cracks are actively growing, whereas they are not actively growing below ~5% weight loss based on photographic measurements of the crack tips.

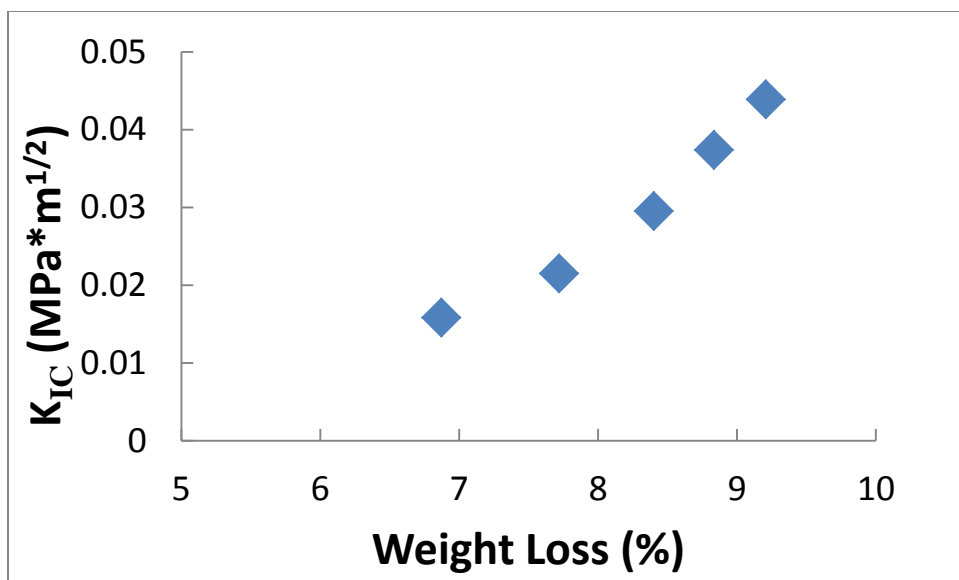


**Figure 4-17 Fracture toughness vs weight loss during conditioning of biaxially constrained membranes at 55°C. The increase in fracture toughness with weight loss indicates that the presence of solvent reduces the stresses that develop and the toughness of the membrane materials.**

Thus, it appears that both the far-field stress and the strength of the coating materials increase with the removal of small molecule solvents and plasticizers. This evolution is important to the long term durability of a coating. However, it does indicate that when the coating is freshly applied it is vulnerable to external stresses and defects that can lead to future failure.

## **Conclusions**

Techniques are developed to monitor the evolution of residual stresses in and the strength of complex multicomponent epoxy-amine based coatings as they undergo conditioning at elevated temperatures. Characterization of the basic physical and mechanical properties of the membrane materials indicated that their properties change significantly during elevated temperature conditioning. The evolution of properties was attributed to the loss of volatile small molecules from the coatings. Acoustic and membrane inflation techniques, applied to uncracked membranes, are able to measure the

stresses developed due to solvent loss in biaxially constrained membranes. By optically measuring the dimensions of cracks introduced in the membranes, and measuring the modulus of the material, we were able to simultaneously monitor the evolution of stresses and toughness of the materials using a fracture mechanics analysis. These techniques are applicable to the characterization of stress and strength in a wide variety of membrane materials where complex curing, ageing, or degradation processes prevent the straightforward measurement and prediction of physical and mechanical properties.

## **References**

1. Ellis B. Chemistry and Technology of Epoxy Resins New York: Chapman and Hall; 1993.
2. Rasband WS. ImageJ [<http://imagej.nih.gov/ij/>]. Bethesda, MD, USA; 1997-2011.
3. Morse PM. Vibration and Sound. 2nd ed. New York: McGraw-Hill; 1948.
4. Morse PM, Ingard KU. Theoretical Acoustics Princeton: Princeton University Press; 1986.
5. Chobotov VA, Binder RC. Journal of the Acoustical Society of America. 1964; 31: p. 59-73.
6. Maden MA, Farris RJ. Stress measurements in spin coated polyimide films using real time averaged holographic interferometry. MRS Proceedings. 1989 April; 154: p. 143.
7. Bowie OL, Neal DM. International Journal of Fracture Mechanics. 1970; 6: p. 199-206.
8. Tada H, Paris PC, Irwin GR. The Stress Analysis of Cracks Handbook: Del Research Corp.; 1973.

## BIBLIOGRAPHY

### Chapter 1

1. Cross A, Haward RN. Orientation hardening of PVC. *Polymer*. 1978; 19: p. 677.
2. Struik LCE. *Physical Ageing of Amorphous Polymers and Other Materials* Amsterdam: Elsevier; 1978.
3. van Melick HGH, Govaert LE, Meijer HEH. On the origin of strain hardening in glassy polymers. *Polymer*. 2003; 44: p. 2493-2502.
4. McKenna GB. Mechanical rejuvenation in polymer glasses: fact or fallacy? *Journal of Physics: Condensed Matter*. 2003; 15(11): p. 737-763.
5. Klompen ETJ, Engels TAP, Govaert LE, Meijer HEH. Modeling of the postyield response of glassy polymers: influence of thermomechanical history. *Macromolecules*. 2005; 38: p. 6997-7008.
6. Ellis B. *Chemistry and Technology of Epoxy Resins* New York: Chapman and Hall; 1993.
7. Lee A, McKenna GB. Effect of crosslink density on physical ageing of epoxy networks. *Polymer*. 1988; 29: p. 1812-1817.
8. Wang X, Gillham JK. Physical aging in the glassy state of a thermosetting system vs. extent of cure. *Journal of Applied Polymer Science*. 1993; 47: p. 447-460.
9. G'Sell C, McKenna GB. Influence of physical ageing on the yield response of model DGEBA/poly(propylene oxide) epoxy glasses. *Polymer*. 1992; 33(10): p. 2103-2113.
10. Detwiler AT, Lesser AJ. Aspects of network formation in glassy thermosets. *Journal of Applied Polymer Science*. 2010; 117: p. 1021-1034.
11. White SR, Mather PT, Smith MJ. Characterization of the cure state of DGEBA-DDS epoxy using ultrasonic, dynamic mechanical, and thermal probes. *Polymer Engineering and Science*. 2002; 42(1): p. 51-67.
12. Rana D, Sauvant V, Halary JL. Molecular analysis of yielding in pure and antiplasticized epoxy-amine thermosets. *Journal of Materials Science*. 2002; 37: p. 5267.

13. Wang X, Gillham JK. Tg-temperature property (TgTP) diagram for thermosetting systems: Anomalous behavior of physical properties vs. extent of cure. *Journal of Applied Polymer Science*. 1993; 47: p. 425-446.
14. Montserrat S. Vitrification and further structural relaxation in the isothermal curing of an epoxy resin. *Journal of Applied Polymer Science*. 1992; 44: p. 545.
15. Cook WD, Scott TF, Quay-Thevenon S, Forsythe JS. Dynamic mechanical thermal analysis of thermally stable and thermally reactive network polymers. *Journal of Applied Polymer Science*. 2004; 93: p. 1349-1359.
16. Tcharkhtchi A, Trotignon JP, Verdu J. Yielding and fracture in crosslinked epoxies. *Macromolecular Symposia*. 1999; 147: p. 221.
17. Madsen PA, Foister RT. Network structure and properties of imidazole-cured epoxy novolac adhesives. *Journal of Applied Polymer Science*. 1989; 37: p. 1931.
18. Calzia KJ, Lesser AJ. Post-Yield Deformation of Glassy Networks: Effects of Molecular Architecture. In ANTEC; 2006; Charlotte, NC.
19. Wang X, Gillham JK. Analysis of crosslinking in amine-cured epoxy systems: The one-to-one relationship between Tg and conversion. *Journal of Applied Polymer Science*. 1992; 45: p. 2127.
20. Jordan C, Galy J, Pascual JP. Measurement of the extent of reaction of an epoxy-cycloaliphatic amine system and influence of the extent of reaction on its dynamic and static mechanical properties. *Journal of Applied Polymer Science*. 1992; 46: p. 859-871.
21. Verchere D, Sautereau H, Pascual JP, Riccardi CC, Moschiar SM, Williams RJJ. Buildup of epoxy-cycloaliphatic amine networks. Kinetics, vitrification, and gelation. *Macromolecules*. 1990; 23: p. 725-731.
22. Charlesworth JM. Effect of cross-link density on the molecular relaxations in diepoxide-diamine network polymers 1. The glassy region. *Polymer Engineering and Science*. 1988; 28(4): p. 221-229.
23. Matejka L. Amine Cured Epoxide Networks: Formation, Structure, and Properties. *Macromolecules*. 2000; 33: p. 3611-3619.
24. Flory PJ. Molecular Size Distribution in Three Dimensional Polymers. I. Gelation. *Journal of the American Chemical Society*. 1941; 63: p. 3083-3090.
25. Flory PJ. *Principles of Polymer Chemistry* Ithaca: Cornell University Press; 1953.

26. Swier S, Van Assche G, Van Mele B. Reaction kinetics modeling and thermal properties of epoxy–amines as measured by modulated-temperature DSC. I. Linear step-growth polymerization of DGEBA + aniline. *Journal of Applied Polymer Science*. 2004; 91: p. 2798-2813.
27. Wang X, Gillham JK. Competitive Primary Amine/ Epoxy and Secondary Amine/Epoxy Reactions: Effect on the Isothermal Time-to-Vitrify. *Journal of Applied Polymer Science*. 1991; 43: p. 2267-2277.
28. Pang KP, Gillham JK. Anomalous behavior of cured epoxy resins: density at room temperature versus time and temperature of cure. *Journal of Applied Polymer Science*. 1989; 37: p. 1969-1991.
29. Ellis B, Found MS, Bell JR. Effects of cure treatment on glass transition temperatures for a BADGE–DDM epoxy resin. *Journal of Applied Polymer Science*. 1996; 59: p. 1493-1505.
30. Brady RF. Volume change in the polymerization of spirocyclic monomers - Causes, Effects, and Applications. *Journal of Macromolecular Science-Reviews in Macromolecular Chemistry and Physics*. 1992; C32: p. 135-181.
31. Shimbo M, Ochi M, Shigeta Y. Shrinkage and internal stress during curing of epoxide resins. *Journal of Applied Polymer Science*. 1981; 26: p. 2265-2277.
32. Varley RJ, Hodgkin JH, Simon GP. Toughening of trifunctional epoxy system. V. Structure-property relationships of neat resin. *Journal of Applied Polymer Science*. 2000; 77: p. 237-248.
33. Ferry JD. *Viscoelastic Properties of Polymers* New York: Wiley; 1980.
34. Venditti RA, Gillham JK, Jean YC, Lou Y. Free volume after cure vs. fractional conversion for a high-Tg epoxy/amine thermosetting system. *Journal of Applied Polymer Science*. 1995; 56: p. 1207-1220.
35. Kovacs AJ, Stratton RA, Ferry JD. Dynamic mechanical properties of polyvinyl acetate in shear in the glass transition temperature range. *Journal of Physical Chemistry*. 1963; 67: p. 152-161.
36. Johari GP. In Richert R, Blumen A, editors. *Disorder Effects on Relaxational Processes*. New York: Springer-Verlag; 1994. p. 627-657.
37. Haward RN, Young RJ. *The Physics of Glassy Polymers* New York: Chapman and Hall; 1997.

38. Halary JL. Structure–Property Relationships in Epoxy-Amine Networks of Well-Controlled Architecture. *High Performance Polymers*. 2000; 12: p. 141-153.
39. Enns JB, Gillham JK. Effect of the extent of cure on the modulus, glass transition, water absorption, and density of an amine-cured epoxy. *Journal of Applied Polymer Science*. 1983; 28: p. 2831-2846.
40. Robertson RE. Theory for the Plasticity of Glassy Polymers. *The Journal of Chemical Physics*. 1966; 44(10): p. 3950-3956.
41. Golden JH, Hammant BL, Hazell EA. The effect of thermal pretreatment on the strength of polycarbonate. *Journal of Applied Polymer Science*. 1967; 11: p. 1571-1579.
42. Vardoulakis I, Labuz JF, Papamichos E, Tronvoll J. Continuum fracture mechanics of uniaxial compression on brittle materials. *International Journal of Solids and Structures*. 1998; 35: p. 4313.
43. Oyanguren PA, Vallo CI, Frontini PM, Williams RJJ. Rejuvenation of epoxy glasses subjected to uniaxial compression. *Polymer*. 1994; 35: p. 5279-5282.
44. Tervoort TA, Govaert LE. Strain hardening behavior in polycarbonate in the glassy state. *Journal of Rheology*. 2000; 44(6): p. 1263-1277.
45. Govaert LE, van Melick HGH, Meijer HEH. Temporary toughening of polystyrene through mechanical. *Polymer*. 2001; 42: p. 1271-1274.
46. van Melick HGH, Govaert LE, Raas B, Nauta WJ, Meijer HEH. Kinetics of ageing and re-embrittlement of mechanically. *Polymer*. 2003; 44: p. 1171-1179.
47. Hoy RS, Robbins MO. Strain hardening of polymer glasses: Effect of entanglement density, temperature, and rate. *Journal of Polymer Science: Part B: Polymer Physics*. 2006; 44: p. 3487-3500.
48. Boyce MC, Arruda EM. Constitutive models of rubber elasticity: A review. *Rubber Chemistry and Technology*. 2000; 73(3): p. 504-523.
49. Treloar LRG. *The Physics of Rubber Elasticity* Oxford: Clarendon Press; 1975.
50. Wang X, Foltz VJ. Crosslinking induced volume expansion in the glass state. *Polymer*. 2006; 47: p. 5090-5096.
51. Boyce MC, Arruda EM. An Experimental and Analytical Investigation of the Large Strain Compressive and Tensile Response of Glassy Polymers. *Polymer Engineering*

- and Science. 1990; 30(20): p. 12888-1298.
52. Haward RN. The application of a simplified model for the stress-strain curves of polymers. *Polymer*. 1987; 28: p. 1485.
  53. Charlesworth JM. Effect of cross-link density on molecular relaxations in diepoxide-diamine network polymers 2. The rubbery plateau region. *Polymer Engineering and Science*. 1988; 28(4): p. 230-236.
  54. Haward RN, Thackray G. The use of a mathematical model to describe isothermal stress-strain curves in glassy thermoplastics. *Proceedings of the Royal Society of London Series A*. 1968; 302: p. 453-472.
  55. Lesser AJ, Crawford E. The role of network architecture on the glass transition temperature of epoxy resins. *Journal of Applied Polymer Science*. 1997; 66: p. 387-395.
  56. Crawford ED, Lesser AJ. The effect of network architecture on the thermal and mechanical behavior of epoxy resins. *Journal of Polymer Science: Part B: Polymer Physics*. 1998; 36: p. 1371-82.
  57. Crawford ED, Lesser AJ. Brittle to ductile: Fracture toughness mapping on controlled epoxy networks. *Polymer Engineering and Science*. 1999; 39: p. 385-392.
  58. Arruda EM, Boyce MC, Jayachandran R. Effects of strain rate, temperature and thermomechanical coupling on the finite strain deformation of glassy polymers. *Mechanics of Materials*. 1995; 19: p. 193-212.
  59. Kontou E. Modeling of postyield behavior of glassy polymers. *Journal of Applied Polymer Science*. 1996; 61: p. 2191-2195.

## Chapter 2

1. Wu DY, Meure S, Solomon D. Self-healing polymeric materials: A review of recent developments. *Progress in Polymer Science*. 2008; 33: p. 470-522.
2. Wool RP. Self-healing materials: a review. *Soft Matter*. 2008; 4: p. 400-418.
3. Volynskii AL, Bakeev NF. Solvent Crazing of Polymers. *Polymer Science Series A*. 2009; 51: p. 1096-1126.
4. Urban MW. Stratification, stimuli-responsiveness, self-healing, and signaling in polymer networks. *Progress in Polymer Science*. 2009; 34: p. 679-687.

5. Murphy EB, Wudl F. The world of smart healable materials. *Progress in Polymer Science*. 2010; 35: p. 223-251.
6. Kim YH, Wool RP. A theory of healing at a polymer polymer interface. *Macromolecules*. 1983; 16: p. 1115-20.
7. Chen X, Dam MA, Ono K, Mal A, Shen H, Nutt SR, et al. A thermally remendable cross-linked polymeric material. *Science*. 2002; 295: p. 1802-1807.
8. Sivakova S, Bohnsack DA, Mackay ME, Suwanmala P, Rowan SJ. Interactions and phase segregation to yield highly thermosensitive supramolecular polymers. *Journal of the American Chemical Society*. 2005; 127: p. 18202-18211.
9. White SR, Sottos NR, Geubelle PH, Moore JS, Kessler MR, Sriram SR, et al. Autonomic healing of polymer composites. *Nature*. 2001; 409: p. 794-797.
10. Williams HR, Trask RS, Knights AC, Williams ER, Bond IP. Biomimetic reliability strategies for self-healing vascular networks in engineering materials. *Journal of the Royal Society of London Interface*. 2008; 5: p. 735-747.
11. Glad MD, Kramer EJ. Microdeformation and network structure in epoxies. *Journal of Materials Science*. 1991; 26: p. 2273-86.
12. Crawford ED, Lesser AJ. Brittle to ductile: Fracture toughness mapping on controlled epoxy networks. *Polymer Engineering and Science*. 1999; 39: p. 385-392.
13. Lemay JD, Kelley FN. Structure and ultimate properties of epoxy resins. *Advances in Polymer Science*. 1986; 78: p. 115-48.
14. Fischer M. Properties and failure of polymers with tailored distances between cross-links. *Advances in Polymer Science*. 1992; 100: p. 313-55.
15. Jordan C, Galy J, Pascualt JP. Measurement of the extent of reaction of an epoxy-cycloaliphatic amine system and influence of the extent of reaction on its dynamic and static mechanical properties. *Journal of Applied Polymer Science*. 1992; 46: p. 859-871.
16. Varley RJ, Hodgkin JH, Simon GP. Toughening of trifunctional epoxy system. V. Structure-property relationships of neat resin. *Journal of Applied Polymer Science*. 2000; 77: p. 237-248.
17. Marks MJ, Snelgrove RV. Effect of Conversion on the Structure-Property Relationships of Amine-Cured Epoxy Thermosets. *ACS Applied Materials & Interfaces*. 2009; 1: p. 921-926.

18. Lake GJ, Thomas AG. Strength of Highly Elastic Materials. Proceedings of the Royal Society of London Series A-Mathematical and Physical Sciences. 1967; 300: p. 108.
19. Crawford ED, Lesser AJ. The effect of network architecture on the thermal and mechanical behavior of epoxy resins. Journal of Polymer Science: Part B: Polymer Physics. 1998; 36: p. 1371-82.
20. Raghavan J, Wool RP. Interfaces in repair, recycling, joining and manufacturing of polymers and polymer composites. Journal of Applied Polymer Science. 1999; 71: p. 775-85.
21. Outwater JO, Gerry DJ. On the fracture energy, rehealing velocity and refracture energy of cast epoxy resin. Journal of Adhesion. 1969; 1: p. 290.
22. Detwiler AT, Lesser AJ. Aspects of network formation in glassy thermosets. Journal of Applied Polymer Science. 2010; 117: p. 1021-1034.
23. Chen X, Wudl F, Mal AK, Shen H, Nutt SR. New thermally remendable highly cross-linked polymeric materials. Macromolecules. 2003; 36: p. 1802-1807.
24. Wool RP, Yuan BL, McGarel OJ. Welding of polymer interfaces. Polymer Engineering and Science. 1989; 29: p. 1340-67.
25. Enns JB, Gillham JK. Effect of the extent of cure on the modulus, glass transition, water absorption, and density of an amine-cured epoxy. Journal of Applied Polymer Science. 1983; 28: p. 2831-2846.
26. Williams JG. Fracture Mechanics of Polymers New York, NY: Halsted Press: John Wiley & Sons Limited; 1984.
27. Miller DR, Macosko CW. Average Property Relations for Nonlinear Polymerization with Unequal Reactivity. Macromolecules. 1978; 11: p. 656-662.
28. Flory PJ. Molecular Size Distribution in Three Dimensional Polymers. I. Gelation. Journal of the American Chemical Society. 1941; 63: p. 3083-3090.
29. Wool RP. Rigidity percolation model of polymer fracture. Journal of Polymer Science: Part B: Polymer Physics. ; 43: p. 168-183.
30. Lide DR, editor. CRC Handbook of Chemistry and Physics. 90th ed. Boca Raton, Florida: CRC Press/ Taylor and Francis; 2010.
31. Verdu J, Tcharkhtchi A. Elastic properties of thermosets in glassy state. Die

- Angewandte Makromolekulare Chemie. 1996; 240: p. 31-38.
32. Kausch HH. Polymer Fracture Berlin Heidelberg: Springer-Verlag; 1978.
  33. Griffith AA. The phenomena of rupture and flow in solids. Philosophical Transactions of the Royal Society of London Series A. 1921; 221: p. 163-198.
  34. Beiner M, Ngai KL. Interrelation between primary and secondary relaxations in polymerizing systems based on epoxy resins. Macromolecules. 2005; 38: p. 7033-7042.
  35. Montserrat S. Physical aging studies in epoxy resins. I. Kinetics of the enthalpy relaxation process in a fully cured epoxy resin. Journal of Polymer Science: Part B: Polymer Physics. 1994; 32: p. 509-522.
  36. Oleinik EF. Epoxy-aromatic amine networks in the glassy state structure and properties. Advances in Polymer Science. 1986; 80(Part IV): p. 49-99.
  37. Brown HR, Deline VR, Green PF. Evidence for cleavage of polymer chains by crack propagation. Nature. 1989; 341: p. 221-222.
  38. Burton BL. The thermooxidative stability of cured epoxy resins. I. Journal of Applied Polymer Science. 1993; 47: p. 1821-1837.
  39. Bellenger V, Verdu J. Oxidative skeleton breaking in epoxy-amine networks. Journal of Applied Polymer Science. 1985; 30: p. 363-374.
  40. Delor-Jestin F, Drouin D, Cheval PY, Lacoste J. Thermal and photochemical ageing of epoxy resin - Influence of curing agents. Polymer Degradation and Stability. 2006; 91: p. 1247-1255.

### Chapter 3

1. Ellis B. Chemistry and Technology of Epoxy Resins New York: Chapman and Hall; 1993.
2. Bucknall CB, Partridge IK. Phase-separation in epoxy resins containing polyethersulfone. Polymer. 1983; 24(5): p. 639-644.
3. Wu WL, Bauer BJ. Network Structure in Epoxies. 6. The Growth Process Investigated By Neutron Scattering. Polymer. 1989; 30: p. 1384-1388.
4. Beck Tan NC, Bauer BJ, Plestil J, Barnes JD, Liu D, Matejka L, et al. Network structure of bimodal epoxies--a small angle X-ray scattering study. Polymer. 1999;

- 40: p. 4603-14.
5. Wu WL, Hu JT, Hunston DL. Structural heterogeneity in epoxies. *Polymer Engineering and Science*. 1990; 30(14): p. 835-840.
  6. Philipson J, inventor; Method and composition for curing epoxy resins. patent 2891927. 1959.
  7. Lahlali N, Naffakh M, Dumon M. Cure kinetics and modeling of an epoxy resin cross-linked in the presence of two different diamine hardeners. *Polymer Engineering and Science*. 2005; 45: p. 1581-89.
  8. Wiggins PL, inventor; Epoxy curing agent composition. USA patent 4,775,736. 1988 October 4.
  9. Tesch H, Heym M, Doerflinger W, Stutz H, Neumann P, Nissen D, et al., inventors; Curable compositions based on epoxy resins. USA patent RE32,628. 1988 March 22.
  10. de Nograro FF, Llano-Ponte R, Mondragon I. Dynamic and mechanical properties of epoxy networks obtained with PPO based amines/MPDA mixed curing agents. *Polymer*. 1996; 37(9): p. 1589-1600.
  11. Nakajima T, Furukawa H, Tanaka Y, Kurokawa T, Osada Y, Gong JP. True chemical structure of double network hydrogels. *Macromolecules*. 2009; 42: p. 2184-2189.
  12. Singh NK, Lesser AJ. Mechanical and Thermo-Mechanical Studies of Double Networks Based on Thermoplastic Elastomers. *Macromolecules*. 2010; 44: p. 1480-1490.
  13. Thiele JL, Cohen RE. Synthesis, characterization, and viscoelastic behavior of single-phase interpenetrating polystyrene networks. *Polymer Engineering and Science*. 1979; 19(4): p. 284-293.
  14. Bellenger V, Dhaoui W, Verdu J. Internal Antiplasticization in Diglycidyl Ether of Bisphenol A Diamino Diphenyl Methane Non-Stoichiometric Epoxy Networks. *Polymer Engineering and Science*. 1990; 30(6): p. 321-325.
  15. Jordan C, Galy J, Pascual JP. Measurement of the extent of reaction of an epoxy-cycloaliphatic amine system and influence of the extent of reaction on its dynamic and static mechanical properties. *Journal of Applied Polymer Science*. 1992; 46: p. 859-871.

16. Detwiler AT, Lesser AJ. Aspects of network formation in glassy thermosets. *Journal of Applied Polymer Science*. 2010; 117: p. 1021-1034.
17. Flory PJ. Molecular Size Distribution in Three Dimensional Polymers. I. Gelation. *Journal of the American Chemical Society*. 1941; 63: p. 3083-3090.
18. Cook WD, Scott TF, Quay-Thevenon S, Forsythe JS. Dynamic mechanical thermal analysis of thermally stable and thermally reactive network polymers. *Journal of Applied Polymer Science*. 2004; 93: p. 1349-1359.
19. Adam G, Gibbs JH. On the temperature dependence of cooperative relaxation properties in glass-forming liquids. *Journal of Chemical Physics*. 1965 July; 43(1): p. 139-146.
20. Boyer RF. The relation of transition temperatures to chemical structure in high polymers. *Rubber Chemistry and Technology*. 1963; 46: p. 1303.
21. Hale A, Macosko CW, Bair HE. Glass transition temperature as a function of conversion in thermosetting polymers. *Macromolecules*. 1991; 24: p. 2610-2621.
22. Zhan HY, Detwiler AT, Lesser AJ. Manuscript in review. 2011.
23. Beck Tan NC, Bauer BJ, Plestil J, Barnes JD, Liu D, Matejka L, et al. Network structure of bimodal epoxies--a small angle X-ray scattering study. *Polymer*. 1999; 40: p. 4603-4614.
24. Lovell R, Windle AH. WAXS investigation of local structure in epoxy networks. *Polymer*. 1990; 31(4): p. 593-601.
25. Wu WI, Bauer BJ. Network structure of epoxies - a neutron scattering study: 2. *Polymer*. 1986; 27: p. 169-180.
26. Arruda EM, Boyce MC. Evolution of plastic anisotropy in amorphous polymers during finite straining. *International Journal of Plasticity*. 1993; 9: p. 697-720.
27. Kovacs AJ, Aklonis JJ, Hutchinson JM, Ramos AR. Isobaric Volume and Enthalpy Recovery of Glasses II. A Transparent Multiparameter Theory. *Journal of Polymer Science: Polymer Physics Edition*. 1979; 1097-1162.
28. Lesser AJ, Calzia KJ. Molecular parameters governing the yield response of epoxy-based glassy networks. *Journal of Polymer Science Part B: Polymer Physics*. 2004; 42: p. 2050-2056.
29. Crawford ED, Lesser AJ. The effect of network architecture on the thermal and mechanical behavior of epoxy resins. *Journal of Polymer Science: Part B: Polymer*

- Physics. 1998; 36: p. 1371-1382.
30. van Melick HGH, Govaert LE, Meijer HEH. On the origin of strain hardening in glassy polymers. *Polymer*. 2003; 44: p. 2493-2502.
  31. Cross A, Haward RN. Orientation hardening of PVC. *Polymer*. 1978; 19: p. 677.
  32. Treloar LRG. *The Physics of Rubber Elasticity* Oxford: Clarendon Press; 1975.
  33. Arruda EM, Boyce MC, Jayachandran R. Effects of strain rate, temperature and thermomechanical coupling on the finite strain deformation of glassy polymers. *Mechanics of Materials*. 1995; 19: p. 193-212.
  34. Haward RN, Thackray G. The use of a mathematical model to describe isothermal stress-strain curves in glassy thermoplastics. *Proceedings of the Royal Society of London Series A*. 1968; 302: p. 453-472.
  35. Tervoort TA, Govaert LE. Strain hardening behavior in polycarbonate in the glassy state. *Journal of Rheology*. 2000; 44(6): p. 1263-1277.
  36. Charlesworth JM. Effect of cross-link density on molecular relaxations in diepoxide-diamine network polymers 2. The rubbery plateau region. *Polymer Engineering and Science*. 1988; 28(4): p. 230-236.
  37. Porter RS, Johnson JF. The entanglement concept in polymer systems. *Chemical Reviews*. 1966; 66(1): p. 1-27.
  38. Hoy RS, Robbins MO. Strain hardening of polymer glasses: Effect of entanglement density, temperature, and rate. *Journal of Polymer Science: Part B: Polymer Physics*. 2006; 44: p. 3487-3500.
  39. Haward RN, Young RJ. *The Physics of Glassy Polymers* New York: Chapman and Hall; 1997.
  40. Wendlandt M, Tervoort TA, Suter UW. Strain-hardening modulus of cross-linked glassy poly(methyl methacrylate). *Journal of Polymer Science: Part B: Polymer Physics*. 2010; 48: p. 1464-1472.
  41. Govaert LE, Engels TAP, Wendlandt M, Tervoort T, Suter UW. Does the strain hardening modulus of glassy polymers scale with the flow stress? *Journal of Polymer Science: Part B: Polymer Physics*. 2008; 46: p. 2475-2481.
  42. Lesser AJ, Crawford E. The role of network architecture on the glass transition temperature of epoxy resins. *Journal of Applied Polymer Science*. 1997; 66: p. 387-

395.

43. Fox TG, Loshaek S. Influence of molecular weight and degree of crosslinking on the specific volume and glass temperature of polymers. *Journal of Polymer Science*. 1955; 15: p. 371-390.
44. Espuche E, Galy J, Gerard JF, Pascual JP, Sautereau H. Influence of crosslink density and chain flexibility on mechanical properties of model epoxy networks. *Macromolecular Symposia*. 1995; 93: p. 107-115.
45. Robertson RE. Theory for the Plasticity of Glassy Polymers. *The Journal of Chemical Physics*. 1966; 44(10): p. 3950-3956.
46. Calzia KJ, Lesser AJ. Correlating yield response with molecular architecture. *Journal of Materials Science*. 2007; 32: p. 5229-5238.
47. Bree HW, Heijboer J, Struik LCE, Tak AGM. The effect of densification on the mechanical properties of amorphous glassy polymers. *Journal of Polymer Science: Polymer Physics Edition*. 1974; 12: p. 1857-1864.
48. Charlesworth JM. Effect of cross-link density on the molecular relaxations in diepoxide-diamine network polymers 1. The glassy region. *Polymer Engineering and Science*. 1988; 28(4): p. 221-229.
49. G'Sell C, McKenna GB. Influence of physical ageing on the yield response of model DGEBA/poly(propylene oxide) epoxy glasses. *Polymer*. 1992; 33(10): p. 2103-2113.
50. Wang X, Gillham JK. Physical aging in the glassy state of a thermosetting system vs. extent of cure. *Journal of Applied Polymer Science*. 1993; 47: p. 447-460.
51. Boyce MC, Arruda EM. Constitutive models of rubber elasticity: A review. *Rubber Chemistry and Technology*. 2000; 73(3): p. 504-523.
52. Rivlin RS, Saunders DW. Large elastic deformations of isotropic materials. VII. Experiments on the deformation of rubber. *Philosophical Transactions of the Royal Society of London Series A*. 1951; 243: p. 251-288.
53. Bicerano J. Prediction of polymer properties. 3rd ed. New York: Marcel Dekker, Inc.; 2002.
54. Bicerano J, Sammler RL, Carriere CJ, Seitz JT. Correlation between glass transition temperature and chain structure for randomly crosslinked high polymers. *Journal of Polymer Science: Part B: Polymer Physics*. 1996; 34: p. 2247-2259.

## Chapter 4

1. Ellis B. Chemistry and Technology of Epoxy Resins New York: Chapman and Hall; 1993.
2. Rasband WS. ImageJ [<http://imagej.nih.gov/ij/>]. Bethesda, MD, USA; 1997-2011.
3. Morse PM. Vibration and Sound. 2nd ed. New York: McGraw-Hill; 1948.
4. Morse PM, Ingard KU. Theoretical Acoustics Princeton: Princeton University Press; 1986.
5. Chobotov VA, Binder RC. Journal of the Acoustical Society of America. 1964; 31: p. 59-73.
6. Maden MA, Farris RJ. Stress measurements in spin coated polyimide films using real time averaged holographic interferometry. MRS Proceedings. 1989 April; 154: p. 143.
7. Bowie OL, Neal DM. International Journal of Fracture Mechanics. 1970; 6: p. 199-206.
8. Tada H, Paris PC, Irwin GR. The Stress Analysis of Cracks Handbook: Del Research Corp.; 1973.